

NGC 6153: Reality is complicated*

MICHAEL G. RICHER,¹ ANABEL ARRIETA,² LORENA ARIAS,² LESLY CASTAÑEDA-CARLOS,³ SILVIA TORRES-PEIMBERT,³
JOSÉ ALBERTO LÓPEZ,¹ AND ADOLFO GALINDO⁴

¹*Instituto de Astronomía, Universidad Nacional Autónoma de México, Apartado Postal 106, CP 22800 Ensenada, Baja California, México; richer@astro.unam.mx, jal@astro.unam.mx*

²*Departamento de Física y Matemáticas, Universidad Iberoamericana, Prolongación Paseo de la Reforma 880, Lomas de Santa Fe, CP 01210, Ciudad de México, México; anabel.arrieta@ibero.mx, lorena.arias@ibero.mx, eadolfogalindo@gmail*

³*Instituto de Astronomía, Universidad Nacional Autónoma de México, Apartado Postal 70-264, CP 04510 Ciudad de México, México; silvia@astro.unam.mx, lcastaneda@astro.unam.mx*

⁴*Departamento de Física y Matemáticas, Universidad Iberoamericana, Prolongación Paseo de la Reforma 880, Lomas de Santa Fe, CP 01210, Ciudad de México, México; anabel.arrieta@ibero.mx, lorena.arias@ibero.mx, eadolfogalindo@gmail.com*

ABSTRACT

We study the kinematics of emission lines that arise from many physical processes in NGC 6153 based upon deep, spatially-resolved, high resolution spectra acquired with the UVES spectrograph at the ESO VLT. Our most basic finding is that the plasma in NGC 6153 is complex, especially its temperature structure. The kinematics of most emission lines defines a classic expansion law, with the outer part expanding fastest (normal nebular plasma). However, the permitted lines of O I, C II, N II, O II, and Ne II present a constant expansion velocity that defines a second kinematic component (additional plasma component). The physical conditions imply two plasma components, with the additional plasma component having lower temperature and higher density. The [O II] density and the [N II] temperature are anomalous, but may be understood considering the contribution of recombination to these forbidden lines. The two plasma components have very different temperatures. The normal nebular plasma appears to have temperature fluctuations in part of its volume (main shell), but only small fluctuations elsewhere. The additional plasma component contains about half of the mass of the N²⁺ and O²⁺ ions, but only 3 – 5% of the mass of H⁺ ions, so the two plasma components have very different chemical abundances. We estimate abundances of $12 + \log(\text{O}^{2+}/\text{H}^+) \sim 9.2$ dex and $\text{He}/\text{H} \sim 0.13$. Although they are all complications, multiple plasma components, temperature fluctuations, and the contributions of multiple physical processes to a given emission line are all part of the reality in NGC 6153, and should generally be taken into account.

Keywords: stars: evolution; ISM: abundances; planetary nebulae: individual (NGC 6153); techniques: spectroscopic

1. INTRODUCTION

NGC 6153 is a bright, southern planetary nebula that has played an important part in the abundance discrepancy problem. The abundance discrepancy was first noted by Wyse (1942), who observed permitted lines of O II and found that they indicated a much higher oxygen abundance than the forbidden [O III] lines that originate

from the same O²⁺ ions. Over the decades, study after study has found that the permitted lines yield systematically larger abundances of C, N, O, and Ne than do the forbidden lines, which is known as the abundance discrepancy problem. The abundance discrepancy occurs in both H II regions and planetary nebulae. Whether it also occurs in active galactic nuclei is unknown since their kinematics impede investigating it.

Until the 1990's, the magnitude of the abundance discrepancy was typically a factor of 2 – 3 (the permitted lines indicated abundances 2 – 3 times higher than the forbidden lines). However, as CCD detectors came into common use, it became clear that many planetary

Corresponding author: Michael G. Richer
richer@astro.unam.mx

* Based on observations collected at the European Southern Observatory under ESO programme(s) 69.D-0174(A).

nebulae had abundance discrepancies that were much higher, e.g., a factor of 5 in NGC 7009 (Liu et al. 1995), 10 in NGC 6153 (Liu et al. 2000), and values in excess of 100 for A46 (Corradi et al. 2015). In their study of NGC 6153, Liu et al. (2000) proposed their model of a chemically-inhomogeneous plasma containing hydrogen-deficient clumps as a possible explanation of the abundance discrepancy. This model and the model of temperature fluctuations that Peimbert (1967) originally suggested to explain the factor of 2 abundance discrepancies in H II regions have remained the main contenders to explain the abundance discrepancy. (Torres-Peimbert et al. (1990) had shown how a chemically-inhomogeneous model of NGC 4361 could explain the discrepant C abundances found from permitted and forbidden lines.)

Much of the debate regarding the abundance discrepancy, at least in planetary nebulae, has focussed upon which of the abundances, derived from permitted or forbidden lines, are the correct abundance ratios to characterize the chemical composition of the plasma in planetary nebulae. This has happened even though evidence for a difference in the spatial distributions of the emission from the permitted and forbidden lines has long existed, with the permitted emission being more centrally-concentrated (e.g., Barker 1982, 1991; Garnett & Dinerstein 2001; Tsamis et al. 2008; García-Rojas et al. 2016). Likewise, chemically-inhomogeneous models demonstrating that the two abundances may not be contradictory, but instead provide information concerning multiple plasmas in planetary nebulae have existed almost since the Liu et al. (2000) study of NGC 6153 (e.g., Péquignot et al. 2002; Ercolano et al. 2003; Tylenda 2003; Tsamis & Péquignot 2005; Yuan et al. 2011). More recently, the kinematics of the permitted and forbidden lines are often found to be distinct, with the permitted lines apparently arising from more highly ionized plasma, i.e., in agreement with the spatial distribution (Sharpee et al. 2004; Barlow et al. 2006; Otsuka et al. 2010; Richer et al. 2013, 2017; Peña et al. 2017). These results as well as the work of Gómez-Llanos & Morisset (2020) strongly influence our view that the structure of the plasma in planetary nebulae is more complex than hitherto considered in the analyses of their chemical abundances.

Given the length of this paper, we provide a general roadmap here, and more detailed versions at the beginning of each section. In §2, we describe the observations, their reduction, the construction of position-velocity (PV) diagrams, and our estimate of the interstellar reddening for NGC 6153. In §3, we present the results related to the structure of the plasma, with various

lines of evidence indicating the presence of two plasma components. In §4, we focus upon the complex temperature structure of the nebular plasma and its consequences concerning the chemical composition of NGC 6153's nebular shell. In §5, we present our conclusions. In summary, we analyze spectroscopy of NGC 6153 at high spectral resolution and conclude that the kinematics and physical conditions of the nebular plasma are consistent with the presence of two plasma components of different composition, density, and temperature. Ignoring this complexity inevitably leads to the conclusion that there is a large abundance discrepancy in NGC 6153.

2. THE OBSERVATIONS, THEIR REDUCTION, PV DIAGRAMS, AND REDDENING

We begin this section presenting the data used and their reduction. We then continue with a description of the construction of the PV diagrams we use to study the kinematics, physical conditions, and chemical abundances in NGC 6153. We conclude this section with our determination of the reddening for NGC 6153, which also allows us to set a common flux scale for all of the wavelength intervals. Throughout, we identify the wavelengths of emission lines rounded to integer values, except when that would allow confusion, in which cases we provide more precise wavelengths. Generally, we adopt the wavelengths from Van Hoof (Atomic Line List version v3.00b4; 2018)¹ and Kramida et al. (National Institute of Standards and Technology 2021)², but Bowen (1960) for forbidden lines and Clegg et al. (1999) for the fine structure components of H I. We use a lot of atomic data, which we cite in Table 1 and refer to as needed.

2.1. The observations and their reduction

The data used here were acquired via programme 69.D-0174A (PI Danziger) on 8 June 2002 using the Ultraviolet and Visual Echelle Spectrograph (UVES; Dekker et al. 2000) on the Very Large Telescope (VLT) Kueyen (UT2) of the European Southern Observatory (ESO). We retrieved the raw data from the ESO data archive. McNabb et al. (2016) previously analyzed this same data.

UVES is a two-arm, cross-dispersed echelle spectrograph with common pre-slit optics, but independent slit and post-slit optics. The blue and red entrance slits are 10'' and 13'' long. The detector for the blue arm was an

¹ <https://www.pa.uky.edu/peter/newpage/>

² <https://physics.nist.gov/asd>

Table 1. Atomic data used

Ion	Atomic data
H I	Storey & Hummer (1995); Ercolano & Storey (2006)
He I	Ercolano & Storey (2006); Porter et al. (2013)
He II	Storey & Hummer (1995); Ercolano & Storey (2006)
N II	Nussbaumer & Storey (1984); Péquignot et al. (1991); Fang et al. (2011, 2013); Tayal (2011)
O II	Zeippen (1982); Nussbaumer & Storey (1984); Wenåker (1990); Péquignot et al. (1991); Wiese et al. (1996); Tayal (2007); Kisielius et al. (2009); Storey et al. (2017)
O III	Dalgarno et al. (1981); Nussbaumer & Storey (1984); Roueff & Dalgarno (1988); Péquignot et al. (1991); Dalgarno & Sternberg (1989); Liu & Danziger (1993); Storey & Zeippen (2000); Tachiev & Fischer (2001); Froese-Fischer & Tachiev (2004); Storey et al. (2014); Kramida et al. (2021)
S II	Rynkun et al. (2019); Tayal & Zatsariny (2010)
Cl III	Rynkun et al. (2019); Butler & Zeippen (1989)
Ar III	Muñoz Burgos et al. (2009)
Ar IV	Rynkun et al. (2019); Ramsbottom & Bell (1997)

EEV 44-82 CCD with 2048×4096 $15 \mu\text{m}$ pixels. The detector for the red arm was a mosaic of an EEV 44-82 CCD and a MIT-LL CCID-20 CCD, both of which had 2048×4096 $15 \mu\text{m}$ pixels. For these observations, all detectors were used in 2×2 binning. Four cross dispersers (CD#1, CD#2, CD#3, and CD#4) were used to cover the wavelength interval 3043–10655 Å (except for three gaps, see below). The effective spectral resolution ($\lambda/\delta\lambda$) in all cases was in the neighborhood of 30,000. UVES’ atmospheric dispersion corrector was not used.

Figure 1 shows the location of the red spectrograph slit superposed upon the object. The observations of both NGC 6153 and the standard stars CD−32° 9927, LTT 3864, and Feige 56 occurred on 8 June 2002, all at low airmass (1.0–1.14 for NGC 6153; 1.01–1.25 for the standards). The observations consist of two standard UVES instrument configurations with simultaneous coverage of CD#1 and CD#3 and then CD#2 and CD#4. For NGC 6153, three 1200 s exposures were obtained for all wavelength intervals. In addition, single short exposures of 60 s (CD#1/CD#3) and 120 s (CD#2/CD#4) were obtained to avoid saturating the brightest lines. While NGC 6153 was east of the meridian, the long exposures and then the short for the CD#2/CD#4 configuration

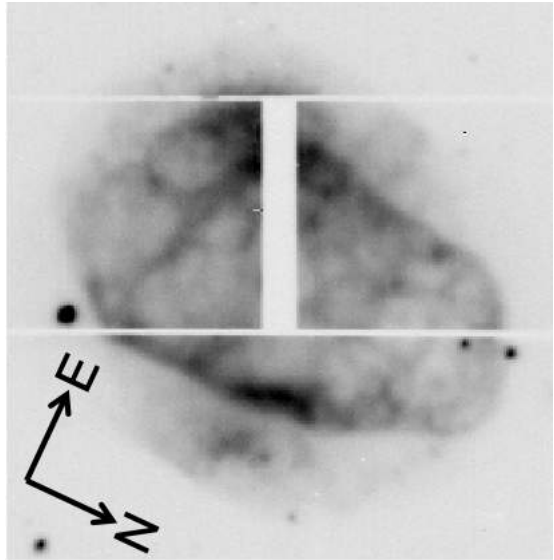


Figure 1. This image from the (red) slit camera shows the slit superposed upon NGC 6153. The arrows indicate the image orientation. The slit size is $15.75'' \times 2''$ and its position angle is 118° (N through E). The decker limits the slit length to $10''$ (CD1 and CD2) or $13''$ (CD3 and CD4).

were acquired, followed by the long exposures and then the short exposure for the CD#1/CD#3 configuration as it crossed the meridian. For the standard stars, all exposures were of 120 s duration. The slit width was $2''$ for NGC 6153 and $10''$ for the standard stars. The observing conditions were not photometric, as the fluxes for NGC 6153 and the standard stars varied from exposure to exposure and between the CD#1/CD#3 and CD#2/CD#4 instrument configurations.

We reduced the data using the Image Reduction and Analysis Facility (IRAF³; Tody 1986, 1993). We reduced the images from each of the three individual CCDs separately, so we work with six wavelength intervals: CD1 (3043–3875 Å), CD2 (3759–4987 Å), CD3b (4980–5965 Å), CD3r (6034–7009 Å), CD4b (7101–8915 Å), and CD4r (9050–10655 Å; “CD3” and “CD4” are shorthand for CD3b+CD3r and CD4b+CD4r, respectively). The reduction steps that follow were applied on a CCD-by-CCD basis. Hence, our data reduction establishes a proper relative flux scale only *within* each of the six wavelength intervals. Given the lack of overlapping spectral coverage between the wavelength intervals (except CD1 and CD2) and the non-photometric observing

³ IRAF is distributed by the National Optical Astronomical Observatory, which is operated by the Association of Universities for Research in Astronomy, Inc., under cooperative agreement with the National Science Foundation.

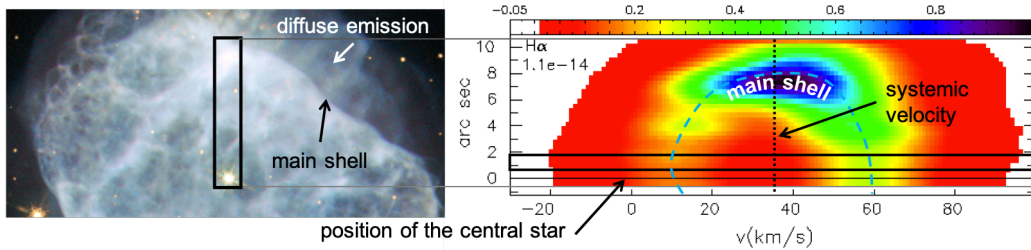


Figure 2. We compare an image (left; Hubble Space Telescope proposal ID 8594) and PV diagram (right; CD#2) of NGC 6153 in the light of $H\alpha$. The spectrograph slit is shown on the left. The position of the central star, whose continuum is subtracted from the PV diagram, would appear at the position of the horizontal line (right panel; y-coordinate of zero). The main structure of NGC 6153 is its main shell, which is the origin of the “ \cap ”-shaped structure in the PV diagram (dashed line): The Doppler effect separates the emission from the approaching and receding sides, except at the top where the expansion is perpendicular to the line of sight. The rectangle (right panel) indicates the three rows used to compute the velocity separation between the approaching and receding sides of the nebula (§3.1). The systemic velocity is the average radial velocity for the object.

conditions, we use the interstellar reddening to establish a common relative flux scale among all of the wavelength intervals (§2.3).

The bias images were combined and subtracted from all other images. The flat field images were processed to remove the scattered light between and within the spectral orders. All of the spectra were divided by their flat field images to remove pixel-to-pixel variations, the spectrograph’s blaze function, and the fringing that occurs in the far-red. The exposure times for the flat field images were very short (0.44 s for CD1, 1.8 s for CD2, 0.33 s for CD3, i.e., CD3b and CD3r, and 0.7 s for CD4), so we created shutter pattern images using other flat field images obtained on the same night and used them to correct the spectra of NGC 6153 and the standard stars. The three long exposures for each wavelength interval for NGC 6153 were combined and then the object spectra were extracted. For the short exposures of NGC 6153 and the standard stars, the object spectra were extracted from the reduced images. When extracting the spectra, the position of the central star of NGC 6153 was traced, as was the standard star’s position. Since NGC 6153 filled the slit, we did not subtract the sky background. Exposures of the ThAr arc lamp were extracted in the same way as the spectra of NGC 6153 and the standard stars and used to determine the wavelength solution. For the wavelength calibration of the CD4 wavelength intervals, we also used the sky lines in the deep spectra of NGC 6153 (wavelengths from Osterbrock et al. 1996, 1997). We combined the order-separated echelle spectra of the standard stars into a single spectrum for each wavelength interval. To derive the system sensitivity function, we used one spectrum of each of the standard stars in the CD1/CD3 wavelength intervals (the ones with the most signal) and one spectrum of LTT 3864 (most signal) and two of CD -32° 9927 (all avail-

able) for the CD2/CD4 wavelength intervals (Hamuy et al. 1992, 1994). We then applied the system sensitivity function to flux-calibrate the spectra of NGC 6153.

2.2. The construction of PV diagrams

We constructed position-velocity (PV) diagrams (or maps) for the emission lines of interest in NGC 6153 from the two-dimensional spectra, of which Figure 2 is an example. PV diagrams present the spatial structure within the slit as a function of radial velocity along the line of sight. At each spatial coordinate in the PV diagram (vertical position in the slit), the emission from the plasma appears at its velocity with respect to the observer due to the Doppler effect. In Figure 2, NGC 6153’s main structure is a shell. There is a more diffuse structure outside it (left panel). Since the shell is expanding, the approaching side is shifted to bluer wavelengths (more negative velocities) while the receding side is shifted to redder wavelengths (more positive velocities). The expansion of the main shell produces the “ \cap ”-shaped structure in the PV diagram. The approaching and receding sides merge to the same velocity at the edge of the shell since the expansion there is perpendicular to the line of sight.

To construct the PV diagrams, we adopt the position of the central star as the spatial zero point and slice the two-dimensional spectra into a collection of one-dimensional spectra one pixel high. These slices correspond to spatial slices of $0.492''$ and $0.362''$ for the blue and red arms, respectively. The number of spatial slices varied for each cross disperser setting, but covered the full extent of the slits in all cases. These spatial slices were then interpolated in a Python script to construct PV diagrams for each line with a uniform spatial sampling of $0.36''$ per row in all of the PV diagrams and spanning a common spatial extent for all wavelengths (i.e., we discard the extra extension of the

red slit). When converting the spectra to PV diagrams, it is necessary to correct the intensities for the change in units from wavelength to velocity, equivalent to multiplying the intensity by a factor of λ/c , where λ is the wavelength of the emission line. The PV diagrams span a velocity range of 130 km/s about the systemic velocity of NGC 6153, which we adopted as 35.0 km/s.

By adopting the position of the central star as the spatial zero point, we eliminate the effect of atmospheric refraction in the spatial direction within the slit. However, we cannot compensate for its effect in the direction perpendicular to the slit. Based upon the tabulated atmospheric refraction for Cerro Paranal⁴, the image displacements perpendicular to slit amount to a maximum of 0.14", 0.07", -0.26", and -0.08" for the cross dispersers CD#1, CD#2, CD#3, and CD#4, respectively. Within each wavelength interval, the maximum image offsets perpendicular to the slit is smaller, 0.10", 0.02", 0.10", and 0.01" for the cross dispersers CD#1, CD#2, CD#3, and CD#4, respectively. (CD#2/CD#4 are affected less since the refraction vector was more parallel to the slit.) To the extent possible, we compare emission lines within a given wavelength interval to minimize the effects of spatial mis-matches due to atmospheric refraction.

We shall often need to compare two PV diagrams. In these comparisons, small errors in wavelength calibration or uncertainties in laboratory wavelengths could introduce spurious structures. To avoid this, we first align the PV diagrams for the individual emission lines to a common velocity scale. The simplest means of doing so is to use the measurements of the velocities for the approaching and receding sides of the nebula, used to determine the velocity splittings in Table 8, setting the mean value for each emission line to a common value. This process should be reasonable since we will usually be comparing PV diagrams for emission lines from ions that arise from the same plasma.

2.3. Interstellar reddening

We use the interstellar reddening to establish a consistent flux scale across our six wavelength intervals. A common flux scale is required in order to study the temperature structure or to investigate the contributions of distinct physical processes to the PV diagrams of a particular transition, e.g., to understand why the forbidden nebular and auroral lines have different velocity splitting. For this reason, we include the reddening as part of the data reductions.

Table 2. The H I and He I lines used for reddening

Interval	H I lines	He I lines
(4)	(5)	(6)
CD1	H9-H25	3187, 3614
CD2	Hβ , H γ , H δ , He ϵ , H9-H11	3965, 4026, 4388, 4438, 4471, 4713, 4922
CD3b		5015, 5876
CD3r	H α	6678
CD4b	P11-P25	7281
CD4r	P7-P9	

We determine both the interstellar reddening and the scale factors for the six wavelength intervals using two one-dimensional spectra (spatially-integrated). The first of these is obtained by summing the one-pixel spatial extractions of the two-dimensional spectra to simulate a traditional one-dimensional spectrum. The second spectrum is a “standard” one-dimensional spectrum from the long exposure spectra of NGC 6153 that was reduced independently. In both cases, we consider only the spatial extent of the blue slit. The results from both spectra are equivalent, so we present those for the first spectrum. We include this spectrum as online data.

We compute the reddening using the H I and He I lines and the [Fitzpatrick \(1999\)](#) reddening law scaled for a total-to-selective extinction ratio of $R_V = 3.07$ ([McCall & Armour 2000](#)). We refer the intensity of the H I lines to H β and that of the He I lines to He I $\lambda 4922$ or He I $\lambda 5876$ using the intrinsic intensity ratios supposing an electron temperature of 10,000 K and the mean of electron densities of 1,000 and 10,000 cm⁻³ (atomic data: Table 1). We do not use the H8 line or He I $\lambda 3889$ because the two are blended. We cannot use the He I $\lambda 5048$ line since it is contaminated by charge overflow from [O III] $\lambda 5007$ in the adjacent order. Only for the CD2 wavelength interval is the wavelength/reddening baseline long enough to establish a secure, independent value for the interstellar reddening. Hence, our relative flux calibration among the six wavelength intervals is relative to the long exposure spectrum for the CD2 wavelength interval. Only the CD1 and CD2 wavelength intervals have emission lines in common that allow checking their relative flux calibration.

Table 2 presents the H I and He I lines available in each wavelength interval for which theoretical line intensities exist. The lines shown in boldface are the

⁴ <https://www.eso.org/gen-fac/pubs/astclim/lasilla/diffrefr.html>

reference lines used to calculate the reddening. Table 3 presents the wavelength interval/order (col. 1; the nomenclature n/x implies wavelength interval CD n and order x), line wavelength (col. 2), the observed (col. 4) and intrinsic (col. 5) relative line intensities for H I lines, the reddening law from Fitzpatrick (1999) (col. 3; $A_1(\lambda) = A(\lambda)/E(B - V)$ for $E(B - V) = 1.0$ mag), and the reddening we find (col. 6). Table 4 presents the analogous information for the He I lines, with He I $\lambda 4922$ used as the reference line in the top half and He I $\lambda 5876$ as the reference line in the bottom half. All of the line intensities in Tables 3 and 4 are from the long exposure spectra, except H α , which is from the short exposure spectrum of interval CD3r (3rs in Table 3). We compute the reddening according to

$$E(B - V) = \frac{\log(F(\lambda)/F(\lambda_{ref})) - \log(I(\lambda)/I(\lambda_{ref}))}{-0.4(A_1(\lambda) - A_1(\lambda_{ref}))}$$

where $F(\lambda)/F(\lambda_{ref})$ are the observed flux ratios, after scaling if they are not from the CD2 wavelength interval, $I(\lambda)/I(\lambda_{ref})$ are the intrinsic flux ratios, and $A_1(\lambda)$ is the reddening law (Fitzpatrick 1999, see above).

Table 3. H I line intensities and reddenings

CD/#	line	$A_1(\lambda)$	$\frac{F(\lambda)}{F(\text{H}\beta)}$	$\frac{I(\lambda)}{I(\text{H}\beta)}$	$E(B - V)$
	(\AA)	(mag)	(obs)	(int)	(mag)
(1)	(2)	(3)	(4)	(5)	(6)
1/127	3669.45	4.67	0.0027	0.0041	0.40
1/127	3671.32	4.67	0.0031	0.0045	0.35
1/127	3673.81	4.67	0.0030	0.0050	0.51
1/127	3676.38	4.66	0.0036	0.0056	0.43
1/127	3679.37	4.66	0.0038	0.0063	0.49
1/127	3682.82	4.66	0.0042	0.0072	0.52
1/126	3682.82	4.66	0.0046	0.0072	0.44
1/127	3686.83	4.65	0.0053	0.0082	0.43
1/126	3686.83	4.65	0.0051	0.0082	0.48
1/127	3691.55	4.65	0.0064	0.0095	0.40
1/126	3691.55	4.65	0.0058	0.0095	0.49
1/127	3697.16	4.64	0.0071	0.011	0.45
1/126	3697.16	4.64	0.0066	0.011	0.53
1/126	3703.86	4.64	0.0078	0.013	0.54
1/126	3711.98	4.63	0.0094	0.016	0.53
1/125	3711.98	4.63	0.0091	0.016	0.56
1/126	3721.95	4.62	0.018	0.020	0.07
1/125	3721.95	4.62	0.017	0.020	0.17

Table 3 *continued*

Table 3 (*continued*)

CD/#	line	$A_1(\lambda)$	$\frac{F(\lambda)}{F(\text{H}\beta)}$	$\frac{I(\lambda)}{I(\text{H}\beta)}$	$E(B - V)$
	(\AA)	(mag)	(obs)	(int)	(mag)
(1)	(2)	(3)	(4)	(5)	(6)
1/125	3734.37	4.61	0.014	0.024	0.57
1/125	3750.15	4.59	0.020	0.031	0.46
1/124	3750.15	4.59	0.020	0.031	0.46
1/124	3770.63	4.57	0.024	0.040	0.57
1/123	3770.63	4.57	0.023	0.040	0.59
1/123	3797.91	4.54	0.032	0.053	0.56
1/122	3797.91	4.54	0.033	0.053	0.51
1/122	3835.40	4.51	0.045	0.073	0.56
1/121	3835.40	4.51	0.044	0.073	0.58
2/124	3770.63	4.57	0.025	0.040	0.50
2/123	3770.63	4.57	0.023	0.040	0.60
2/123	3797.91	4.54	0.033	0.053	0.52
2/122	3797.91	4.54	0.031	0.053	0.60
2/122	3835.40	4.51	0.048	0.073	0.49
2/121	3835.40	4.51	0.045	0.073	0.56
2/118	3970.08	4.38	0.11	0.16	0.48
2/117	3970.08	4.38	0.11	0.16	0.52
2/114	4101.73	4.26	0.18	0.26	0.59
2/114	4101.73	4.26	0.18	0.26	0.59
2/108	4340.47	4.05	0.38	0.47	0.45
2/107	4340.47	4.05	0.37	0.47	0.51
2/96	4861.35	3.56	1	1	
3rs/93	6563.00	2.30	5.00	2.86	0.49
4b/74	8323.42	1.57	0.0039	0.0013	0.60
4b/74	8333.78	1.57	0.0045	0.0015	0.61
4b/74	8345.54	1.56	0.0046	0.0016	0.56
4b/74	8359.00	1.56	0.0059	0.0019	0.63
4b/74	8374.48	1.55	0.0059	0.0021	0.56
4b/74	8392.40	1.55	0.0066	0.0024	0.55
4b/74	8413.32	1.54	0.0066	0.0028	0.47
4b/73	8413.32	1.54	0.0067	0.0028	0.48
4b/73	8437.95	1.53	0.0091	0.0032	0.56
4b/73	8467.26	1.52	0.011	0.0038	0.55
4b/73	8502.48	1.51	0.012	0.0045	0.51
4b/72	8545.38	1.50	0.016	0.0055	0.56
4b/72	8598.39	1.48	0.019	0.0067	0.54
4b/71	8665.02	1.47	0.025	0.0084	0.57
4b/71	8750.46	1.44	0.030	0.011	0.53
4b/70	8862.89	1.41	0.040	0.014	0.54

Table 3 *continued*

Table 3 (*continued*)

CD/#	line	$A_1(\lambda)$	$\frac{F(\lambda)}{F(\text{H}\beta)}$	$\frac{I(\lambda)}{I(\text{H}\beta)}$	$E(B - V)$
	(Å)	(mag)	(obs)	(int)	(mag)
(1)	(2)	(3)	(4)	(5)	(6)
4r/235	9229.01	1.32	0.079	0.025	0.55
4r/233	9545.97	1.24	0.100	0.037	0.47
4r/230	10049.37	1.13	0.21	0.055	0.59

We cross-check the CD2-referenced reddenings in several ways. We compute the reddening using the H I P_n/B_n ratios, where P_n and B_n are the Paschen and Balmer lines, respectively, with upper level n . This uses CD1/CD4b and CD2/CD4r line ratios, but not including H β . There are no H I lines in the CD3b interval. However, we tie its calibration more tightly to other intervals by computing the reddening from the He I lines using He I $\lambda 5876$ as the reference line.

When a line is well-detected in adjacent orders, we use both measurements. Note that the relative line intensities in Tables 3 and 4 already include the scale factors required to place all six wavelength intervals on a common flux scale. These flux scale factors are given in column 2 of Table 5 with the acceptable range for the scale factor in parentheses. These flux scale factors apply to the PV diagrams. The scale factors between the long and short exposures (column 4) are determined by comparing line fluxes measured in both spectra and so are independent of the flux scale factors. The scale factors for the short exposure spectra (column 3) are the ratio of the two previous scale factors. Usually, the uncertainty is dominated by the range allowed for the scale factors of the long exposure spectra.

Figure 3 presents the results, showing the reddening, $E(B - V)$, as a function of wavelength for the H I and He I lines. For the H I lines, the filled circles show the line ratio with respect to H β with the reddening plotted at the wavelength of the H I lines (numerator). The open gray triangles show the reddening computed using the ratios of Paschen and Balmer lines arising from the same upper level, plotted at the wavelength of the Paschen lines (the plot is less confusing that way). The horizontal dashed line is the mean value of $E(B - V)$ for the CD2 wavelength interval. For the He I lines, the open squares show the reddening computed using He I $\lambda 4922$ as the reference line and plotted at the position of each He I line (numerator). The black crosses present the reddening computed from the He I lines using He I

Table 4. He I line intensities and reddenings

CD/#	line	$A_1(\lambda)$	$\frac{F(\lambda)}{F(\text{ref})}$	$\frac{I(\lambda)}{I(\text{ref})}$	$E(B - V)$
	(Å)	(mag)	(obs)	(int)	(mag)
(1)	(2)	(3)	(4)	(5)	(6)
1/147	3187.75	5.24	0.77	3.44	0.93
1/146	3187.75	5.24	0.80	3.44	0.91
1/129	3613.64	4.73	0.11	0.42	1.16
2/118	3964.73	4.39	0.39	0.86	0.96
2/117	3964.73	4.39	0.37	0.86	1.02
2/116	4026.19	4.33	1.22	1.73	0.45
2/107	4387.93	4.01	0.40	0.46	0.30
2/106	4387.93	4.01	0.36	0.46	0.53
2/105	4437.55	3.96	0.05	0.06	0.48
2/105	4471.48	3.93	2.94	3.67	0.55
2/104	4471.48	3.93	2.85	3.67	0.63
2/99	4713.15	3.70	0.37	0.44	0.86
2/99	4713.15	3.70	0.37	0.44	0.86
2/95	4921.93	3.50	1	1	
3b/122	5015.68	3.40	1.53	2.19	-4.17
3b/104	5875.62	2.71	15.80	10.71	0.54
3r/92	6678.15	2.24	5.98	3.02	0.59
3r/91	6678.15	2.24	5.94	3.02	0.59
4b/85	7281.35	1.96	0.83	0.64	0.18
4b/85	7281.35	1.96	0.83	0.64	0.18
1/147	3187.75	5.24	0.048	0.32	0.81
1/146	3187.75	5.24	0.050	0.32	0.79
1/129	3613.64	4.73	0.0071	0.039	0.92
2/118	3964.73	4.39	0.025	0.080	0.76
2/117	3964.73	4.39	0.024	0.080	0.79
2/116	4026.19	4.33	0.077	0.16	0.49
2/107	4387.93	4.01	0.025	0.043	0.44
2/106	4387.93	4.01	0.023	0.043	0.54
2/105	4437.55	3.96	0.0033	0.0060	0.52
2/105	4471.48	3.93	0.19	0.34	0.54
2/104	4471.48	3.93	0.18	0.34	0.57
2/99	4713.15	3.70	0.024	0.041	0.60
2/99	4713.15	3.70	0.024	0.041	0.60
2/95	4921.93	3.50	0.063	0.093	0.54
3b/122	5015.68	3.40	0.097	0.20	1.16
3b/104	5875.62	2.71	15.80	1	
3r/92	6678.15	2.24	0.38	0.28	0.69
3r/91	6678.15	2.24	0.38	0.28	0.67
4b/85	7281.35	1.96	0.053	0.060	-0.18
4b/85	7281.35	1.96	0.053	0.060	-0.18

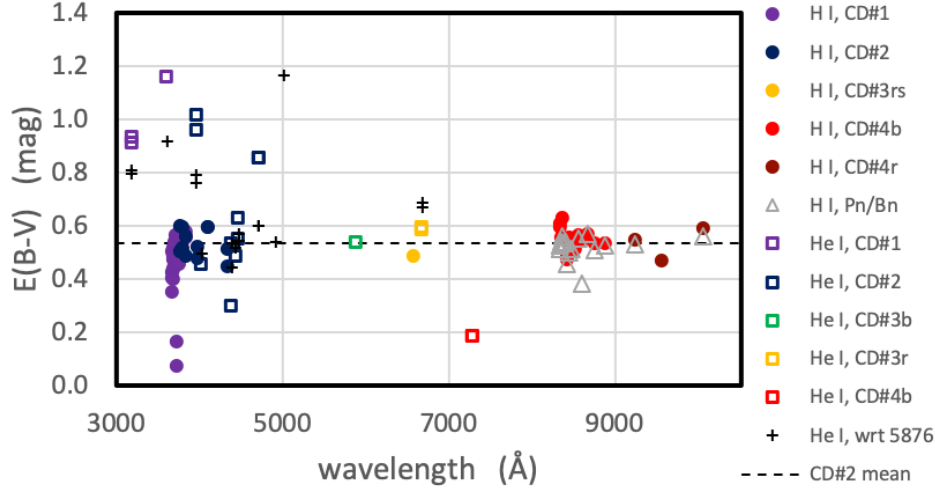


Figure 3. We plot the reddening, $E(B - V)$, from Tables 3 and 4 as a function of wavelength for H I and He I lines. For the lines indicated as “H I, CD# X ”, the line ratio is $H_n/H\beta$ or $P_n/H\beta$ and plotted at the wavelength of H_n or P_n , respectively, the Balmer and Paschen lines originating at upper level n . For the reddening computed from the ratio of Paschen to Balmer lines, P_n/B_n , the reddening is plotted at the wavelength of the Paschen line. The horizontal dashed line represents the mean value of $E(B - V)$ for the H I lines in the CD2 wavelength interval (reference value). For the He I lines, the squares represent ratios using He I $\lambda 4922$ as the reference line while the crosses use He I $\lambda 5876$ as the reference line. The reddening computed from the He I $\lambda\lambda 5015/4922$ and He I $\lambda\lambda 7281/5876$ line ratios fall at negative values (and are not shown). Both lines are apparently much too weak.

Table 5. Flux scale factors

Interval	Long exposure	Short exposure	short/long
(1)	(2)	(3)	(4)
CD1	0.95 (0.915-0.974)	0.778 ± 0.028	1.221 ± 0.023
CD2	1.0 (reference)	0.991 ± 0.047	1.009 ± 0.047
CD3b	2.0 (1.9-2.1)	1.525 ± 0.091	1.312 ± 0.042
CD3r	0.6 (0.57-0.63)	0.430 ± 0.047	1.40 ± 0.13
CD4b	0.5 (0.48-0.51)	0.515 ± 0.019	0.971 ± 0.021
CD4r	0.4 (0.38-0.42)	0.402 ± 0.020	0.995 ± 0.005

$\lambda 5876$ as the reference wavelength, again plotted at the wavelength of the He I line in the numerator. For the H I and He I lines plotted as filled circles and open squares, the colour indicates the wavelength interval.

For the H I lines, the most anomalous is H I $\lambda 3722$, which is blended with [S III] $\lambda 3722$. For the CD1 interval, the reddening decreases for the bluest lines. In contrast, the bluest Paschen lines imply slightly higher extinction. This trend is not apparent when the reddening is computed using the ratio of Paschen and Balmer lines. This could well be the same effect noted by Mesa-Delgado et al. (2009) due to l -changing collisions causing departures from Case B theory since its effect will largely disappear when comparing Paschen and Balmer lines from the same upper level. The He I lines show

considerable scatter. The scatter is more pronounced when using He I $\lambda 4922$ as the reference wavelength, in part because the wavelength baseline for the blue lines is shorter and also because it is the weaker reference line. He I $\lambda\lambda 3187, 3614, 3964, 5015$ are all apparently too weak, regardless of the reference line. Since they all have the metastable 2s levels as their lower levels (He I $\lambda 3187$ is a triplet state, the others singlet states), this may be due to radiative transfer effects. He I $\lambda 7281$ is too weak, independent of the reference line we choose, but it is not clear why. He I $\lambda 6678$ has the same lower level and its intensity is, if anything, slightly too high. Most of the Paschen lines from the CD4b wavelength interval are not anomalous.

Table 6 presents the mean reddening values for lines in each wavelength interval by the different means described above. The mean reddening for the H I lines from the CD2 interval is compatible with that measured for all other wavelength intervals, and we adopt its value, $E(B - V) = 0.535 \pm 0.053$ mag, as our reddening for NGC 6153. Based upon the Fitzpatrick (1999) reddening law, this is equivalent to $c(H\beta) = 1.424E(B - V) = 0.76$ dex.

The reddening we find is lower than that reported by others. Kingsburgh & Barlow (1994) find $c(H\beta) = 0.96$ dex from their optical spectrum, Liu et al. (2000) report $c(H\beta) = 1.27 \pm 0.06$ and 1.30 ± 0.01 dex based upon their scanned (entire object) and minor axis optical spectra, respectively, Pottasch et al. (2003) deduce

Table 6. Average $E(B - V)$

Interval	H I lines	He I lines
CD1	0.496 ± 0.064 ^a	
CD1, overlap	0.560 ± 0.026	
CD2	0.535 ± 0.053	0.528 ± 0.078 ^b
CD3b		0.536 ^b
CD3r	0.486	0.589 ± 0.005 ^c
CD4b	0.561 ± 0.032	
CD4b, Pn/Hn	0.532 ± 0.021	
CD4r	0.536 ± 0.061	
CD4r, Pn/Hn	0.545 ± 0.023	

^aExcludes H I $\lambda 3722$ ^b $\lambda_{ref} = \text{He I } \lambda 5876$ ^c $\lambda_{ref} = \text{He I } \lambda 4922$

$c(\text{H}\beta) = 1.19$ dex comparing the observed $\text{H}\beta$ flux with various 6 cm radio fluxes, and McNabb et al. (2016) obtain $c(\text{H}\beta) = 1.32$ dex based upon the H I Balmer lines. It is not obvious why our reddening is different since we checked that our flux calibrations are similar to the historical calibrations in the ESO archives⁵. Also, the Fitzpatrick (1999) extinction law is similar to the Cardelli et al. (1989) extinction law used by McNabb et al. (2016).

Whether our reddening is correct is less important than whether our intrinsic, reddening-corrected line intensity ratios are correct. For wavelength intervals where the density of H I or He I lines is high (CD2, the red end of CD4b, the blue half of the CD4r), our line ratios corrected for our reddening must necessarily give the correct intrinsic ratios, because that is how we determine the reddening. For the same reason, the flux scale in the vicinity of the He I $\lambda\lambda 5876, 6678$ and $\text{H}\alpha$ lines will also be correct. To check that there are no problems across the CD3b or CD3r wavelength intervals where there are few H I or He I lines, Table 7 presents the He^+/H^+ and $\text{He}^{2+}/\text{H}^+$ abundances for lines that fall in those wavelength intervals and for He II $\lambda\lambda 3203, 4686$ from the CD1 and CD2 intervals. The format of Table 7 is identical to that of Tables 3 and 4, except that the last column presents the He ionic abundance ratios and the intensity ratios are given on the scale

Table 7. He II line intensities and abundances

CD/#	line	$A_1(\lambda)$	$\frac{F(\lambda)}{F(\text{ref})}$	$\frac{I(\lambda)}{I(\text{ref})}$	$\frac{\text{He}^{+i}}{\text{H}^+}$
(1)	(2)	(3)	(4)	(5)	(6)
He I					
2/104	4471.50	3.93	5.00	6.05	0.115
3b/104	5875.60	2.71	26.9	17.5	0.115
3r/92	6678.15	2.24	9.74	5.03	0.117
3r/91	6678.15	2.24	9.66	4.99	0.116
He II					
1/146	3203.17	5.22	4.49	10.4	0.021
1/145	3203.17	5.22	4.01	9.26	0.019
2/100	4685.68	3.73	15.1	16.5	0.014
3b/113	5411.52	3.04	1.43	1.10	0.012
3r/101	6074.11	2.58	0.052	0.032	0.015
3r/100	6074.11	2.58	0.048	0.030	0.014
3r/100	6118.26	2.55	0.056	0.034	0.014
3r/99	6170.60	2.52	0.077	0.046	0.016
3r/96	6406.38	2.39	0.14	0.079	0.016
3r/92	6683.20	2.24	0.19	0.099	0.013
3r/91	6683.20	2.24	0.19	0.099	0.013
3r/89	6890.90	2.14	0.26	0.127	0.013
3r/88	6890.90	2.14	0.29	0.135	0.013

where $F(\text{H}\beta) = I(\text{H}\beta) = 100$. We assume a density of 10^4 cm^{-3} and temperatures of 8,000 K and 10,000 K when computing the He^+ and He^{2+} abundances, respectively (atomic data: Table 1). After correcting for reddening (col. 5), our He I line intensities are very similar to those found by Liu et al. (2000), as expected given that they are used to derive the reddening and flux scale factors. Given the constancy of the $\text{He}^{2+}/\text{H}^+$ abundance ratio for the lines in the CD3b and CD3r wavelength intervals, there is no problem with flux scale. Our only test of the flux scale across the blue half of the CD4b wavelength interval is the [Ar III] $\lambda\lambda 7135, 7751$ lines. Since they indicate very similar [Ar III] temperatures (Figure 15), it would appear that the shape of the flux scale in this part of the CD4b wavelength interval is secure, but we have no objective measure of whether its normalization is correct. (The He II $\lambda\lambda 7177, 7592$ lines are badly affected by an instrumental artifact and atmospheric absorption, respectively.)

So, while we are unable to explain why the reddening we determine for NGC 6153 is different from others, we are confident that our relative line intensities, once corrected for our reddening, yield the correct intrinsic

⁵ <https://www.eso.org/observing/dfo/quality/UVES/qc/SysEffic.qc1.html>

relative intensities. Note that the flux calibration does not affect any result based upon kinematics.

3. RESULTS: THE PLASMA STRUCTURE

The multi-component structure of the plasma in NGC 6153’s nebular shell is the unifying theme of this section. We first analyze the ionization structure of NGC 6153 in detail. We consider both the information available in the morphology of the PV diagrams as well as the more common Wilson diagram, which presents the velocity splitting as a function of the ionization energy. Following this, we investigate the physical conditions based upon kinematics, forbidden lines, and permitted lines. Finally, we show that, by assuming two plasma components in NGC 6153, we can explain the anomalous [N II] temperature and [O II] density as the result of excitation of the [N II] $\lambda 5755$ and [O II] lines due to recombination, mostly in the additional plasma component.

Both the kinematics and the physical conditions imply the presence of two distinct plasma components. One component has the kinematics and physical conditions typically-associated with planetary nebulae (e.g., as described in textbooks Aller 1984; Osterbrock & Ferland 2006), so we shall refer to it as the “**normal nebular plasma**”. The other component has unusual kinematics and is colder and denser than the former, so we shall call it the “**additional plasma component**”.

3.1. The ionization structure of NGC 6153

A PV diagram (e.g., Figure 2) is the result of the spatial distribution, the kinematics, and the physical conditions of the plasma that emits a given line within the nebular volume intercepted by the spectrograph’s slit convolved with the fine structure of that line and the mass of the emitting ion. Figure 4 presents a gallery of PV diagrams that span the full range of ionization energies we could usefully study in NGC 6153, from C IV $\lambda\lambda 5801,5811$ (64.5 eV) to [O I] $\lambda 6300$ (0 eV). In Figure 4, we indicate features that we shall refer to later, such as the emission from the nebula’s main shell, the filament, and the diffuse emission, both of which are beyond the receding side of the main shell. The line that schematically indicates the velocity ellipse for the main shell is drawn for the [O III] $\lambda 4959$ line and repeated in each panel, making it easier to appreciate the systematic changes in the extent of the main shell (away from the central star) or its velocity splitting as a function of ionization energy. In Appendix A (Figures 44-51), we present a large collection of PV diagrams of all stages of ionization.

There are clear and systematic changes in the shape of the line emission profiles as a function of ionization

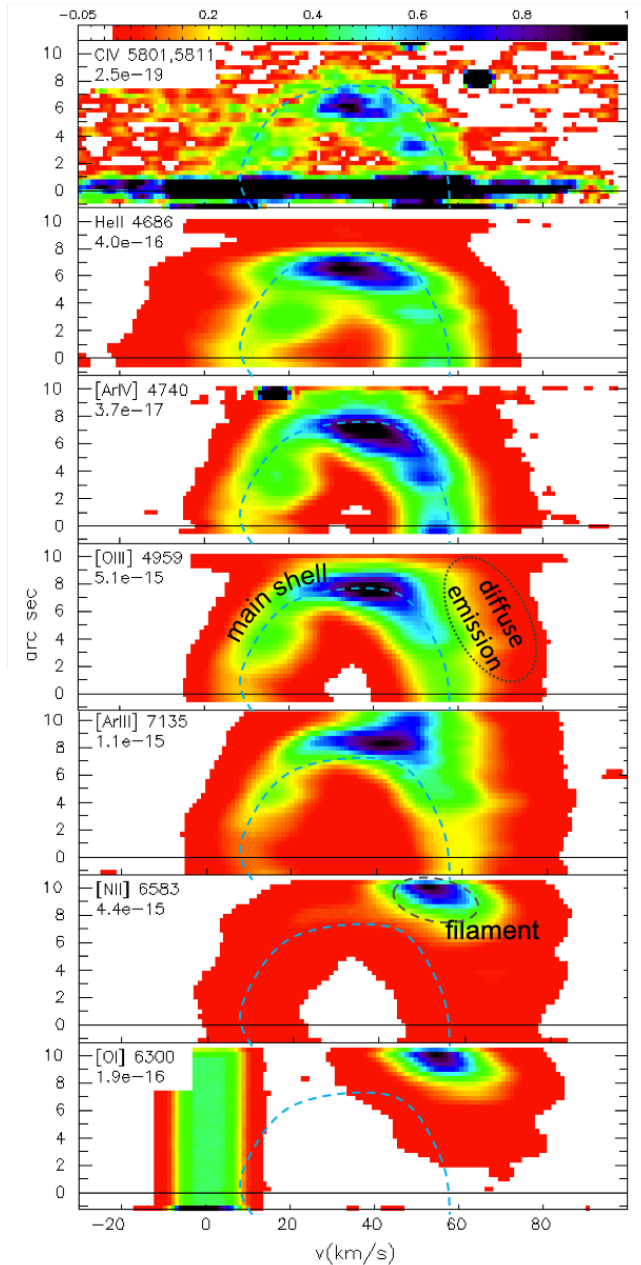


Figure 4. We present the PV diagrams for lines spanning the full range of ionization energies in NGC 6153: C IV $\lambda\lambda 5801,5811$, He II $\lambda 4686$, [Ar IV] $\lambda 4740$, [O III] $\lambda 4959$, [Ar III] $\lambda 7135$, [N II] $\lambda 6583$, and [O I] $\lambda 6300$ (top to bottom). The intensity in each panel is normalized to its maximum value, indicated at upper left in each panel, below the line identification. The color bar at top is common to all panels (-5% to 100% of the maximum value; linear scale). We identify several morphological features that we refer to in the text. There are clear, continuous, and systematic changes in the shape of the emission line profile as a function of the ionization energy. Likewise, the difference in velocity between the approaching and receding sides varies with ionization energy.

energy in Figure 4. In the most highly ionized gas (C IV $\lambda\lambda 5801, 5811$), there is little structure apart from a round velocity ellipse (the low S/N is an impediment; the central star also emits in this line; Liu et al. (2000)). In the next most highly ionized line, He II $\lambda 4686$, much more structure is apparent, and the main shell’s spatial extent increases, creating a profile that is more square in shape. Then, in [Ar IV] $\lambda 4740$, the emission from the main shell changes, especially on the approaching side, to a more rounded shape, mostly as a result of a greater velocity difference between the approaching and receding sides of the main shell, but with little increase in spatial extent. With [O III] $\lambda 4959$, the increasing velocity difference between the two sides of the main shell continues, but there is also less emission on the receding side of the main shell along the direction to the central star (the horizontal line; ordinate value of zero). Continuing to lower ionization energies, in [Ar III] $\lambda 7135$, an extension beyond the main shell on its receding side begins to appear and there is a dimming of both sides of the main shell along the line of sight to the central star. Proceeding to [N II] $\lambda 6583$, the emission from the main shell decreases substantially and the filament is by far the brightest feature. Finally, in the lowest ionization stage, [O I] $\lambda 6300$, the main shell almost disappears while the filament remains very bright (the other emission is telluric).

Figure 5 presents three Wilson (1950) diagrams for NGC 6153 in which we quantify the foregoing, adding details from top to bottom. For emission lines arising from different ions and different excitation processes, we compute the line splitting, measured as the velocity difference between the approaching and receding sides of the nebula. In Figure 5, we plot the line splitting as a function of the ionization potential of the “parent” ion, i.e., the ion that initiates the emission process. For example, O^{2+} ions are responsible for initiating the emission of the permitted lines of O II, and the emission of forbidden [O III] lines. The Bowen fluorescence lines of O III and N III are a special case. These lines arise due to fluorescence from He II Ly α , so we plot them at the ionization energy of He $^+$ and not the ionization energies of O^{2+} and N^{2+} .

We measure the line splitting near the position of central star, within the three rows of the PV diagram in the rectangle in Figure 2, over the spatial extent $0.72''$ – $1.80''$ NE of the central star. Due to the symmetry with respect to the line of sight towards the central star, measuring the line splitting in this region minimizes projection effects. All of the measurements of the line splittings used to construct Figure 5 are given in Table 8. When several lines from a given ion and process

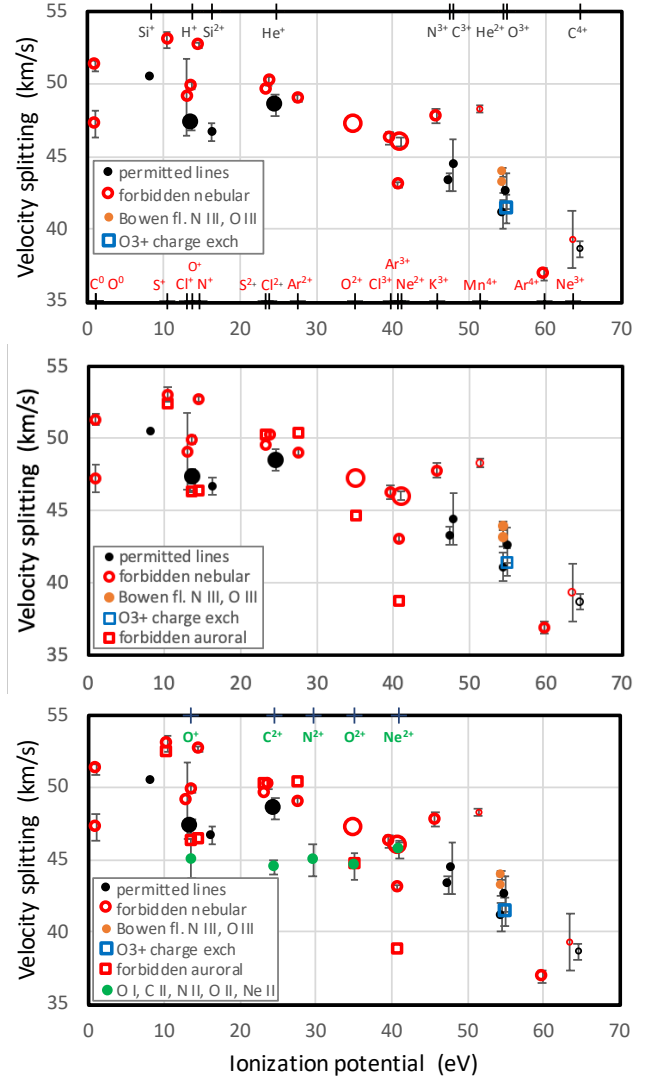


Figure 5. These panels present the Wilson diagram, adding details from top to bottom. The top panel presents the velocity splitting as a function of ionization energy from all forbidden nebular lines and all permitted lines, except those of O^0 , C^+ , N^+ , O^+ , and Ne^+ . These lines establish a well-defined relation between velocity splitting and ionization potential. In the second panel, we add the auroral forbidden lines of N^+ , O^+ , O^{2+} , S^+ , S^{2+} , Ar^{2+} , and Ar^{3+} (open squares). For N^+ , O^+ , O^{2+} , and Ar^{3+} , these transitions have smaller velocity splitting than the nebular transitions. In the bottom panel, we add the permitted lines of O^0 , C^+ , N^+ , O^+ , and Ne^+ . Although these lines span a wide range of ionization potentials, they share a common velocity splitting. The permitted lines of H^0 and He^0 and the forbidden lines of O^{2+} and Ne^{2+} are shown in larger symbols since these lines sample the majority of the nebular volume. The small symbols for Mn^{4+} , Ne^{3+} (forbidden), and C^{3+} (permitted) indicate that they are difficult measurements. The tick marks and labels indicate the ionization energies.

are available, we plot the average line splitting and its standard deviation (error bars) in Figure 5. We adopt ionization energies from [Kramida et al. \(2021\)](#).

In the top panel of Figure 5, the velocity splitting of the emission lines in NGC 6153 decreases as the ionization energy for the parent ion increases ([Wilson 1950](#)). This well-known result arises since the most highly ionized ions are in the innermost plasma that expands most slowly, i.e., the inner plasma cannot overrun the plasma outside it. This panel includes all lines due to forbidden nebular transitions (transitions between the first excited state and the ground state or ground term), Bowen fluorescence lines of O III and N III, charge exchange lines of O III, and all permitted lines, except those of O I, C II, N II, O II, and Ne II. The sequence, from [Ar V], [Ne IV], O III, and He II at the smallest velocity splitting to [S II], [O II], and [N II] at the largest, is therefore expected. With the exception of the H I lines, the permitted and forbidden lines follow a single, continuous ionization structure. Even lines such as O III $\lambda\lambda 3757, 5592$ that arise from charge exchange and the O III and N III Bowen fluorescence emission fall, as they should, at velocities similar to those for the emission from He II and O III recombination (higher ionization energies).

In the second panel, we add the auroral forbidden lines (transitions from the second excited state to the first excited state). For the lines of [O II], [N II], [O III], and [Ar IV] (Table 8), the auroral lines have smaller velocity splitting than their nebular counterparts, e.g., [O II] $\lambda\lambda 7320, 7330$ have a smaller velocity splitting than [O II] $\lambda\lambda 3726, 3729$. The auroral and nebular lines of [S II], [S III], and [Ar III] differ by of order 1 km/s, which is similar to the typical dispersion (standard deviation) of the line splitting in Table 8 for many ions. As we shall see, the cases of [N II] and [O II] arise due to contamination of the auroral lines from recombination (§3.3), while the difference for [O III] appears to be real and due to the ionization structure (§3.3). For the [S III] lines (similar velocity splitting) and the [Ar IV] lines, atmospheric absorption confuses the issue (details in Appendix A).

In the bottom panel of Figure 5, we add the permitted lines of O I, C II, N II, O II, and Ne II. Though the lines from these ions span a large range in ionization energy, they all have similar velocity splitting. In particular, the O II and Ne II lines arise from O^{2+} and Ne^{2+} ions, respectively, as do the [O III] and [Ne III] lines. Though the Ne II and [Ne III] lines have similar velocity splitting, the O II and [O III] lines do not. Since we expect all lines emitted by a given ion to share the same volume of the nebula, the different velocity splitting for the O II and [O III] lines is striking. Similarly, the C II and N II lines would normally be expected to present veloc-

ity splittings similar to those of He I, [S III], [Cl III], and [Ar III], but the velocity splitting for these lines is systematically too low given their ionization potentials, by $\sim 3 - 5$ km/s.

The velocity splitting for these lines, 44 – 45 km/s, is very similar to that of the C III, N III, and [Ar IV] lines at 43 – 44 km/s. Figure 6 presents examples of the PV diagrams of the C II, N II, O II, and Ne II lines. It is notable that the morphology of these PV diagrams differs from the morphologies of the PV diagrams for [Ar IV] $\lambda 4740$ (Figure 4) or those in Figure 46 that have very similar velocity splitting, indicating that they arise from a different volume of plasma. The PV diagrams illustrate more clearly than the Wilson diagram (Figure 5) that the kinematics of the C II, N II, O II, and Ne II lines is different from the kinematics of other lines of either the same ionization potential or velocity splitting. (See Figures 4 and 47, respectively, for the PV diagrams of the [O III] $\lambda 4959$ and [Ne III] $\lambda 3869$ lines.)

Finally, there is a cluster of permitted lines from H I, O I, and Si II, at approximately 14 eV and 46 km/s (the auroral lines of [O II] and [N II] also fall here; middle and bottom panels of Figure 5). The case of H I is the simplest to understand. Given that it is emitted throughout the whole nebular volume, its velocity splitting should be similar to that of other lines that sample the majority of this volume, such as the lines of He I, [O III], and [Ne III]. Indeed, this is the case, so its deviation from the general trend is not unexpected.

Second, the O I $\lambda\lambda 7771, 9265$ lines in question are quintuplet lines, whose lower level is the meta-stable $3s^5S^o$ state that can decay to the O^0 ground state only through a forbidden transition. Hence, they cannot be excited by fluorescence from the ground state and so are likely the result of recombination. Figure 7 compares the PV diagrams of these lines with the emission from O II $\lambda 9982$, obtained simultaneously. The morphology and velocity splitting of the PV diagrams for these O I lines, especially O I $\lambda 9265$ (least affected by sky lines), is very similar to that of O II $\lambda 9982$. So, it appears that the O I $\lambda\lambda 7771, 9265$ lines arise from the same plasma that emits the O II lines. [García-Rojas et al. \(2022\)](#) find the same result.

Third, the Si II lines involved are Si II $\lambda\lambda 5041, 6347, 6374$ from multiplets V5 (5041Å) and V2, respectively, and we detect them with good S/N (see Figure 51). We suspect that these lines in NGC 6153 are partly excited by recombination and partly by fluorescence as a minority ion in zones of higher ionization. So, the velocity splitting from these Si II lines in NGC 6153 may not reflect the kinematics of the volume where Si^{2+} is the dominant ionization state, which is how this data point

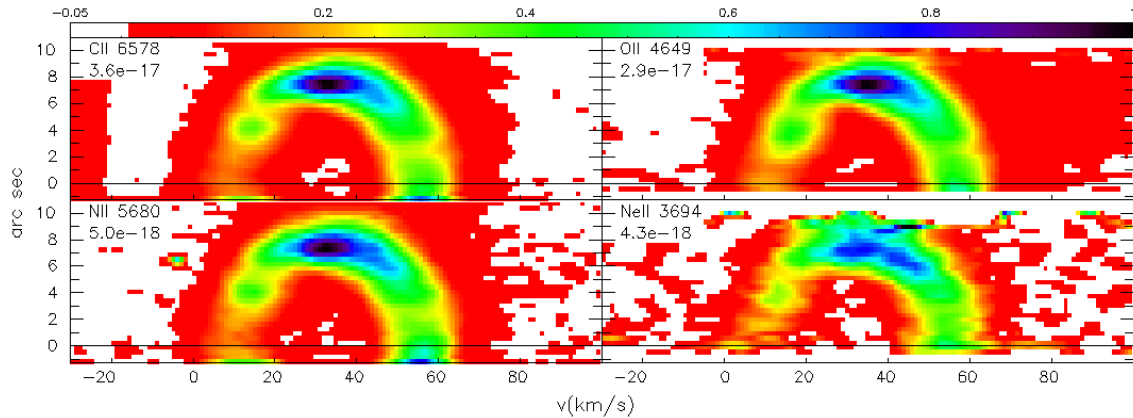


Figure 6. These panels present the PV diagrams in the lines of C II $\lambda 6578$, O II $\lambda 4649$, N II $\lambda 5680$, and Ne II $\lambda 3694$. Although the PV diagram for Ne II $\lambda 3694$ is of lower S/N, all of the lines share the same morphology, indicating that they arise from the same volume of plasma. Note that the morphology of these PV diagrams is quite different from the morphology of the PV diagrams for [O III] $\lambda\lambda 4959, 5007$ and [Ne III] $\lambda 3869$ (Figure 4, Figure 47, Figure 48). They are more similar to the PV diagrams in Figure 46, but their overall shape is even more circular because of their larger velocity splitting.

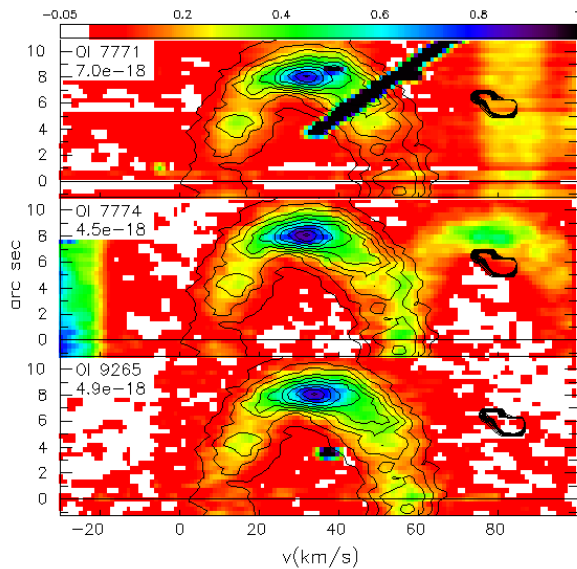


Figure 7. These panels present the PV diagrams of the O I $\lambda\lambda 7771, 7774$ (7775 to the red), and 9265 lines. In all cases, some sky lines have been subtracted, which is what produces the faint vertical bands. The black streak is a cosmic ray. The contours are of the intensity of the emission of the O II $\lambda 9982$ line. In this and following figures, we plot the contours at 10%, 20%, ..., 90% of the maximum intensity. The kinematics of these O I quintuplet lines are compatible with those of the O II $\lambda 9982$ line.

is plotted in Figure 5. We provide more details in Appendix A.

The general trend of a velocity splitting that decreases as the ionization energy of the parent ion increases in Figure 5 is the expected one. This trend defines what we refer to as the *normal nebular plasma*. There are two novelties though. First, the auroral forbidden lines

of [O II], [N II], and [O III] clearly have lower velocity splitting than their nebular counterparts, the first two due to contamination from recombination and the last due to real temperature structure (§3.3). This also occurs for [Ar IV], but may be due to atmospheric absorption. Second, the lines of O I, C II, N II, O II, and Ne II share a common velocity despite spanning a large range in the ionization energy of the parent ions. These lines appear to define a second kinematic component that does not participate in the general trend and which we call the *additional plasma component*.

3.2. Physical conditions

In the following subsections, we study the temperature and density in the nebular shell of NGC 6153 based upon a variety of methods. Table 9 summarizes these results. The temperatures derived from forbidden lines and the He I lines are substantially higher than the temperatures derived using the permitted lines of N II and O II. Likewise, a dichotomy exists concerning the density, with the N II and O II lines indicating higher densities than other methods. Thus, the physical conditions reflect the results of the kinematics, i.e., that two plasma components are present.

3.2.1. Thermal broadening of line profiles

Ions belonging to the same plasma component should share common spatial, velocity, density, and temperature structures provided that they occupy the same (or similar) volume within the nebula. Even so, emission lines from two ions that share the same volume of the nebula will have different PV diagrams if they have dif-

Table 8. Line splitting

Parent	E_{ion}	Velocity splitting	Lines
	(eV)	(km/s)	
H ⁺	13.6	47.37 ± 0.48	H I λλ3770, 3797, 3835, 3970, 4101, 4340, 4861, 6563, 9229, 9545, 10049
He ⁺	24.6	48.51 ± 0.75	He I λλ3187, 3614, 3965, 4026, 4387, 4471, 4713, 4922, 5015, 5876, 6678, 7281
He ²⁺	54.4	41.09 ± 1.00	He II λλ3203, 4541, 4686, 4859, 5411, 6560, 10123
C ⁰	0.0	47.23 ± 0.95	[C I] λλ9850 (nebular)
C ²⁺	24.4	44.48 ± 0.46	C II λλ4267, 5342, 6151, 6461, 6578, 7231, 9903
C ³⁺	47.9	44.4 ± 1.8	C III λ4647
C ⁴⁺	64.5	38.67 ± 0.54	C IV λλ5801, 5811
N ⁺	14.5	52.72 ± 0.18	[N II] λλ6548, 6583 (nebular)
N ⁺	14.5	46.4	[N II] λ5755 (auroral)
N ²⁺	29.6	45.0 ± 1.1	N II λλ4035, 4041, 5666, 5676, 5680, 5686, 5710
N ²⁺	54.4	43.92 ± 0.29	N III λλ4097, 4103, 4634, 4641 (Bowen fluorescence)
N ³⁺	47.4	43.26 ± 0.63	N III λλ4379, 5147
O ⁰	0.0	51.30 ± 0.38	[O I] λλ6300, 6364 (nebular)
O ⁺	13.6	49.90 ± 0.30	[O II] λλ3726, 3729 (nebular)
O ⁺	13.6	46.32 ± 0.04	[O II] λλ7319, 7320, 7330, 7331 (auroral)
O ⁺	13.6	45.1 ± 1.4	O I λλ7771, 7774, 9265
O ²⁺	35.1	47.2	[O III] λ4959 (nebular)
O ²⁺	35.1	44.6	[O III] λ4363 (auroral)
O ²⁺	35.1	44.58 ± 0.96	O II λλ4069.6, 4069.9, 4072, 4076, 4084, 4089, 4317, 4349, 4366, 4591, 4596, 4639, 4649, 4662, 4676, 6500.8, 6501.4, 9982
O ²⁺	54.4	43.18 ± 0.69	O III λλ3133, 3299, 3312, 3340, 3444, 3754, 3759 (Bowen fluorescence)
O ³⁺	54.9	42.6 ± 1.2	O III λ3260, 3707
O ³⁺	54.9	41.43 ± 0.98	O III λλ3757, 3774, 5592 (charge exchange)
Ne ²⁺	41.0	46.02 ± 0.32	[Ne III] λλ3869, 3967 (nebular)
Ne ²⁺	41.0	45.68 ± 0.55	Ne II λλ3335, 3568, 3694, 5130, 9096
Ne ³⁺	63.5	39.3 ± 2.0	[Ne IV] λ4724 (nebular)
Si ⁺	8.2	50.5	Si I λ6486
Si ²⁺	16.3	46.67 ± 0.60	Si II λλ5041, 6347, 6371
S ⁺	10.4	53.03 ± 0.50	[S II] λλ6716, 6731 (nebular)
S ⁺	10.4	52.4	[S II] λ4069 (auroral)
S ²⁺	23.3	49.6	[S III] λλ9531 (nebular)
S ²⁺	23.3	50.27 ± 0.37	[S III] λ6312 (auroral)
Cl ⁺	13.0	49.1 ± 2.7	[Cl II] λλ8578, 9123 (nebular)
Cl ²⁺	23.8	50.26 ± 0.30	[Cl III] λλ5517, 5537 (nebular)
Cl ³⁺	39.6	46.27 ± 0.47	[Cl IV] λλ7530, 8045 (nebular)
Ar ²⁺	27.6	49.02 ± 0.22	[Ar III] λ7135, 7751 (nebular)
Ar ²⁺	27.6	50.4	[Ar III] λ5191 (auroral)
Ar ³⁺	40.7	43.05 ± 0.21	[Ar IV] λλ4711, 4740 (nebular)
Ar ³⁺	40.7	38.7	[Ar IV] λ7262 (auroral)
Ar ⁴⁺	59.8	36.87 ± 0.43	[Ar V] λ6435, 7006 (nebular)
K ³⁺	45.7	47.78 ± 0.52	[K IV] λλ6101, 6795 (nebular)
Mn ⁴⁺	51.4	48.29 ± 0.29	[Mn V] λλ5701, 5861, 6083, 6393

ferent intrinsic fine structure or different thermal line widths. Therefore, we can exploit differences in atomic mass to infer the plasma temperature for ions that share the same nebular volume if we can account for the differences in the intrinsic line structure of the two lines (e.g., Courtès et al. 1968; Dyson & Meaburn 1971; García-Díaz et al. 2008). Determining the temperature in this way circumvents issues related to atomic data, but requires comparing only ions that share the same nebular volume.

We will consider lines arising from ions of H^+ , He^+ , and O^{++} . The latter two are expected to occupy very similar volumes within the nebula, especially since NGC 6153 is highly ionized and optically thin. The volume of the nebula occupied by H^+ will differ from that occupied by He^+ and O^{++} , but the effect of this difference is predictable and clear: the PV diagrams for lines from H^+ will present an excess at low expansion velocities and near the central star (the He^{2+} zone) compared to PV diagrams for lines arising from He^+ and O^{++} . The sensitivity of the process depends upon the difference in atomic mass, so it is most instructive to compare H and He with heavy elements. The case of O^{++} allows us to extend our results to the permitted lines of C II, O II, N II, and Ne II. In order to minimize instrumental and observational effects, we consider only lines from the CD2 wavelength interval, for which the slit's position angle was closest to the parallactic angle, so they suffer least from differential atmospheric refraction.

The width observed for an emission line will depend upon the velocity structure of the nebula, the instrumental resolution, the thermal broadening, and the intrinsic line structure. The thermal and instrumental broadening are Gaussian or closely so in profile, so we approximate the line width as $\sigma^2 = \sigma_{neb}^2 + \sigma_{ins}^2 + \sigma_{th}^2 + \sigma_{fs}^2$, where σ_{neb} is the contribution due to the nebula's kinematic structure, σ_{ins} the instrumental broadening, σ_{th} the thermal broadening, and σ_{fs} the fine structure of the emission line itself.

The effect of atomic mass appears through the thermal broadening of the lines emitted by a given ion. The thermal width is given by $\sigma_{th} = \sqrt{82.5((10^{-4}T_e)/m_{ion})}$, where T_e is the temperature of the plasma (K) and m_{ion} is the mass of the ion (atomic mass units; García-Díaz et al. 2008). Thus, the difference in thermal line width can be accounted for by convolving the PV diagram of the emission line from the more massive ion with a Gaussian to account for the difference in atomic mass between it and the ion with lower atomic mass.

The differences in the line structure can always be accommodated if one of the lines is a single, spectrally-resolved emission component. In that case, we can mod-

ify the PV diagram of the single line to match the line structure of the other, reflected in its PV diagram: Multiple copies of the single line are shifted and scaled appropriately to mimic the structure of the line with multiple components.

The H I and He I triplet lines have substructure that must be taken into account. The H I Balmer lines have 7 components, spread over a small range in velocity (Clegg et al. 1999). The seven components divide into two groups whose spread in velocity is significantly less than the difference in velocity between the two groups (blue and red). Within the blue group, about 80% of the total intensity is split between two components while, within the red group, a single component accounts for about 80% of the total intensity (e.g., Fig. 1 of Clegg et al. 1999). We adopt the fraction of the emission from each group from Clegg et al. (1999). The He I lines are either triplet or singlet states. The triplets are formed by three ($n^3S - n'^3P$) or six ($n^3D - n'^3P$) individual transitions; all but one conform a blue group spread over 1-3 km/s while the last transition falls 10-20 km/s to the red (Van Hoof 2018). We follow Axner et al. (2004) to determine the relative intensities of the individual transitions in He I, finding that the blue group contains 89% of the total intensity. Within the blue group, two transitions separated by about half of the total spread account for about 72% of its total intensity.

So, we approximate the H I and He I triplet lines as two components, one representing the blue group and the other the red line/group. Two copies of the PV diagram of a single line are created and added together after appropriately shifting them in wavelength and scaling them in flux according to the details of the H I or He I line involved. Then, this model PV diagram is broadened by convolving it with a Gaussian so as to match the thermal width of the H I or He I line. Matching the thermal width is a process of trial and error in which we consider electron temperatures between 3,000 K and 15,000 K. We then compare this model to the observed PV diagram, determining the best thermal broadening by searching for the PV diagram with the most constant ratio.

This kinematic temperature is an emission-weighted mean temperature, measured by the motions of the ions in the plasma. It does not imply that there is a single, uniform temperature within the plasma emitting in the H I, He I, O II, and [O III] lines. The plasma may well contain temperature gradients or small-scale structure, but the PV diagrams inherently reflect the result of that structure. (Given the thermal width of the H I and He I lines, the kinetic temperature will not be very sensitive to small-scale structure.) One worry is that the temper-

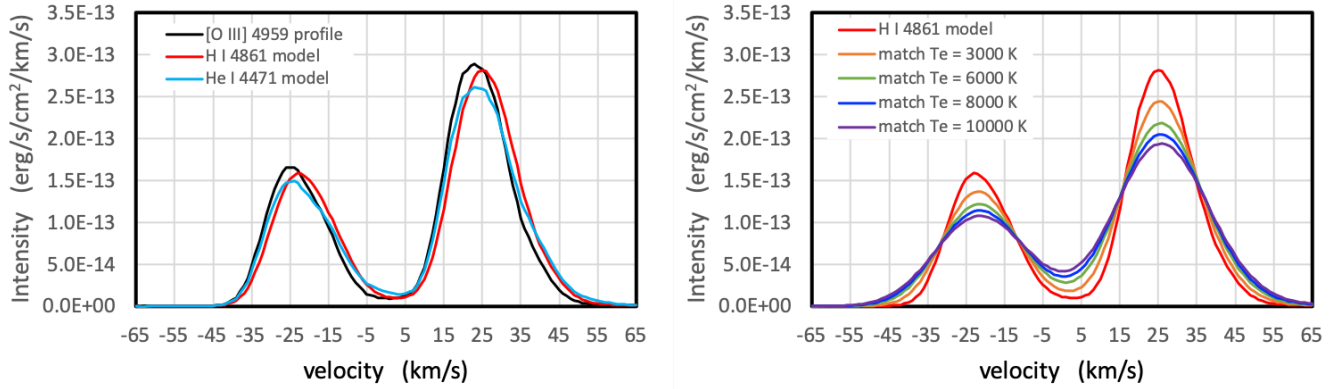


Figure 8. left panel: This plot presents the line profile for the spatial interval used to compute the velocity splitting (see Figure 2) for the [O III] $\lambda 4959$ line as well as the models based upon this line for the H β and He I $\lambda 4471$ lines. Right panel: This plot presents the model of the H β line based upon the [O III] $\lambda 4959$ line from the left panel as well as the profiles of this model after broadening with a Gaussian to match the thermal line width of the H β line for temperatures of 3,000 K, 6,000 K, 8,000 K, and 10,000 K. The latter is the largest modification made to the [O III] line profile.

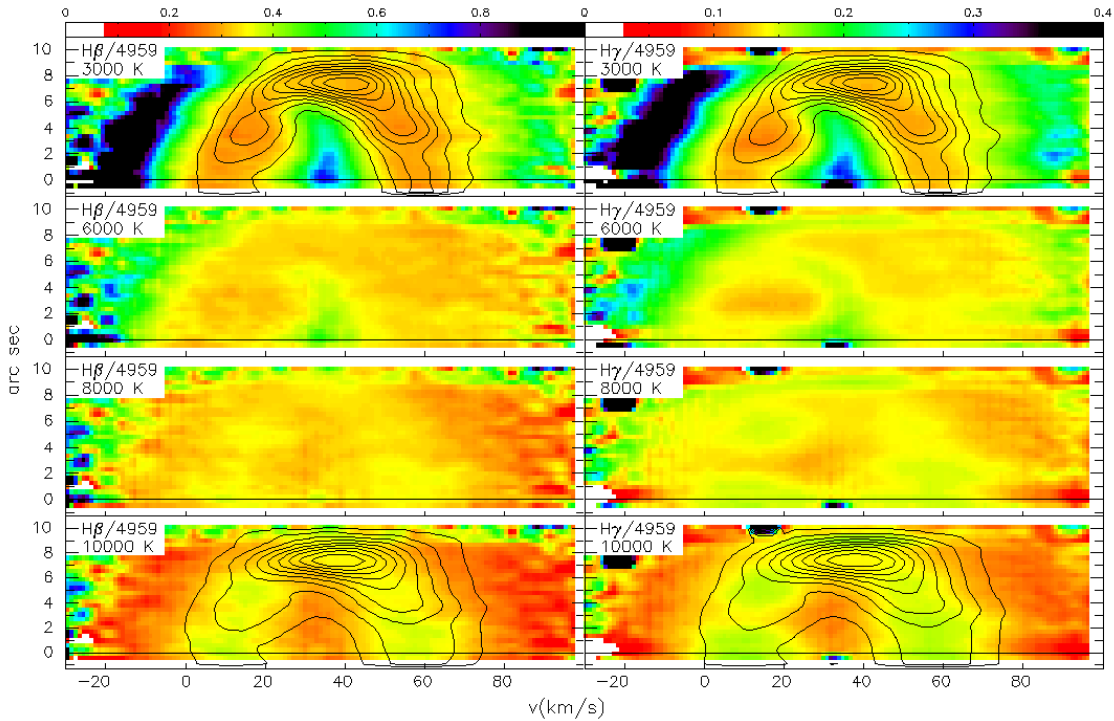


Figure 9. These panels present the ratio of H β (left column) and H γ (right column) with respect to [O III] $\lambda 4959$. The ratio images assume temperatures of 3,000 K, 6,000 K, 8,000 K, and 10,000 K (top to bottom) when broadening the PV diagram of [O III] $\lambda 4959$. In the top row, the contours are those of the PV diagram for [O III] $\lambda 4959$. In the bottom row, the contours are those of H β (left column) and H γ (right column). The ratios best approximate a constant value for a temperature of 8,000 K.

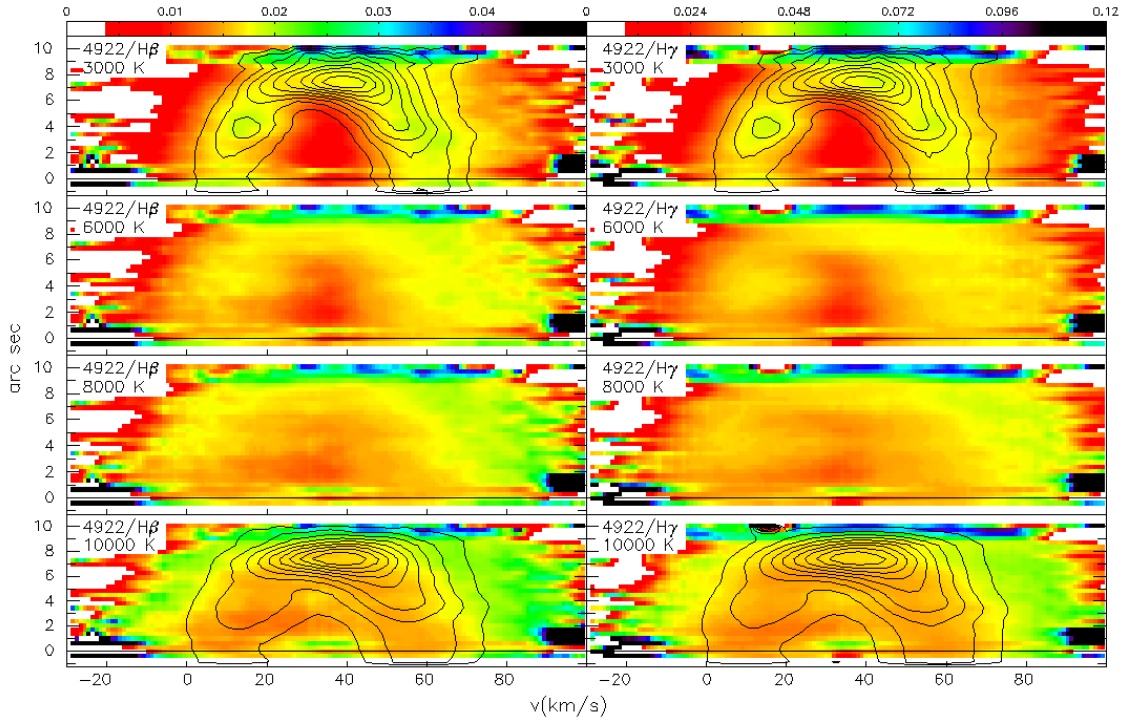


Figure 10. These panels present the ratio of the He I $\lambda 4922$ line with respect to H β (left column) and H γ (right column), assuming temperatures of 3,000 K, 6,000 K, 8,000 K, and 10,000 K (top to bottom). The contours are those of the PV diagram for He I $\lambda 4922$ in the top row, but of H β (left) and H γ (right) in the bottom row. The ratios are most constant when the assumed temperature to broaden the He I lines is 8,000 K.

ature sensitivity varies among the lines considered. The intensity of the [O III] lines increases with increasing temperature, but the intensities of the other lines decreases, an effect that cannot be compensated exactly. To mitigate the issue, we consider only [O III] $\lambda 4959$.

Most of the structure in the line profiles for the lines of the heavy elements is due to the velocity structure of the nebula, not the thermal width of the line (nor the instrumental resolution). For example, the observed line width of [O III] $\lambda 4959$ is slightly more than 18 km/s FWHM. Of this, the thermal broadening contributes 5.4 km/s (supposing a temperature of 10,000 K, less if the temperature is lower), while the instrumental broadening of order 10 km/s. Since these add in quadrature, the broadening due to the velocity structure dominates, amounting to 14 km/s.

Even so, the substantial modifications required to match the [O III] $\lambda 4959$ line to the H I Balmer lines gives the method good sensitivity. The left panel of Figure 8 demonstrates that accounting for the line structure of either $H\beta$ or He I $\lambda 4471$ requires only minor modifications. However, the broadening required to match the thermal line width of a hydrogen line can be substantial, as shown in the right panel of Figure 8, amounting to as much as 20.7 km/s for a temperature of 10,000 K. The modifications required to match the thermal width of a He line to a H line are less important because of the larger thermal widths of the He lines. Likewise, matching the thermal width of an O line to a He line also requires less broadening than illustrated in Figure 8.

Figure 9 compares the PV diagrams of the $H\beta$, $H\gamma$, and [O III] $\lambda 4959$ lines. In the left column, we present the ratio of $H\beta$ with respect to [O III] $\lambda 4959$. (By “[O III] $\lambda 4959$ ”, we mean the model of the $H\beta/H\gamma$ line constructed with the [O III] $\lambda 4959$ PV diagram.) The four panels consider temperatures of 3,000 K, 6,000 K, 8,000 K, and 10,000 K when broadening the PV diagram for [O III] $\lambda 4959$. Since the volumes occupied by H^+ and O^{2+} largely coincide, the ratio should be approximately constant when the appropriate temperature is used to broaden the PV diagram for [O III] $\lambda 4959$. If the assumed temperature is too low, the PV diagram for [O III] $\lambda 4959$ will not be sufficiently broadened, and we expect a minimum in the $H\beta/[O III] \lambda 4959$ ratio where the emission from [O III] $\lambda 4959$ is most intense. Conversely, if the assumed temperature is too high, the PV diagram for [O III] $\lambda 4959$ will be broadened too much, diffusing its emission too far, to velocities too far from and too close to the systemic velocity. In this case, we expect that the $H\beta/[O III] \lambda 4959$ ratio will present a maximum where the $H\beta$ emission is most intense. The main difference in the volumes occupied by H^+ and O^{2+}

is that O^{2+} does not sample as completely as H^+ the innermost volume of the nebular shell occupied by He^{2+} (closest to the central star and with velocities closest to the systemic velocity).

The four panels in the left column of Figure 9 present a clear trend. In the first panel, with [O III] $\lambda 4959$ broadened assuming a temperature of 3,000 K, the ratio varies the most. The $H\beta/[O III] \lambda 4959$ ratio falls strongly at the velocities and spatial positions where the emission from [O III] $\lambda 4959$ is most concentrated (the contour lines) because the PV diagram for $H\beta$ is broader than that of [O III] $\lambda 4959$. As a result, the ratio is too high at the velocities both closest to and farthest from the systemic velocity. As the assumed temperature increases to 6,000 K (second row) and 8,000 K (third row), the ratio better approximates a constant value. For a temperature of 8,000 K, the ratio is very constant. For an assumed temperature of 10,000 K, we see an increase in the ratio at the velocities and positions where the $H\beta$ emission is most intense, implying that the broadening of the [O III] $\lambda 4959$ PV diagram has now gone too far. For a temperature of 10,000 K, the ratio of the $H\beta/[O III] \lambda 4959$ decreases at the velocities that most differ from the systemic velocity, also a result of the [O III] $\lambda 4959$ PV diagram being now too diffuse. Hence, we conclude that a temperature between 6,000 K and 8,000 K is that which best matches the kinematics of the lines of $H\beta$ and [O III] $\lambda 4959$. Comparing the last two panels in the left column of Figure 9, the pattern of the emission from $H\beta$ is also becoming visible in the third panel, for an assumed temperature of 8,000 K. So, the temperature that will best characterize the kinematics of both the $H\beta$ and [O III] $\lambda 4959$ lines will be somewhat below 8,000 K (we return to this in §4.5).

The right column of Figure 9 presents the analogous results for the ratio $H\gamma/[O III] \lambda 4959$. Again, the most constant value of this ratio occurs for an assumed temperature of 8,000 K, though, again, the best temperature is likely to be somewhat lower than this.

In Figure 10, we consider the ratio of the He I $\lambda 4922$ singlet line with respect to $H\beta$ and $H\gamma$ for assumed temperatures of 3,000 K, 6,000 K, 8,000 K, and 10,000 K when broadening the He I $\lambda 4922$ line. For 3,000 K, the He I $\lambda 4922/H\beta$ and He I $\lambda 4922/H\gamma$ ratios indicate that the He I $\lambda 4922$ line is narrower than the H I lines, since the ratio is high where there is He I $\lambda 4922$ emission. To some extent, this persists at 6,000 K, especially considering the He I $\lambda 4922/H\gamma$ ratio. At 8,000 K the two ratios are approximately constant. At 10,000 K, there is a bright rim in the PV diagram of the He I $\lambda 4922/H\beta$ and He I $\lambda 4922/H\gamma$ ratios and the ratios are depressed where the emission from $H\beta$ and $H\gamma$ is strong, all of

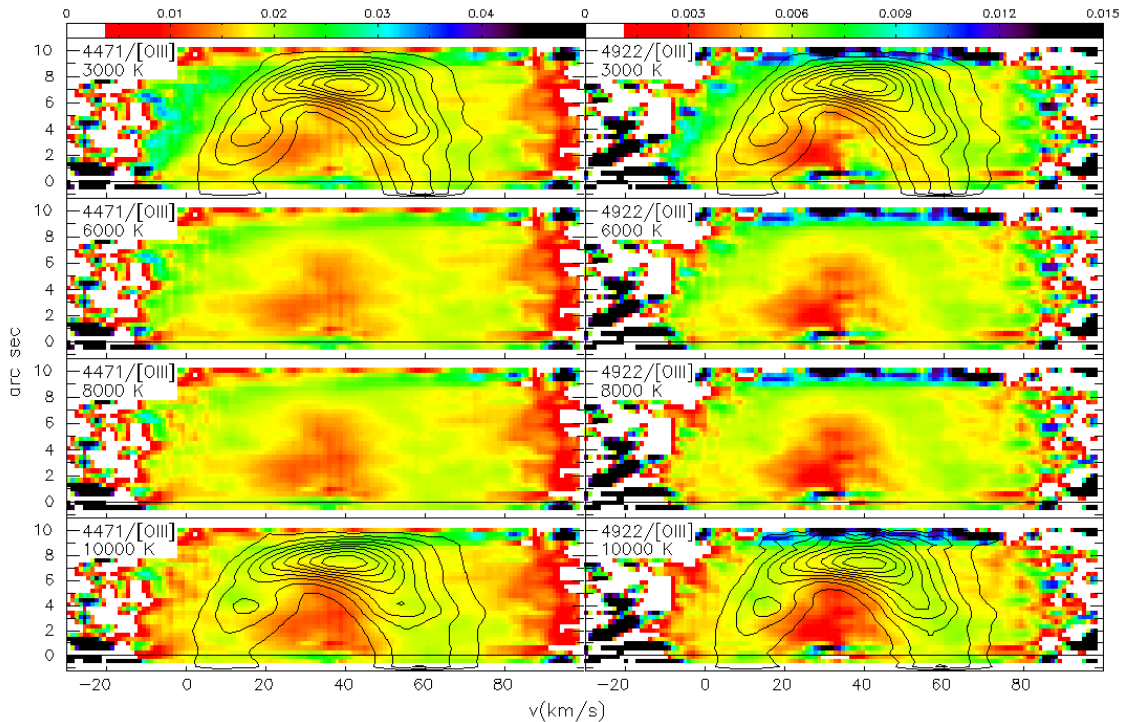


Figure 11. These panels present the ratio of the PV diagram of He I $\lambda 4471$ (left column) and He I $\lambda 4922$ (right column) with respect to [O III] $\lambda 4959$. The ratios assume temperatures of 3,000 K, 6,000 K, 8,000 K, and 10,000 K (top to bottom). In the top row, the contours are those of the PV diagram for [O III] $\lambda 4959$. In the bottom row, the contours are those of He I $\lambda 4471$ (left) and He I $\lambda 4922$ (right). Again, the ratios are most constant for a temperature of 8,000 K.

which indicate that the He I $\lambda 4922$ line is too broad in these cases. Hence, it appears that 8,000 K is the temperature that best permits matching the He I $\lambda 4922$, $H\beta$, and $H\gamma$ PV diagrams. In the first three rows of Figure 10, there is a depression in the He I $\lambda 4922/H\beta$ and He I $\lambda 4922/H\gamma$ ratios for the velocities closest to the systemic velocity and spatial positions closest to the central star because He^+ is supplanted by He^{2+} as the dominant ionization stage of helium in the innermost part of the nebular shell.

We present the ratios of the PV diagrams of He I $\lambda 4471$ (left column) and He I $\lambda 4922$ (right column) with respect to that of [O III] $\lambda 4959$ in Figure 11. These ratios are computed after broadening the [O III] $\lambda 4959$ line assuming temperatures of 3,000 K, 6,000 K, 8,000 K, and 10,000 K. Regardless of the temperature assumed, there is a depression in the He I $\lambda 4471/[O III] \lambda 4959$ and He I $\lambda 4922/[O III] \lambda 4959$ ratios at velocities near the systemic velocity and positions near the central star. This arises because (1) O^{2+} is the dominant ionization stage of oxygen in the central part of the nebula while He^+ is not and (2) the smaller thermal widths better resolve this central region. Outside this central zone, the He I $\lambda 4471/[O III] \lambda 4959$ and He I $\lambda 4922/[O III] \lambda 4959$

ratios vary by approximately 10% for temperatures of 6,000 K and 8,000 K.

Figure 12 presents the PV diagrams for the lines of O II $\lambda 4649$ and [O III] $\lambda 4959$ as well as the ratio of these two lines. Both lines arise from the O^{2+} ion and are single lines, so there is no correction for either line structure or thermal broadening, assuming that they arise from the same plasma component. Hence, the ratio O II $\lambda 4649/[O III] \lambda 4959$ is of no use in determining the temperature of the plasma from which these lines arise. However, since this ratio is very non-uniform, it clearly indicates that the two lines do not arise from the same plasma component.

Given that all of these PV diagrams are very similar to O II $\lambda 4649$, the C II, N II, O II, and Ne II lines presumably all arise in the same plasma component. In Figure 13, we test this hypothesis. All of the panels in Figure 13 present ratios of different C II, N II, O II, and Ne II lines, all of which yield approximately constant values. In calculating these ratios, we do not correct for thermal broadening since the broadening involved varies from 0.7 to 1.3 km/s over the 3,000–10,000 K temperature range. The O II $\lambda 4662/\text{O II } \lambda 4649$ ratio, is a sanity check to test the method. The two lines are from the same ion and the same spectral order. In four of the six

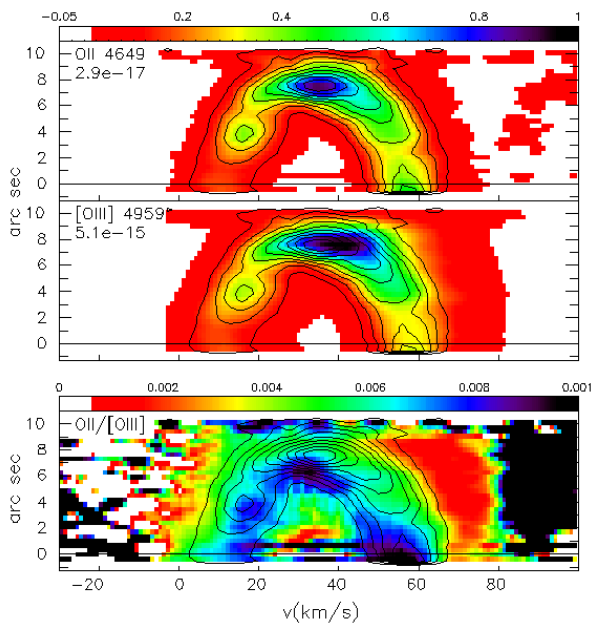


Figure 12. These panels present the PV diagrams for the O II $\lambda 4649$ and [O III] $\lambda 4959$ lines and the ratio O II $\lambda 4649$ /[O III] $\lambda 4959$. The contours represent the intensity of the O II $\lambda 4649$ line. Both lines are single lines from the CD2 wavelength interval from the same ion, so there are no corrections for the intrinsic line structure or thermal broadening (supposing they arise from the same plasma component). The solid black color at right is due to contamination of the PV diagram of O II $\lambda 4649$ by C III $\lambda 4650$.

ratios, the lines are from the same wavelength interval (CD2 in three cases, CD3 in the other), so differential atmospheric refraction should not be a problem. In two cases, N II $\lambda 5680$ /O II $\lambda 4649$ and Ne II $\lambda 3694$ /O II $\lambda 4649$, the ratios compare lines from wavelength intervals CD3 and CD1 with respect to CD2. These are the cases where the ratio varies most. The basic result of Figure 13 is that ratios of the lines of C II, N II, O II, and Ne II produce constant values, as expected if these lines arise in the same plasma component.

Figures 9-11 argue that the kinematics of H I, He I, and [O III] lines are compatible with these emission lines arising from the same plasma component whose temperature is $\sim 8,000$ K. On the other hand, Figure 12 indicates that the O II $\lambda 4649$ does not arise from the same plasma component that gives rise to the H I, He I, and [O III] lines. Figure 13 indicates that this line, as well as other lines of C II, N II, O II, and Ne II, have kinematics that are compatible with an origin in a common plasma component. So, by extension, all of these lines arise from a different plasma component from that producing the H I, He I, and [O III] lines.

3.2.2. Forbidden lines

We construct PV diagrams for the electron temperature and density diagnostics from collisionally-excited lines. Since we resolve both the spatial structure along the slit and the velocity structure along the line of sight, regions expected to have higher temperatures, such as those close to the central star, have different PV coordinates from other volumes of the nebula. We compute the physical conditions using PyNeb (Luridiana et al. 2015) to convert an intensity ratio into an electron temperature or density.

We consider the electron temperatures derived from the [O III] and [Ar III] lines as well as the electron densities derived from the [S II], [Cl III] and [Ar IV] lines. As we shall see (§3.3), the [N II] and [O II] forbidden lines have an important excitation component due to recombination, in addition to the usual collisional excitation process, so we defer their discussion for later. Finally, due to the radial velocity of NGC 6153 at the time of the observations, the [S III] $\lambda\lambda 9069,9531$ lines coincided with strong telluric absorption lines, so they cannot be used to determine a reliable electron temperature (Stevenson 1994).

Figure 14 presents the PV diagrams of the [O III] $\lambda\lambda 4363,4959$ lines as well as the PV diagrams of the [O III] temperature. In computing the [O III] temperature, we adopt an electron density of $4,000 \text{ cm}^{-3}$ (atomic data: Table 1). The [O III] temperature map presents three regimes. In the main shell, there is a slight gradient from the outermost parts of the nebula (largest distance from the central star, largest velocities w.r.t. the systemic velocity) to the innermost part (spatial positions closer to the central star, velocities near the systemic velocity), that varies only slightly $9,000 - 10,000$ K. Inside the main shell, the plasma is hotter, $10,000 - 11,000$ K. In the diffuse emission beyond the main shell at the largest recession velocities, the temperature is lowest $8,000 - 9,000$ K.

Figure 15 presents the PV diagrams of the [Ar III] $\lambda\lambda 5191, 7135, 7751$ lines as well as the PV diagrams of the temperature based upon the ratios of [Ar III] $\lambda\lambda 5191/7135$ and [Ar III] $\lambda\lambda 5191/7751$. In this case, lines from different wavelength intervals must be used (CD3b and CD4b). Again, we adopt an electron density of $4,000 \text{ cm}^{-3}$ (atomic data: Table 1). The [Ar III] temperature map is limited to the main shell and the filament on its receding side. The [Ar III] temperature map is more uniform than the [O III] temperature, though with larger uncertainties, and slightly lower, by ~ 500 K.

Turning to the electron density indicators, Figure 16 presents the PV diagrams of the [S II] $\lambda\lambda 6716,6731$

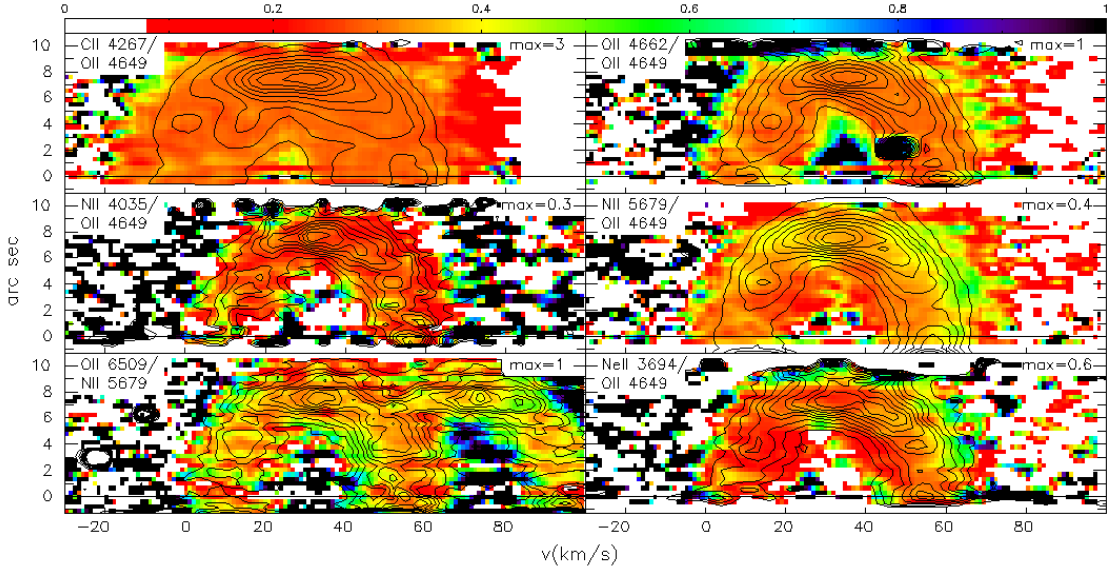


Figure 13. These panels present the ratios of PV diagrams C II, N II, O II, and Ne II lines, as indicated in each panel. In all panels, the contours are of the intensity of the numerator. No correction for thermal broadening was applied to any of the PV diagrams. The C II $\lambda 4267$ /O II $\lambda 4649$ and O II $\lambda \lambda 6509, 6510$ /N II $\lambda 5680$ ratios required modeling multiple C II and O II lines. The horizontal bands in the O II $\lambda 6509$ /N II $\lambda 5680$ ratio are due to the poor background subtraction for O II $\lambda 6509$. The ratio of PV diagrams all approximate a constant value, indicating that these permitted lines of C II, N II, O II, and Ne II arise from the same plasma component.

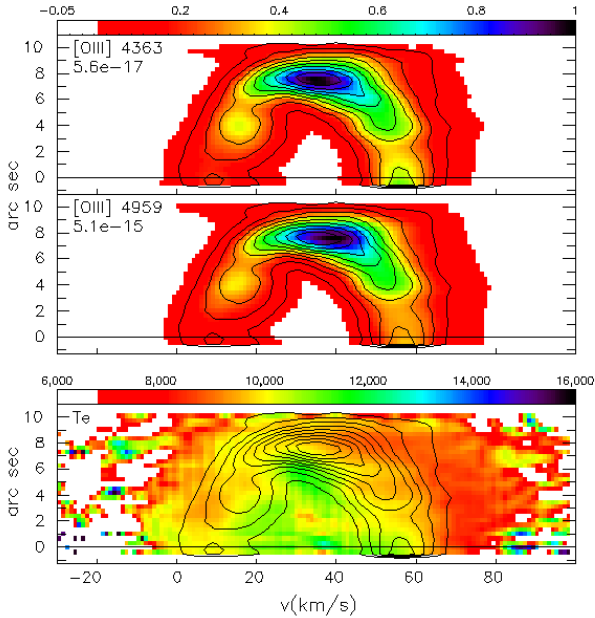


Figure 14. These panels present the PV diagrams of the [O III] $\lambda 4363, 4959$ lines and the [O III] temperature (bottom). The contours in all panels are those of the intensity of [O III] $\lambda 4363$. The white colour in the temperature map includes positions with zero values or unphysical values. There is a mild temperature gradient from the zone close to the central star (near the systemic velocity and in the middle of the slit) to zones farther away (the smallest and largest velocities and towards the top of the slit).

lines and of the [S II] electron density. To compute the electron density, we assume an electron temperature of 10,000 K (atomic data: Table 1). There is a clear gradient in the electron density implied by the [S II] $\lambda \lambda 6716/6731$ line ratio, with lower densities towards the periphery of the object, at either the velocities that differ most from the systemic velocity or at the greatest distance from the central star. The variation in electron density appears to exceed a factor of 2, from approximately $2,000 \text{ cm}^{-3}$ to $4,000 - 5,000 \text{ cm}^{-3}$. The filament on the receding side of the main shell that is the brightest feature of the [S II] $\lambda \lambda 6716, 6731$ PV diagrams is of low density, so it is presumably bright due to a change in the ionization stage for sulfur. This feature is not evident in the $H\alpha$ line (Figure 2), so it is presumably of low mass.

Figure 17 presents the PV diagrams of the [Cl III] $\lambda \lambda 5517, 5537$ lines and the [Cl III] density. Again, we assume an electron temperature of 10,000 K (atomic data: Table 1). The PV diagram of the [Cl III] density is quite uniform over the entire area that includes [Cl III] emission. There is, however, a “red border” around the outer edge of the area with [Cl III] emission, as if the density drops at the outer edge of the Cl^{2+} zone. By and large, this is congruent with the variation in the density as traced by the [S II] lines, since the [S II] lines trace plasma with a lower degree of ionization. The higher [Cl III] density throughout most of the Cl^{2+} zone agrees

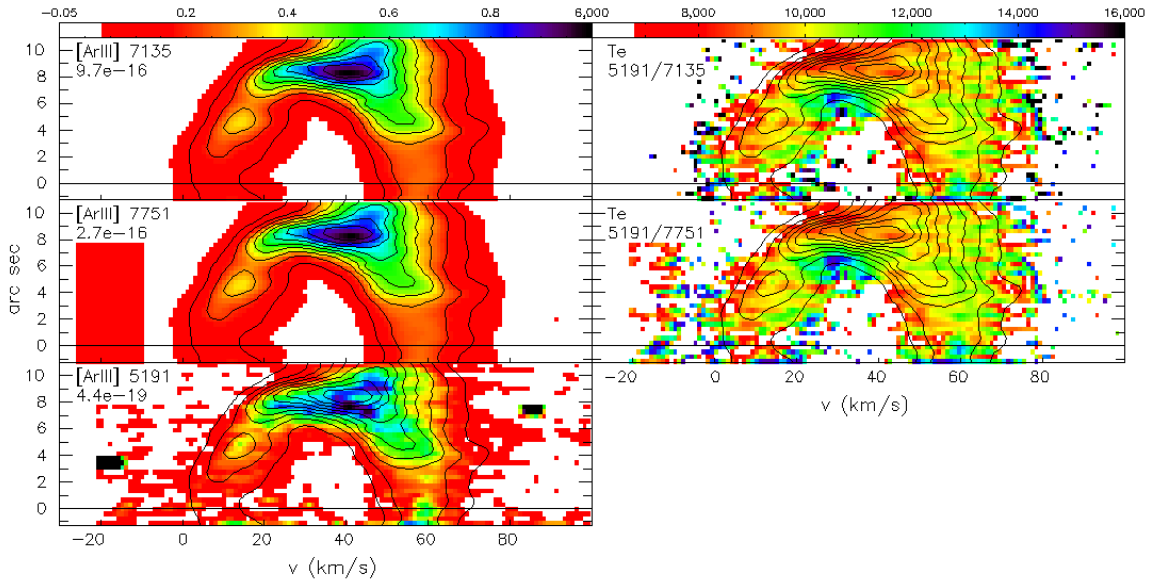


Figure 15. These panels present the PV diagrams of the lines of [Ar III] λ 7135,7751,5191 the [Ar III] temperature from the [Ar III] λ 5191/7135 and 5191/7751 line ratios in the right column. The contours are of the intensity of the [Ar III] λ 7135 line. The color scale in the right column is the same as used for the [O III] temperature in Figure 14.

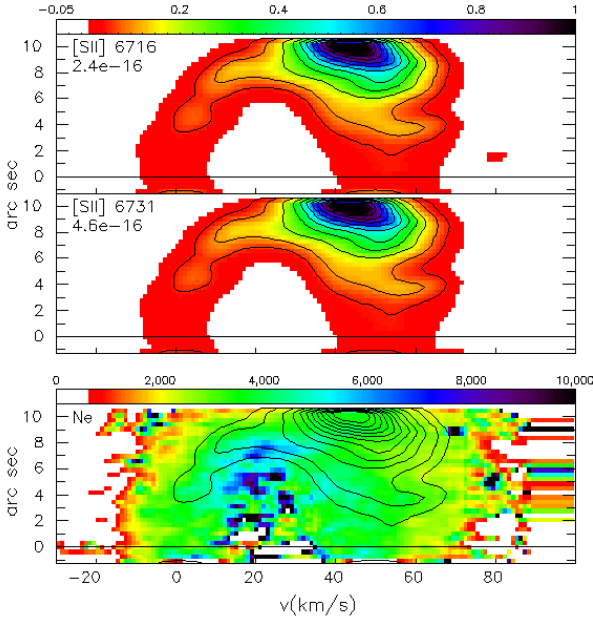


Figure 16. These panels present the PV diagrams of the [S II] λ 6716,6731 lines and of the [S II] density. In all panels the contours are of the [S II] λ 6716 line intensity. The white color in the PV diagram of the [S II] density represent non-physical values or where there is no [S II] emission. The color scale for the density spans the range 0 – 10,000 cm^{-3} .

with the [S II] electron density at the velocities and spatial coordinates in common. However, one discrepancy is the higher density implied for the filament on the receding side of the main shell.

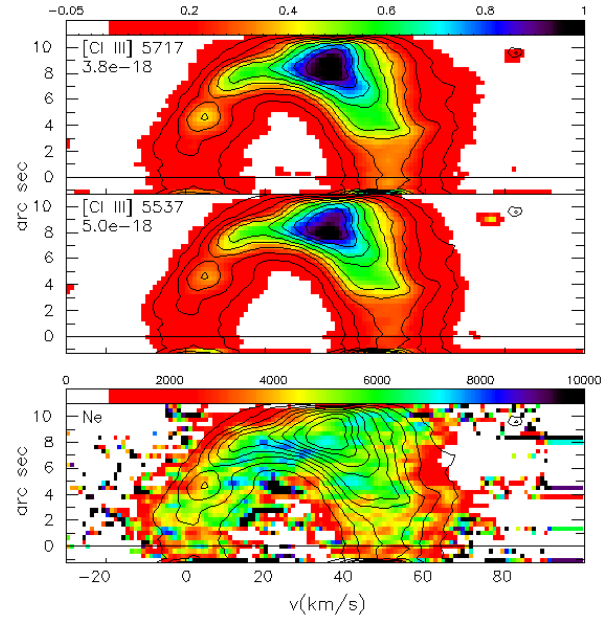


Figure 17. These panels present the PV diagrams of the [Cl III] λ 5717,5537 lines and of the [Cl III] density. In all panels the contours are of the [Cl III] λ 5717 line intensity. The white color in the PV diagram of the [Cl III] density represent non-physical values or where there is no [Cl III] emission. The color scale for the density spans the range 0 – 10,000 cm^{-3} .

Figure 18 presents the PV diagrams of the [Ar IV] λ 4711,4740 lines and the [Ar IV] electron density (assuming an electron temperature of 10,000 K; atomic data: Table 1). The PV diagram of the [Ar IV] electron

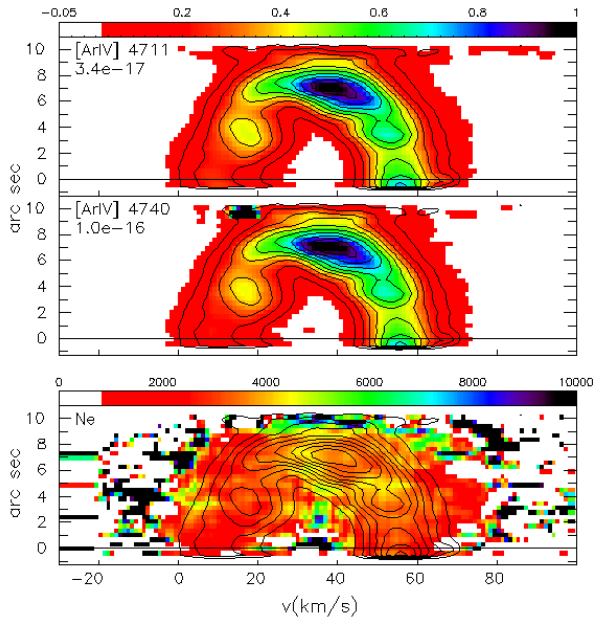


Figure 18. These panels present the PV diagrams for the lines of [Ar IV] $\lambda\lambda 4711, 4740$ and of the [Ar IV] density. In all panels, the contours are of the intensity of the [Ar IV] $\lambda 4711$ line. The white color in the PV diagram of the [Ar IV] density represent non-physical values or where there is no [Ar IV] emission. The color scale for the density spans the range $0 - 10,000 \text{ cm}^{-3}$.

density is very uniform. However, the electron density implied by the [Ar IV] lines is substantially lower than that found from the [Cl III] or [S II] lines, even for the velocities and spatial coordinates in common, more like the low densities found at the periphery from [S II]. Perhaps, a different atomic data set could resolve the issue. It is unlikely due to uncertainty in the line intensity ratio, since it implies a 20% change, which we think unlikely for such strong lines.

Based upon the [S II] and [Cl III] densities, the density throughout most of the main shell of NGC 6153 appears to be approximately $4,000 - 5,000 \text{ cm}^{-3}$ with a lower density region at the extreme velocities and distance from the central star (Figures 16 and 17). The electron density implied by the [Ar IV] lines is about a factor of 2 lower throughout the nebular volume in common with the [S II] and [Cl III] emission.

3.2.3. Permitted lines

The intensities of high- n Balmer and Paschen lines may be used to infer the electron density, though this requires adopting an electron temperature. We use the theoretical line emissivities for Case B (atomic data: Table 1) and the line intensities measured from the 1-D spectrum (Table 3).

Figure 19 presents the intensities of the high- n Balmer lines relative to the intensity of $H\beta$. We consider temperatures of 1,000 K (left panel) and 10,000 K (right panel) as illustrative of the range of relevant values. The H14 line (H I $\lambda 3721$) has an anomalously high intensity, presumably due to contamination ([S III] $\lambda 3721$). As the temperature increases, so does the implied electron density, but the implied range of electron densities is modest, $< 1,000$ to $< 10,000 \text{ cm}^{-3}$ for this temperature range.

Figure 20 presents the intensities of the high- n Paschen lines relative to the intensity of $H\beta$ (Table 3). We consider the same representative electron temperatures. In this case, an electron density of $1,000 \text{ cm}^{-3}$ is found at a temperature of 1,000 K, but the implied electron density is higher at 10,000 K, with $10,000 \text{ cm}^{-3}$ being perhaps the most representative value, except for the highest Paschen lines. Given the difficulty of measuring the intensities of the highest Paschen lines accurately, due to both line crowding and telluric absorption, we shall give the electron density derived from them lower weight. Generally, the H I lines appear to indicate densities of $\lesssim 10,000 \text{ cm}^{-3}$.

The He I lines also permit us to set limits on the electron temperature and density in NGC 6153 (atomic data: Table 1). The ratio of $nS - n'P$ transitions to $nD - n'P$ transitions are sensitive to the electron temperature. The ratios of like transitions, $nS - n'P$ to $n''S - n'P$ or $nD - n'P$ to $n''D - n'P$, have some limited sensitivity to density. Here, we use the triplet lines He I $\lambda 4713$ ($4^3S - 2^3P$) and He I $\lambda\lambda 4026, 4471, 5876$ ($nD - 2^3P$; $n = 5, 4, 3$, respectively) to illustrate the process. (He I $\lambda 4713$ is the faintest of these lines.)

In the top row of Figure 21, we present the ratios of the the PV diagrams of He I $\lambda 4713$ line to the He I $\lambda\lambda 4026, 4471, 5876$ lines to set limits upon the electron temperature. As shown, these line ratios are not corrected for reddening. The contours are of intensities of the He I $\lambda\lambda 4026, 4471, 5876$ lines (the denominator of the ratio). The line ratios are generally uniform, except perhaps the emission from the approaching side of the main shell in the He I $\lambda\lambda 4713/4026$ ratio. Note that this part of the He I $\lambda 4026$ (4026.2\AA) profile suffers a slight contamination due to the He II $\lambda 4025.6$ line that contaminates the emission from the approaching side of the main shell.

The three panels in the middle row of Figure 21 present statistics for the He I $\lambda\lambda 4713/4026$, He I $\lambda\lambda 4713/4471$, and He I $\lambda\lambda 4713/5876$ ratios (left to right) for the pixels that exceed 10%, 20%, ..., 90% of the intensity of the maximum intensity in the PV diagrams of the He I $\lambda\lambda 4026, 4471, 5876$ lines, respectively.

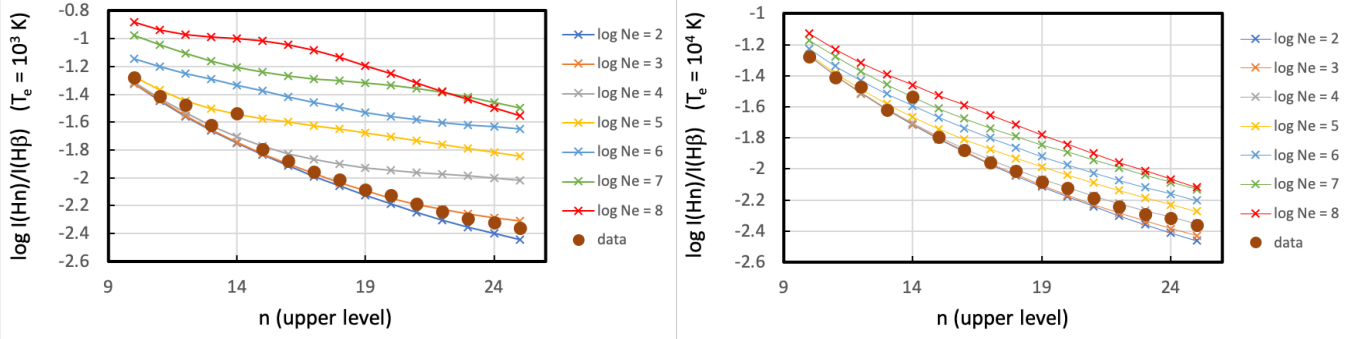


Figure 19. These panels present the intensities of reddening-corrected, high- n Balmer lines with respect to the intensity of $H\beta$ as a function of the upper level for assumed electron temperatures of 1,000 K (left) and 10,000 K (right). The implied densities are between $< 1,000 \text{ cm}^{-3}$ and $\sim 10,000 \text{ cm}^{-3}$.

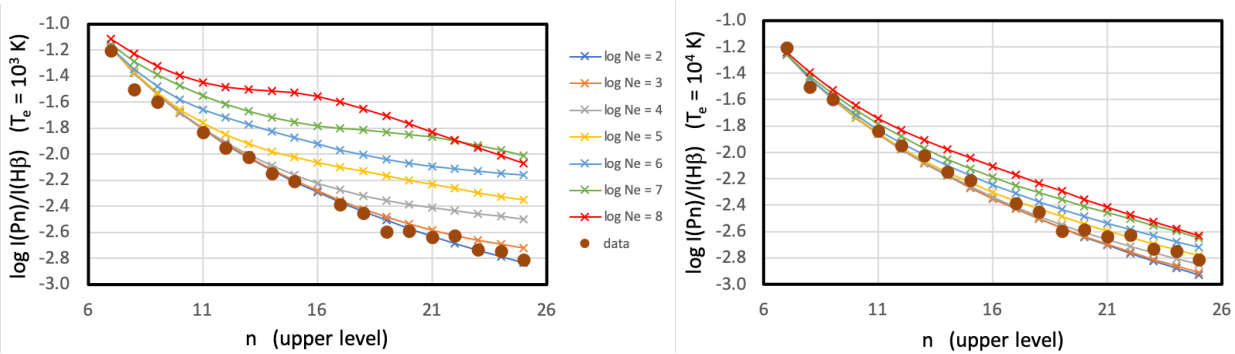


Figure 20. These panels present the intensities of reddening-corrected, high- n Paschen lines with respect to the intensity of $H\beta$ as a function of the upper level for assumed electron temperatures of 1,000 K (left) and 10,000 K (right). The implied densities are of $\sim 1,000 \text{ cm}^{-3}$ at 1,000 K and perhaps $\sim 10,000 \text{ cm}^{-3}$ at 10,000 K.

The error bars indicate the standard deviation of the distribution of the ratio values at each threshold level. The crosses indicate the median values at each threshold level while the dashed lines indicate the values of the 5-th and 95-th percentiles of the distribution, again at each threshold level. All statistics include only the $0.72'' - 9.00''$ spatial range to exclude the flat-fielding artefacts in the top few rows of PV diagrams (top row). The mean and median values do not vary strongly with the threshold level, indicating that the temperature variation within the plasma emitting these He I lines is modest. The different threshold levels correspond to different volumes of the plasma that emit these lines. At the 10% threshold, plasma throughout the main shell contributes to the statistics of the line ratios in Figure 21 while, at the 90% threshold, the statistics reflect only the plasma along the line of sight to the end of the main shell, farthest from the central star.

Given the limited variation in these line ratios (and temperatures) we adopt the mean value and its standard deviation for the threshold at 30% of the maximum intensity as our temperature indicator and its uncertainty (this sample includes over 500 pixels). The

range of values spanned by the standard deviation at this threshold usually includes almost the entire range of variation in the mean or median at all threshold values. In the bottom row of Figure 21, we compare the intensity ratio, now also corrected for reddening with the theoretical values (atomic data: Table 1). By this measure, the He I lines imply an electron temperature of $\log T_e$ of 3.85 – 4.05 (He I $\lambda\lambda 4713/4026$), 3.90 – 4.07 (He I $\lambda\lambda 4713/4471$), and 3.89 – 4.03 (He I $\lambda\lambda 4713/5876$) if electron densities range over $10^2 - 10^6 \text{ cm}^{-3}$.

In Figure 22, we present the He I $\lambda\lambda 4026/5876$ and He I $\lambda\lambda 4471/5876$ line ratios, which have some sensitivity to the electron density. The three rows present the same information as in Figure 21. Here, only the He I $\lambda\lambda 4026/5876$ ratio provides additional information, restricting the electron density to values of 10^4 cm^{-3} or lower. Considering this restriction, the previous electron temperatures are restricted to the temperature ranges of $\log T_e$ of 3.91–4.05 (He I $\lambda\lambda 4713/4026$), 3.97–4.07 (He I $\lambda\lambda 4713/4471$), and 3.93 – 4.03 (He I $\lambda\lambda 4713/5876$)

Finally, we can also use the N II and O II lines to compute the electron temperature and density. Figure 23 presents the PV diagrams for the N II $\lambda\lambda 4041, 5666$,

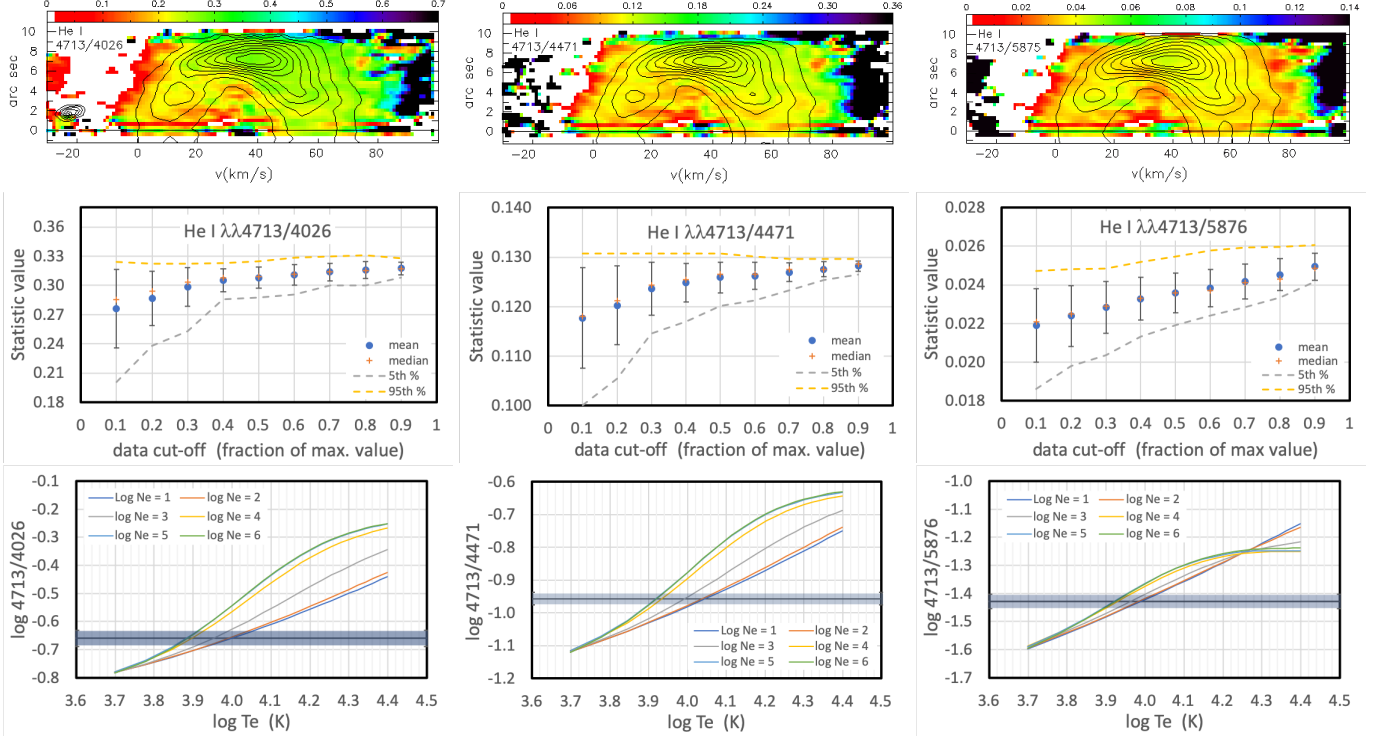


Figure 21. Top row: These panels present the PV diagrams of the line ratios He I $\lambda\lambda 4713/4026$ (left), He I $\lambda\lambda 4713/4471$ (middle), and He I $\lambda\lambda 4713/5876$ (right). The contours show the intensity of the He I $\lambda\lambda 4026$, 4471 , and 5876 lines (the denominator of the ratio). Middle row: These panels present various statistics for the ratios of the PV diagrams of He I $\lambda\lambda 4713/4026$ (left), He I $\lambda\lambda 4713/4471$ (middle), and He I $\lambda\lambda 4713/5876$ (right) as a function of the line intensities in the original PV diagrams of the He I $\lambda\lambda 4026$, 4471 , and 5876 lines (denominator). In the top and middle rows, the line ratios have been corrected for the flux scale factors (Table 5), but not for reddening. Bottom row: These panels compare the ratio of the line intensities of He I $\lambda\lambda 4713/4026$ (left), He I $\lambda\lambda 4713/4471$ (middle), and He I $\lambda\lambda 4713/5876$ (right), now corrected for reddening (Table 6), with the theoretical line intensities from Porter et al. (2013). We adopt the mean line ratio for all pixels exceeding 30% of the maximum line intensity of the denominator and the uncertainty given by the standard deviation. The He I lines are compatible with temperatures $\log T_e = 3.91 - 4.07$ when considering densities up to 10^4 cm^{-3} (see Figure 22).

5680 lines as well as the N II $\lambda\lambda 4041/5680$ (temperature) and N II $\lambda\lambda 5666/5680$ (density) line ratios. The PV diagram for N II $\lambda 4041$ is the one with the worst S/N and is from a different wavelength interval. Even so, the N II $\lambda\lambda 4041/5680$ ratio is decently uniform. Certainly, there is no clear evidence of gradients or large-scale changes. The N II $\lambda\lambda 5666/5680$ line ratio is very uniform, especially where the intensity of the lines is strong.

In Figure 24, we plot the N II $\lambda\lambda 4041/5680$ line ratio as a function of temperature (left panel) and the N II $\lambda\lambda 5666/5680$ line ratio as a function of density (right panel). For both line ratios, we use all of the pixels that exceed 40% of the maximum intensity in the PV diagram of the N II $\lambda 5680$ line. The shaded region indicates the mean value and the range allowed by 90% of the distribution (from the 5th to the 95th percentiles). The theoretical ratio (atomic data: Table 1), is shown for different values of the electron temperature (left panel) and density (right panel). The N II $\lambda\lambda 4041/5680$ line ratio implies an electron temperature of $\log T_e = 3.3 -$

4.2 dex. The N II $\lambda\lambda 5666/5680$ line ratio implies an electron density of $\log N_e > 3.5$ dex and is compatible with electron temperatures of $\log T_e = 2.7 - 4.2$ dex. Combining the restrictions from the two N II line ratios, they are nominally compatible with $\log T_e = 3.7 - 4.2$ dex and $\log N_e > 3.5$ dex (and up to 5.0 dex given the atomic data available).

Figure 25 presents the PV diagrams of the O II $\lambda\lambda 4089$, 4649 , 4662 lines (left column) and of the O II $\lambda\lambda 4089/4649$ (temperature) and O II $\lambda\lambda 4662/4649$ (density) line ratios (right column). The PV diagrams for all of the lines have good S/N. The temperature- (top right) and density-sensitive (middle right) line ratios are both quite uniform. Hence, there is no evidence for any large scale variations in the temperature or density of the plasma emitting in the O II lines.

Figure 26 compares the O II $\lambda\lambda 4089/4649$ and O II $\lambda\lambda 4662/4649$ line ratios (left and right panels, respectively) with the theoretical values for different physical conditions (atomic data: Table 1). The pink shaded re-

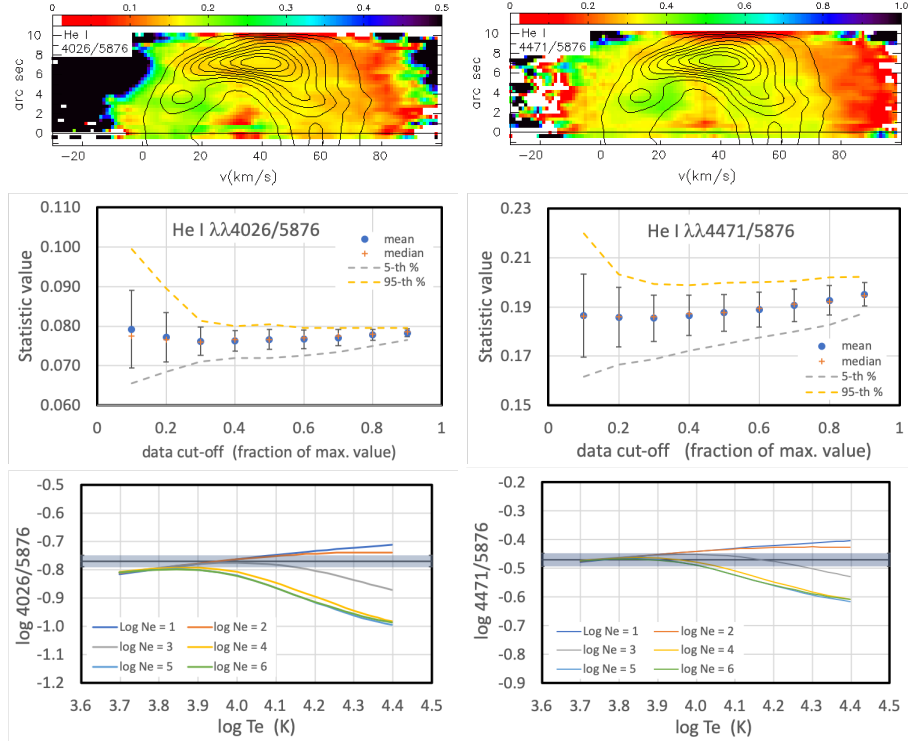


Figure 22. Top row: These panels present the PV diagrams of the line ratios He I $\lambda\lambda 4026/5876$ (left) and He I $\lambda\lambda 4471/5876$ (right). The contours show the intensity of the He I $\lambda 5876$ line (the denominator). Middle row: These panels present various statistics for the line ratios of He I $\lambda\lambda 4026/5876$ (left) and He I $\lambda\lambda 4471/5876$ (right) as a function of the line intensities in the original PV diagram of the He I $\lambda 5876$ line (denominator). These line ratios have been corrected for the flux scale factors (Table 5), but not reddening. Bottom row: These panels compare the ratio of the lines of He I $\lambda\lambda 4026/5876$ (left) and He I $\lambda\lambda 4471/5876$ (right), now corrected for reddening, with the theoretical line intensities from Porter et al. (2013). These line ratios are insensitive to temperature, but have some sensitivity to density and are useful to check the reddening (Table 6). These He I lines are compatible with densities up to 10^4 cm^{-3} .

gion indicates the observed value and the range containing 90% of the distribution of values using all of the pixels that exceed 40% of the maximum intensity in the O II $\lambda 4649$ PV diagram (denominator). The temperature-sensitive O II $\lambda\lambda 4089/4649$ line ratio (Figure 26; left panel) implies $\log T_e = 3.2 - 4.2$ dex, considering all densities. The density-sensitive O II $\lambda\lambda 4662/4649$ line ratio (Figure 26; right panel) implies $\log N_e > 3.7$ dex and an electron temperature of $\log T_e = 2.8 - 4.4$ dex. Combining the two O II line ratios implies $\log T_e = 3.2 - 3.7$ dex and $\log N_e > 3.7$ dex (and up to 5.0 dex).

For both the N II and O II lines, the density-sensitive indicator is compatible with temperatures substantially lower than the temperature-sensitive line ratio. The density-sensitive line ratios are sufficiently close in wavelength that they are independent of the reddening correction and the scale factors between wavelength intervals, but one (O II) or both (N II) corrections are important for the temperature-sensitive ratios. The density-sensitive line ratios also have higher S/N. If the density-sensitive line ratios are considered alone, they

are in excellent agreement, implying that the electron temperature may be as low as $\log T_e = 2.7 - 2.8$ dex (~ 500 K). All things considered, we conclude that the N II and O II lines imply a “low” electron temperature of $\log T_e \sim 3.2 - 3.7$ dex and a “high” electron density of $\log N_e > 3.7$ dex (and up to 5.0 dex given the atomic data available). If so, the N II and O II lines imply different physical conditions compared to the H I, He I, and forbidden lines. Again, this argues for the presence of two plasma components.

3.3. Contamination in forbidden lines

Many emission lines may be excited by multiple processes. Here, we consider the effects of excitation mechanisms other than collisional excitation on the [N II] $\lambda 5755$, [O II] $\lambda\lambda 7319, 7320$, and [O III] $\lambda 4363$ lines. We shall call these additional excitation channels “contamination”, though Nature does not see it that way. The contamination is severe in the first two cases (Liu et al. 2000), but it has a minimal effect on [O III] $\lambda 4363$ in NGC 6153. We choose these examples deliberately be-

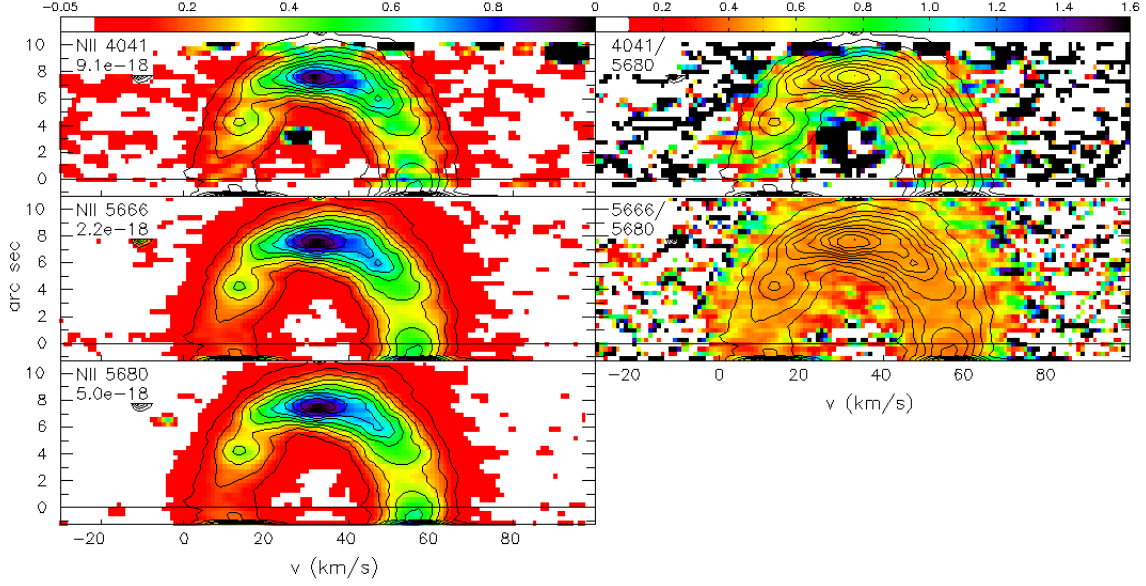


Figure 23. These panels present the PV diagrams for the lines (left) of N II $\lambda 4041$, N II $\lambda 5666$, and N II $\lambda 5680$, and for the line ratios (right) N II $\lambda\lambda 4041/5680$ and N II $\lambda\lambda 5666/5680$. The contour lines are of the N II $\lambda 5680$ intensity. The spatial coverage of the PV diagram of N II $\lambda 4041$ is less than for the others. Both the temperature- and density-sensitive maps (4041/5680 and 5666/5680, respectively) are reasonably uniform.

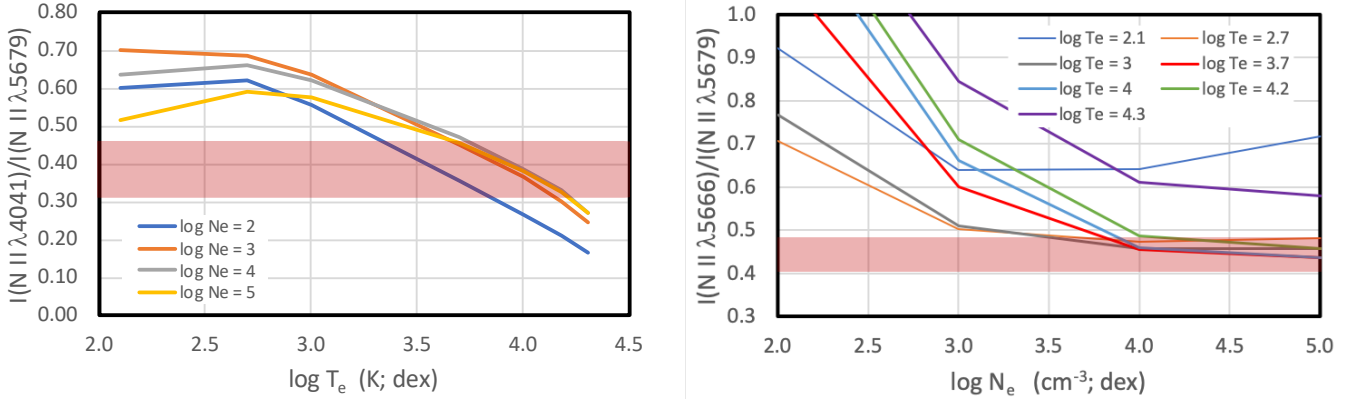


Figure 24. Left: We present the temperature-sensitive N II $\lambda\lambda 4041/5680$ ratio and its uncertainty (the pink region), based upon an intensity limit at 40% of the maximum intensity and the 90% width of the distribution of pixel values. This ratio is corrected for both reddening and the scale factor between the CD2 and CD3b wavelength intervals. $T_e > 2,000$ K if the electron density is very low; $T_e > 5,000$ K for higher densities. Right: We present the density-sensitive N II $\lambda\lambda 5666/5680$ ratio and its uncertainty (the pink region; same definitions). The N II $\lambda\lambda 5666/5680$ ratio is compatible with high densities ($3,000 - 10^5 \text{ cm}^{-3}$) and a wide range of electron temperatures ($500 - 16,000$ K).

cause they are little affected by collisional de-excitation

§3.1 and §3.2 indicate that there are two sets of physical conditions that apply to two kinematical components. One set of physical conditions applies to the H I, He I, and forbidden lines (the normal nebular plasma), where the electron temperature is $\sim 8,000$ K and the electron density is $\sim 4,000 - 5,000 \text{ cm}^{-3}$. For the normal nebular plasma, we adopt the physical conditions of $T_e = 8,000$ K and $N_e = 5,000 \text{ cm}^{-3}$. The second set of

physical conditions applies to the N II and O II lines (the additional plasma component), where the temperature is lower, $T_e \sim 1,600 - 5,000$ K, and the density higher, $N_e > 5,000 \text{ cm}^{-3}$, possibly as high as 10^5 cm^{-3} . For the additional plasma component, we adopt the physical conditions of $T_e = 2,000$ K and $N_e = 10,000 \text{ cm}^{-3}$. Thus, we shall decompose the PV diagrams for the [N II] $\lambda 5755$, [O II] $\lambda\lambda 7319, 7320$, and [O III] $\lambda 4363$ lines, assuming that there are two plasma components in NGC 6153, each with distinct physical conditions.

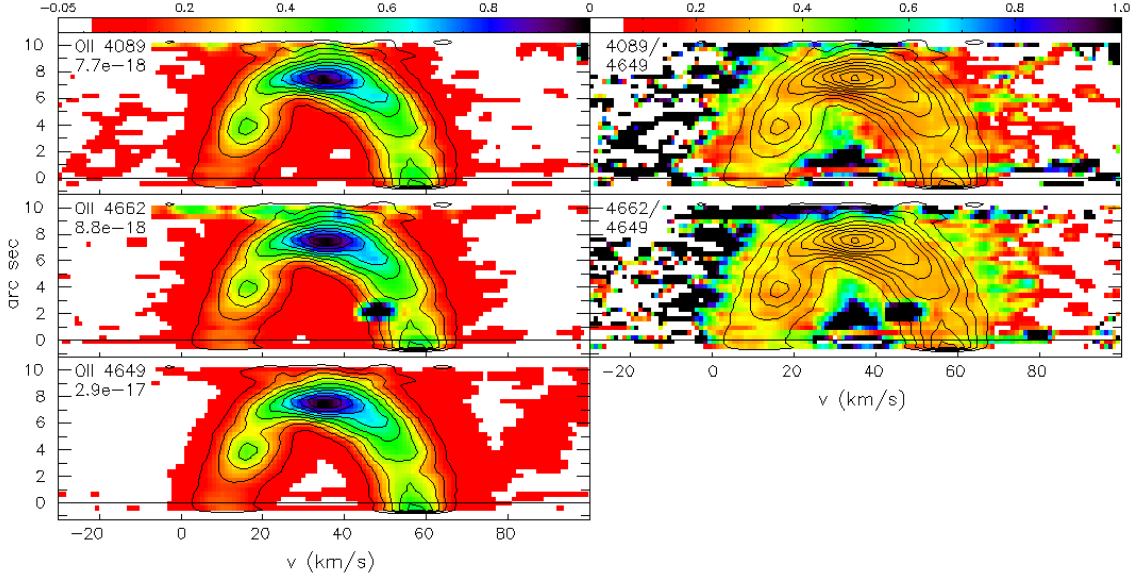


Figure 25. In the left column, these panels present the lines of O II $\lambda 4089$, O II $\lambda 4662$, and O II $\lambda 4649$. In the right column, the panels present the PV diagrams of the line ratios O II $\lambda\lambda 4089/4649$ and O II $\lambda\lambda 4662/4649$. The contours in the right panels are the intensity contours from the PV diagram of the O II $\lambda 4649$ line (bottom left). The bright fringe at the top of the PV diagrams is due to imperfect subtraction of the nebular continuum. A cosmic ray contaminates the PV diagram of the O II $\lambda 4662$ line.

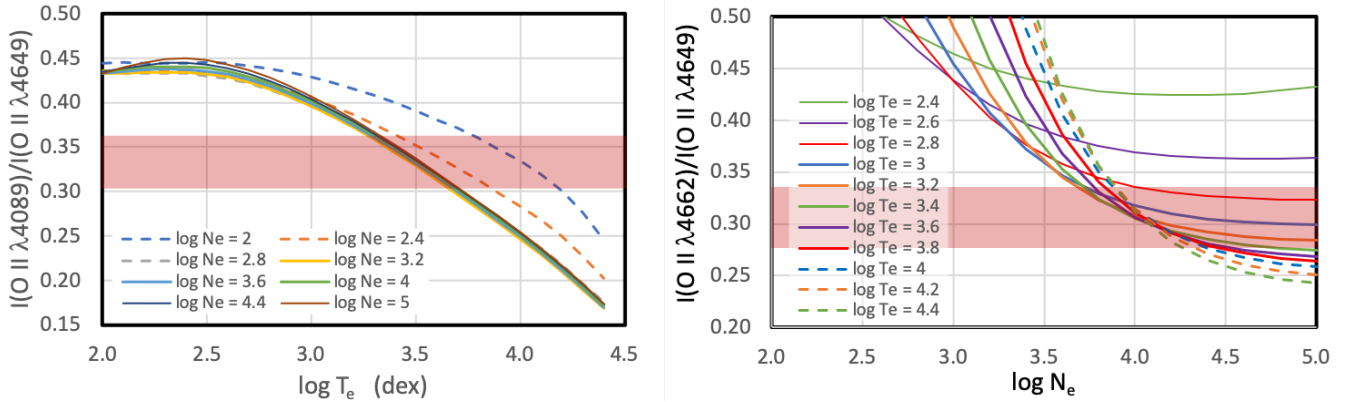


Figure 26. Left: We present the temperature-sensitive O II $\lambda\lambda 4089/4649$ ratio and its uncertainty as a function of the temperature (the pink band), based upon an intensity limit at 40% of the maximum intensity and the 90% width of its distribution of pixel values. The temperature implied is rather low, $\log T_e = 3.25 - 3.7$ dex, unless the density is very low. Right: We present the observed value of the density-sensitive ratio O II $\lambda\lambda 4662/4649$ and its uncertainty as a function of the electron density (the pink band; same definitions). The observed O II $\lambda\lambda 4662/4649$ ratio implies high densities ($10^4 - 10^5 \text{ cm}^{-3}$) at lowest temperatures ($< 2,500 \text{ K}$) and densities of $5,000 - 30,000 \text{ cm}^{-3}$ at higher temperatures.

The goal of the decomposition is to obtain PV diagrams of the forbidden lines with *only* the contribution due to collisional excitation, the only excitation process considered by the standard nebular analysis. Thus, we need models or patterns of the emission due to recombination from the normal nebular plasma and the additional plasma component that we may subtract from the observed PV diagrams, leaving only the contribution due to collisional excitation. To do this, we must scale

the patterns of the PV emission using the emissivities of the lines involved for the physical conditions found in each of the plasma components. The three panels of Figure 27 present the emissivities of the relevant lines due to H^+ , N^+ , O^+ , and O^{2+} as a function of the electron temperature (atomic data: Table 1).

First, we consider [N II] $\lambda 5755$. Figure 28 compares the PV diagrams of the forbidden [N II] $\lambda\lambda 5755, 6583$ lines. The bright filament is the brightest feature in both

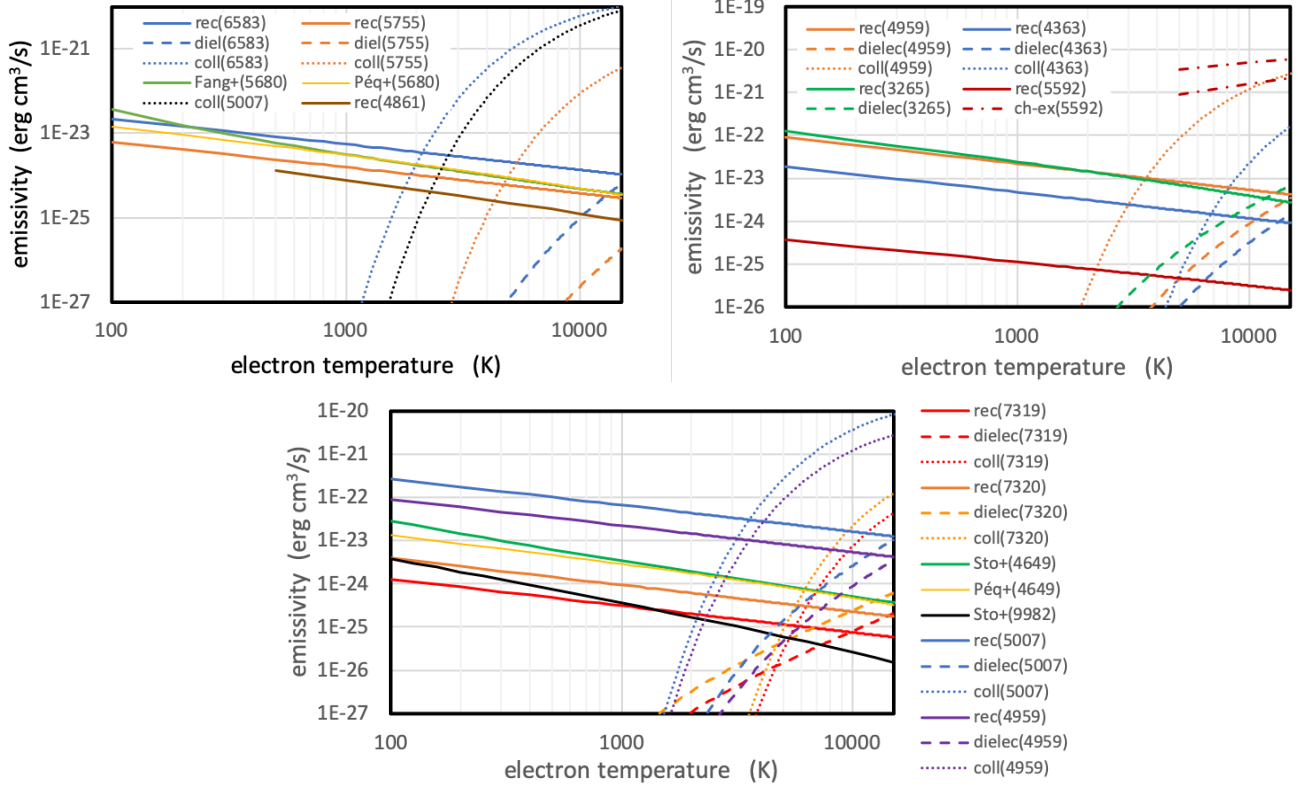


Figure 27. We present the emissivities per ion and per electron for the lines required to decompose the PV diagram of [N II] $\lambda 5755$ (top left), [O III] $\lambda 4363$ (top right), and [O II] $\lambda\lambda 7319, 7320$ (bottom). The emissivity for charge exchange is per ion and per hydrogen atom. The legends indicate the transition wavelength in brackets. The line style indicates the physical process that excites the line: solid for radiative recombination, dashed for dielectronic recombination, dotted for collisional excitation, and dot-dashed for charge exchange. Atomic data: See Table 1.

PV diagrams, but the contrast between it and the main shell is very different for the two lines, with the main shell being relatively much brighter in the [N II] $\lambda 5755$ line. The velocity splitting of [N II] $\lambda 6583$ is greater than in the [N II] $\lambda 5755$ line, 52.7 km/s versus 46.2 km/s. Finally, there is an excellent correspondence between the emission from the main shell in the [N II] $\lambda 5755$ line and the emission from the permitted N II $\lambda 5680$ line (contours). All of these lines are from the CD3 wavelength intervals. The bottom panel in Figure 28 presents the [N II] $\lambda\lambda 5755/6583$ ratio and it is clear that the excess emission in the [N II] $\lambda 5755$ line correlates with the emission from the N II $\lambda 5680$ line (contours).

Hence, in NGC 6153, the [N II] $\lambda 5755$ line appears to be contaminated due to an additional excitation mechanism whose PV distribution is similar to that of the N II $\lambda 5680$ line. The N II $\lambda 5680$ line may be excited directly via recombination, but also indirectly by fluorescence in the He I $\lambda 509$ lines in the He⁺ zone or by starlight in the N⁺ zone (Grandi 1976; Escalante 2002; Sharpee et al. 2004). Were N II $\lambda 5680$ excited primarily by fluorescence, its PV diagram should be very similar to that

of [N II] $\lambda 6584$ (Figure 4; N⁺ zone) or He I $\lambda 4471$ (Figure 47; He⁺ zone), as occurs for He II $\lambda\lambda 3203, 4686$ and the Bowen fluorescence lines of O III $\lambda 3444$ and N III $\lambda 4634$ (Figure 45). So, in NGC 6153, fluorescence is unlikely to be the main excitation mechanism for the N II $\lambda 5680$ line. The contamination pattern like N II $\lambda 5680$ in the [N II] $\lambda 5755$ line would thus appear to be due to recombination.

Since the upper level of the [N II] $\lambda 5755$ line is a singlet state, fluorescence from the ground state (triplet) cannot excite it. Although the excitation of singlet states via recombination is disfavored relative to the triplet states, it is possible (Rubin 1986; Liu et al. 2000). The appearance of contamination with a PV pattern similar to that of a recombination line in [N II] $\lambda 5755$ is therefore not unreasonable. If so, in the model of two plasma components previously outlined, both components will contribute to the observed PV diagrams of both [N II] $\lambda\lambda 5755, 6583$ via recombination while the normal nebular plasma will contribute the collisional excitation, i.e., there are three contributions to the [N II] $\lambda\lambda 5755, 6583$ lines.

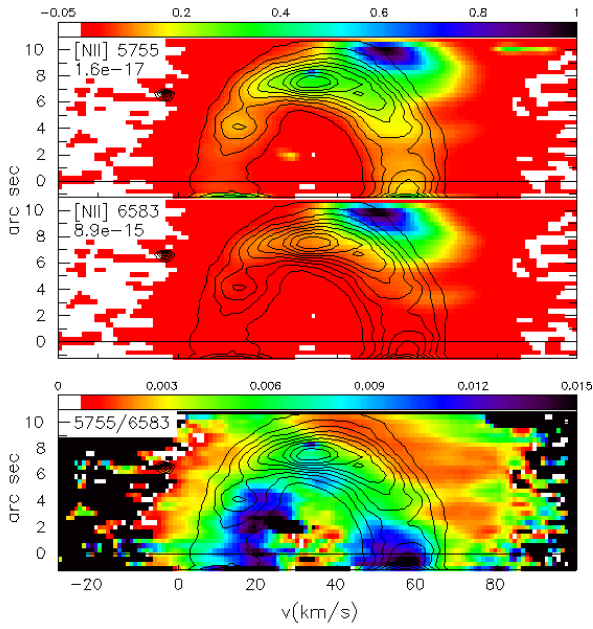


Figure 28. We compare the PV diagrams of the forbidden [N II] $\lambda\lambda 5755, 6583$ lines (top and middle, respectively) and of their ratio. The contour lines are of the emission in the N II $\lambda 5680$ line (Figure 29/Figure 6). The main shell is notably brighter, compared to the filament on its receding side, in the [N II] $\lambda 5755$ line, as is the emission from the permitted N II $\lambda 5680$ line. The ratio of the forbidden lines presents an excellent correspondence between the excess emission in the [N II] $\lambda 5755$ line and the emission from N II $\lambda 5680$.

The key to decomposing the PV diagrams of [N II] $\lambda\lambda 5755, 6583$ is to decompose the observed PV diagram of N II $\lambda 5680$ in terms of the recombination from each of the plasma components. The parent ion that gives rise to the N II lines is N^{2+} , which occupies a volume in the nebula very similar to O^{2+} (e.g., Figure 9 from Richer et al. 2013). Since [N II] $\lambda 5755$ is from the CD3b wavelength interval, we use the PV diagram of [O III] $\lambda 5007$ as a template for the PV pattern of the emissivity of the recombination contribution from the normal nebular plasma. We estimate the N II $\lambda 5680$ emission due to the normal nebular plasma by scaling the PV diagram of [O III] $\lambda 5007$ by the abundance ratio (we adopt $N^{2+}/O^{2+} = 0.5$; Liu et al. 2000; McNabb et al. 2016), and then by the ratio of the emissivities of the two lines at 8,000 K (Figure 27; adopting the atomic data for $N_e = 10,000 \text{ cm}^{-3}$ for N II $\lambda 5680$). We subtract this model of the recombination contribution from the normal nebular plasma from the observed PV diagram of N II $\lambda 5680$ to obtain the PV diagram of the N II $\lambda 5680$ emission from the additional plasma component. Mathematically, if, $I(\lambda)_x$ indicates the PV diagram of the emission line at wavelength λ due to recombination as observed ($x = o$), from the normal nebular plasma

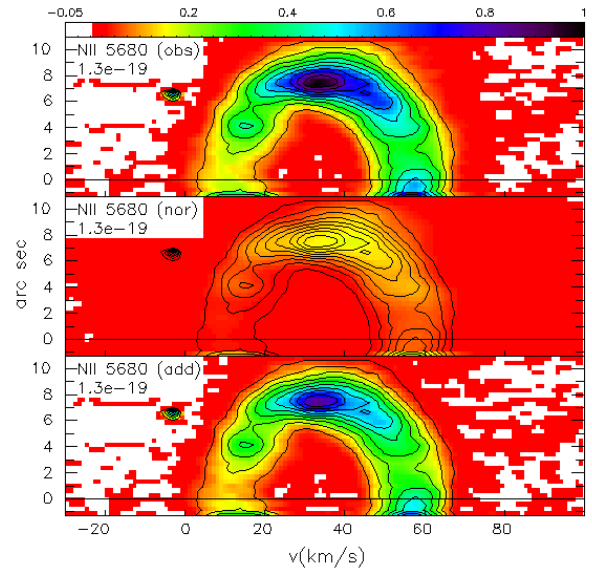


Figure 29. These panels present the PV diagrams of the N II $\lambda 5680$ line as observed (top), the model of the recombination in this line from the normal nebular plasma (middle), and the difference between the previous two (bottom), which is interpreted as the recombination in this line due to the additional plasma component. The contours in the three panels correspond to the contours for the N II $\lambda 5680$ line (top panel). The three panels share the same intensity scale.

($x = n$), or from the additional plasma component ($x = a$), the foregoing implies that the PV diagram of the N II $\lambda 5680$ due to the additional plasma component is

$$I(5680)_a = I(5680)_o - I(5680)_n,$$

where

$$I(5680)_n = \frac{N(N^{2+})}{N(O^{2+})} \frac{\epsilon(5680)_n}{\epsilon(5007)_n} I(5007)_o$$

with $N(X)$ being the abundance of ion X and $\epsilon(\lambda)_x$ the emissivity of line λ at the temperatures previously indicated for each plasma component (subscript).

Figure 29 demonstrates the decomposition of the PV diagram of the N II $\lambda 5680$ line. Clearly, the contribution from the normal nebular plasma is a small fraction of the total observed emission. However, its PV emission pattern differs from that of the additional plasma component.

We use the two PV patterns of the recombination emission in the bottom two panels of Figure 29 to subtract these contributions from the PV diagrams of the [N II] $\lambda\lambda 5755, 6583$ lines. The scale factors are the ratios of the emissivities of the [N II] $\lambda\lambda 5755, 6583$ lines with respect to that of the N II $\lambda 5680$ line at the temperatures of the two plasma components. For the [N II]

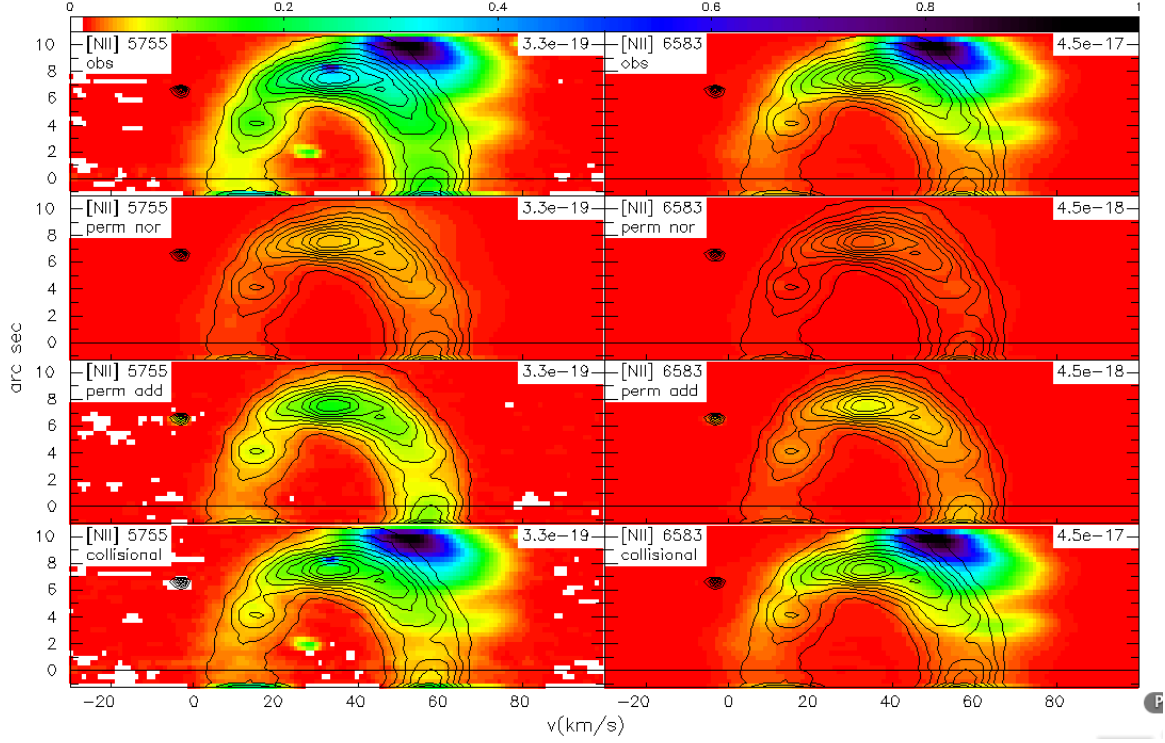


Figure 30. The left and right columns present the PV diagrams of [N II] $\lambda 5755$ and [N II] $\lambda 6583$, respectively. In the top row, we present the observed PV diagrams of these lines. In the second and third rows, we present the models of the permitted emission in these lines due to recombination in the normal nebular plasma and the additional plasma component, respectively. In the bottom row, we present the difference between the observed PV diagram and the sum of the permitted emission, yielding what should be the emission due to collisional excitation only from the normal nebular plasma. The maximum of the intensity/color scale is given at upper right in each panel (constant on the left; variable on the right). The contour lines are of the intensity of the N II $\lambda 5680$ line (Figure 29/Figure 6). Clearly, the fractional contribution of recombination from both plasma components, but especially the additional plasma component, is much greater for [N II] $\lambda 5755$.

$\lambda 5755$ line,

$$I(5755)_a = \frac{\epsilon(5755)_a}{\epsilon(5680)_a} I(5680)_a$$

$$I(5755)_n = \frac{\epsilon(5755)_n}{\epsilon(5680)_n} I(5680)_n$$

$$I(5755)_c = I(5755)_o - I(5755)_a - I(5680)_n$$

where $I(5755)_c$ indicates the PV diagram of [N II] $\lambda 5755$ due to collisional excitation only. (The process for [N II] $\lambda 6583$ is equivalent.) Figure 30 presents the result. While the contamination due to recombination is completely negligible for [N II] $\lambda 6583$, this is not the case for [N II] $\lambda 5755$, since the additional plasma component makes a very significant contribution to its PV diagram. Even the normal nebular plasma contributes noticeable emission due to recombination. The morphologies of the PV diagrams for the [N II] $\lambda\lambda 5755, 6583$ lines in the bottom row are now much more similar.

Figure 31 presents the PV diagrams of the [N II] temperature before and after correcting for the recombination contributions to the [N II] $\lambda\lambda 5755, 6583$ lines.

Clearly, the result after removing the recombination contributions is much more like the [O III] and [Ar III] temperature maps (Figures 14-15). Even so, the [N II] temperature still exceeds the [O III] and [Ar III] temperatures in the innermost regions. The bottom panel in Figure 31 is an experiment to estimate the maximum contribution of recombination to the [N II] $\lambda\lambda 5755, 6583$ lines in which the recombination contributions are arbitrarily increased by 20% with respect to the values based upon the existing atomic data. The resulting PV diagram of the [N II] temperature is nearly as uniform as the maps of the [O III] and [Ar III] temperatures.

Therefore, decontaminating the [N II] lines using the nominal atomic data yields an electron temperature much more similar to those found using the [O III] or [Ar III] lines. Though it might be argued that the nominal correction may underestimate the contamination due to recombination, the basic lesson is that using the raw PV diagrams (or line intensities) of the [N II] lines leads to erroneous results in NGC 6153.

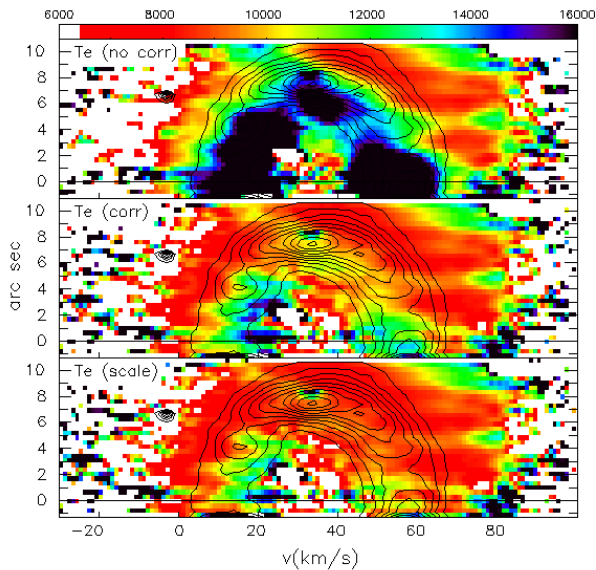


Figure 31. These PV diagrams present the [N II] temperature. Top panel: We use the observed PV diagrams of the [N II] $\lambda\lambda 5755, 6583$ lines. Middle panel: We decompose the [N II] lines using the atomic data as published (Figure 30). Bottom panel: We scale the recombination coefficients (atomic data: Table 1) by a factor of 1.2 when decomposing the [N II] lines. In all panels, the temperature scale spans the range 6,000 – 16,000 K and the contours are of the intensity of the N II $\lambda 5680$ line (Figure 29). After correcting for the recombination contribution to the [N II] lines (middle), the [N II] temperature is a much better approximation of the [O III] and [Ar III] temperatures, but may still be too high in the innermost regions. The [N II] temperature map in the bottom panel is nearly as uniform as the [O III] (Figures 14/36) and [Ar III] temperatures (Figure 15).

The previous procedure differs from that employed by others (e.g., Liu et al. 2000; Corradi et al. 2015; Ruiz-Escobedo & Peña 2022; García-Rojas et al. 2022). Those analyses suppose that the additional plasma component emits all of the permitted emission whereas we find that the additional plasma component contributes 76% of the total N II $\lambda 5680$ emission (and 84% of the total O II $\lambda 4649$ emission), which is not a great difference. Our method may be applied when two-dimensional data are available, whether in PV or spatial coordinates.

Turning now to [O II], Figure 32 compares the PV diagrams of [O II] $\lambda 3726$, [O II] $\lambda\lambda 7319, 7320$, and O II $\lambda\lambda 4649, 9982$. The morphologies of the PV diagrams of the [O II] lines are very different (considering only one line of the [O II] $\lambda 7319, 7320$ doublet). For [O II] $\lambda 3726$, the filament on the receding side of the main shell is by far the brightest feature, but, in the auroral lines, the brightest feature is the brightest part of the main shell! The contour lines superposed on both panels are those of the O II lines with the same spatial coverage and they

are an excellent approximation to the emissivity of the main shell in [O II] $\lambda 7320$. This suggests that, like [N II] $\lambda 5755$, the [O II] $\lambda\lambda 7319, 7320$ lines suffer very significant contamination due to recombination.

We model the [O II] $\lambda\lambda 7319, 7320$ lines since their critical densities for collisional de-excitation are well above the densities found for the normal nebular plasma in NGC 6153. (This is not the case for [O II] $\lambda\lambda 3726, 3729$.) We begin by decomposing the O II $\lambda\lambda 4649, 9982$ lines to obtain the recombination contributions from the two plasma components, as we did for [N II] $\lambda 5680$. We use the [O III] $\lambda\lambda 4959, 5007$ lines to model the recombination contribution from the normal nebular plasma (emissivities in Figure 27). We use [O III] $\lambda 5007$ to match the spatial extent of the O II $\lambda 9982$ line, though it was not obtained simultaneously with the other lines and may suffer from a slightly different slit placement. As for N II $\lambda 5680$, the additional plasma component contributes the majority of the emission due to recombination. We construct models of the recombination contribution to each of the [O II] $\lambda\lambda 7319, 7320$ lines based upon each of the O II $\lambda\lambda 4649, 9982$ lines. We subtract the sum of the models from the observed PV diagram of the [O II] $\lambda\lambda 7319, 7320$ lines to obtain the PV diagram of the emission due to collisional excitation only.

Figure 33 presents the result of this decomposition for the [O II] $\lambda\lambda 7319, 7320$ lines. The observed PV diagram is in the top row (both columns). The middle row presents the model of the permitted emission, based upon the O II $\lambda 4649$ (left) and O II $\lambda 9982$ lines (right). The two models differ, with that based upon O II $\lambda 9982$ having approximately two thirds of the flux of the model based upon O II $\lambda 4649$. The models also differ because the shapes of the O II $\lambda 4649$ and O II $\lambda 9982$ PV diagrams differ slightly, with the latter being somewhat “taller”, likely due to the longer slit used in the red arm of the spectrograph. The taller O II $\lambda 9982$ line profile is a better match to the shape of the [O II] $\lambda 7319, 7320$ PV diagram.

The bottom row in Figure 33 presents the difference between the observed emission and the modeled permitted emission, again using the models based upon the O II $\lambda 4649$ and O II $\lambda 9982$ lines. The PV diagrams in the bottom row in Figure 33 should include only the emission due to collisional excitation. Evidently, collisional excitation dominates the [O II] $\lambda\lambda 7319, 7320$ emission from the filament, but recombination provides the overwhelming majority of the [O II] $\lambda\lambda 7319, 7320$ emission from the main shell itself, as expected given the comparison of the PV diagrams for [O II] $\lambda 3726$ and [O II] $\lambda\lambda 7319, 7320$ in Figure 32. The PV diagram of the [O II] $\lambda\lambda 7319, 7320$ at bottom left is very similar to

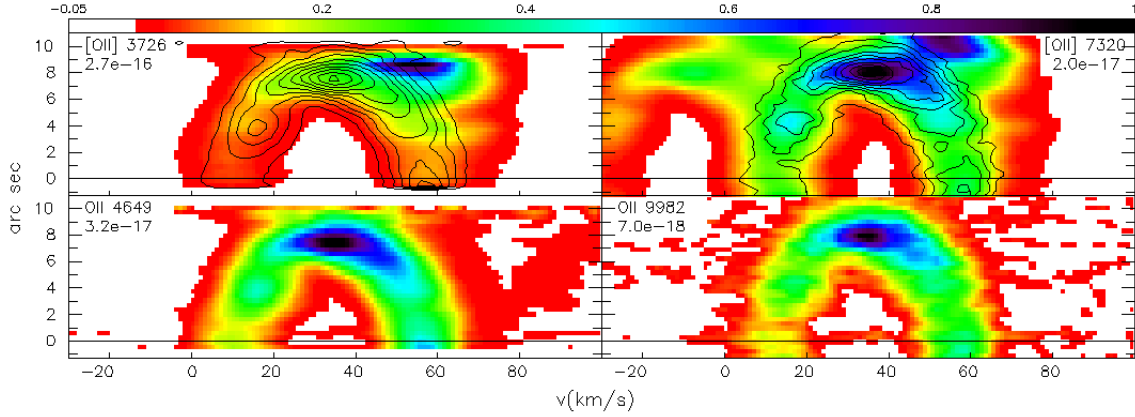


Figure 32. These PV diagrams present the [O II] $\lambda 3726$ and [O II] $\lambda\lambda 7319,7320$ lines (top row) and the O II $\lambda 4649$ and O II $\lambda 9982$ lines (bottom row). The contours on the PV diagrams in the top row are of the intensity of the PV diagrams in the bottom row. The morphology of the PV diagrams for the [O II] lines are very different. For the [O II] $\lambda 7320$ line, the main shell is the brightest feature and its emission matches very closely that from O II $\lambda 9982$. Also, the velocity splitting for [O II] $\lambda 3726$ is greater than that for O II $\lambda 4649$ whereas the velocity splitting for [O II] $\lambda 7320$ is the same as for O II $\lambda 9982$.

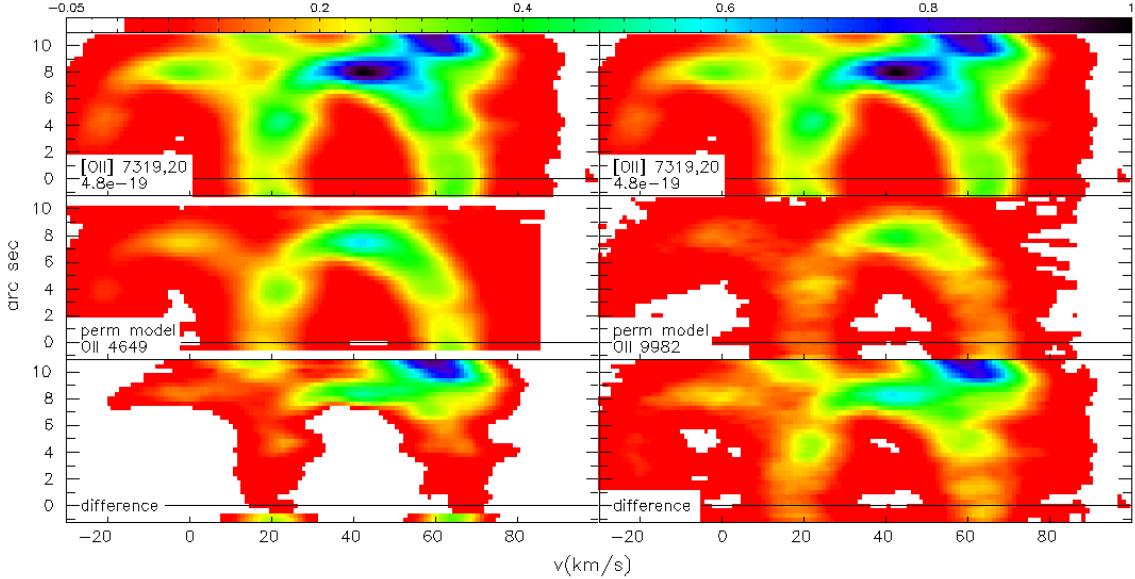


Figure 33. These panels present the decomposition of the [O II] $\lambda\lambda 7319,7320$ line profiles (top row, both columns). The middle row presents the total permitted emission in both lines using O II $\lambda 4649$ (left) and O II $\lambda 9982$ (right) as models. The bottom row is the difference between the observations (top) the models (middle). All panels share a common intensity scale. The model based upon the O II $\lambda 4649$ line accounts for *almost all* of the emission from the main shell in the [O II] $\lambda\lambda 7319,7320$ lines.

the PV diagrams of the [N II] $\lambda 6583$, [S II] $\lambda 6716$ or [Cl II] $\lambda\lambda 8578,9123$ lines (Figure 49).

On the other hand, the PV diagram of the [O II] $\lambda\lambda 7319,7320$ lines after subtracting the model based upon O II $\lambda 9982$ (Figure 33, bottom right) still has significantly more emission from the main shell than those of the [N II] $\lambda 6583$, [S II] $\lambda 6716$ or [Cl II] $\lambda\lambda 8578,9123$ lines (Figure 49). (The emission in the filament is unaffected.) In order to obtain a PV diagram for [O II]

$\lambda\lambda 7319,7320$ similar to those using the model of the permitted emission based upon O II $\lambda 9982$, the emissivity for this line from Storey et al. (2017) should be multiplied by a factor of about 1.5. Storey et al. (2017) note the limitations of their calculations for the $2s^2 2p^2$ (3P) $4f$ and $5f$ configurations. Since the upper level of the O II $\lambda 9982$ transition, (3P_2) $5g[6]_{13/2,11/2}$ (Wenaker 1990), is even higher in energy, within 2.2 eV of the ionization

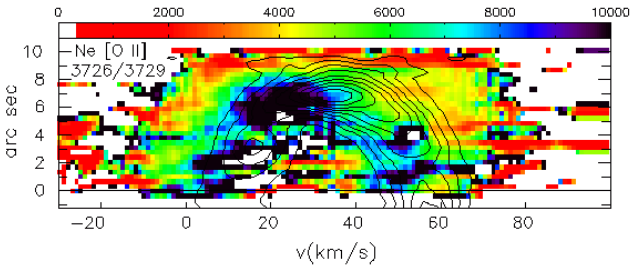


Figure 34. We present the PV diagram of the density derived from the [O II] $\lambda\lambda 3726, 3729$ lines. The contours are those of the intensity of the emission in the O II $\lambda 4649$ line (see Figure 6). Overall, the density implied by the [O II] lines is higher than implied by the [S II], [Cl III], or [Ar IV] lines. In addition, there is a similar structure of high densities where the [N II] $\lambda\lambda 5755/6583$ ratio is high (Figure 28).

limit ($O^{2+} \ ^3P_2$), a discrepancy of $\sim 50\%$ in its emissivity is perhaps not unexpected.

We suppose that the decontamination of the [O II] $\lambda\lambda 7319, 7320$ lines using the model based upon O II $\lambda 4649$ (Figure 33) is the more reliable result. However, the most important lesson is that recombination contributes the majority of the emission in the [O II] $\lambda\lambda 7319, 7320$ lines for the main shell of NGC 6153 regardless of which model we use. Hence, were the [O II] $\lambda\lambda 7319, 7320$ emission to be analyzed as if due to collisional excitation, the result would be erroneous for the main shell (but not the filament). Although Figure 33 concerns the [O II] $\lambda\lambda 7319, 7320$ lines, recombination undoubtedly contributes to the emission in the [O II] $\lambda\lambda 3726, 3729$ lines as well. All of the recombination contribution to the [O II] $\lambda\lambda 7319, 7320, 7330, 7331$ lines will contribute to the excitation of the [O II] $\lambda\lambda 3726, 3729$ lines as will direct recombination to the upper levels of the [O II] $\lambda\lambda 3726, 3729$ lines, as has been argued elsewhere (e.g., Liu et al. 2000; Wesson et al. 2018).

Even though the [O II] $\lambda\lambda 3726, 3729$ lines are contaminated by recombination excitation, they remain a useful density indicator. However, the [O II] $\lambda\lambda 3726/3729$ ratio will sense the density in the two plasma components. Given the low critical densities for the [O II] $\lambda\lambda 3726, 3729$ lines, $\sim 1,000$ and $4,000 \text{ cm}^{-3}$ at $9,000 \text{ K}$, respectively (atomic data: Table 1), the [O II] $\lambda\lambda 3726, 3729$ lines will suffer more collisional de-excitation in the additional nebular plasma. Where a given plasma component dominates the emission in these lines in the PV diagram, the [O II] $\lambda\lambda 3726/3729$ ratio will reflect the density in that plasma component. Necessarily, there will be PV coordinates where the two plasma components will contribute and the density will not represent either component. Figure 34 presents the density computed from the ratio of these lines, assum-

ing an electron temperature of $10,000 \text{ K}$. Its structure is more complicated than the PV diagrams for the densities computed from the [S II], [Cl III], [Ar IV], N II, and O II lines. However, it is possible to recognize that, at PV coordinates corresponding to the outer part of the main shell, the density is near $5,000 \text{ cm}^{-3}$, as for the other forbidden lines, and, for the inner part of the main shell, the densities reach $10,000 \text{ cm}^{-3}$, compatible with the results from the N II and O II lines.

Finally, we consider the PV diagrams of [O III] $\lambda\lambda 4363, 4959$. These emission lines are the result of three physical processes. The dominant process is collisional excitation, but recombination and charge exchange also contribute. So, we must model and subtract the latter two contributions from the observed PV diagrams to yield PV diagrams for the [O III] $\lambda\lambda 4363, 4959$ lines due to collisional excitation only. We attribute the contributions from both recombination and charge exchange to the normal nebular plasma, since we assume that the additional plasma component does not emit in O III lines (§3.1, Appendix A).

We model the charge exchange contribution using the O III $\lambda 5592$ line. The upper level of the O III $\lambda 5592$ line will be dominantly excited by charge exchange, though recombination also contributes a minority ($< 10\%$; atomic data: Table 1). The lower level of the O III $\lambda 5592$ line decays to the upper levels of the [O III] $\lambda 4363$ or [O III] $\lambda\lambda 4959, 5007$ lines (for a useful Grotrian diagram, see Dalgarno & Sternberg 1989). The upper level may also decay directly to the upper levels of the [O III] $\lambda 4363$ or [O III] $\lambda\lambda 4959, 5007$ lines and it may also decay indirectly to these levels via other intermediate levels.

Since we use the observed PV diagram for O III $\lambda 5592$, the scaling to account for the contribution of charge exchange to [O III] $\lambda 4363$ requires only the branching ratio from the upper and lower levels of the O III $\lambda 5592$ line (the Einstein A-values) for populating the upper level of the [O III] $\lambda\lambda 4363, 4959$ lines, i.e., the physical conditions are not involved (atomic data: Table 1). We find that the excitation to the upper levels of both lines is at most 48% of the intensity of the O III $\lambda 5592$ line.

We use the PV diagram of the O III $\lambda\lambda 3260, 3265$ lines as the emission pattern for the recombination contribution to the [O III] $\lambda\lambda 4959, 5007$ lines (atomic data: Table 1), as all of the bright O III lines are enhanced by Bowen fluorescence (often dominated by it) and so cannot be used. However, the O III $\lambda\lambda 3260, 3265$ lines are just to the blue of our flux calibration limit at 3300 \AA . Since the He II $\lambda 3203$ line over-estimates the $\text{He}^{2+}/\text{H}^+$ ionic abundance (Table 7), the O III $\lambda\lambda 3260, 3265$ lines

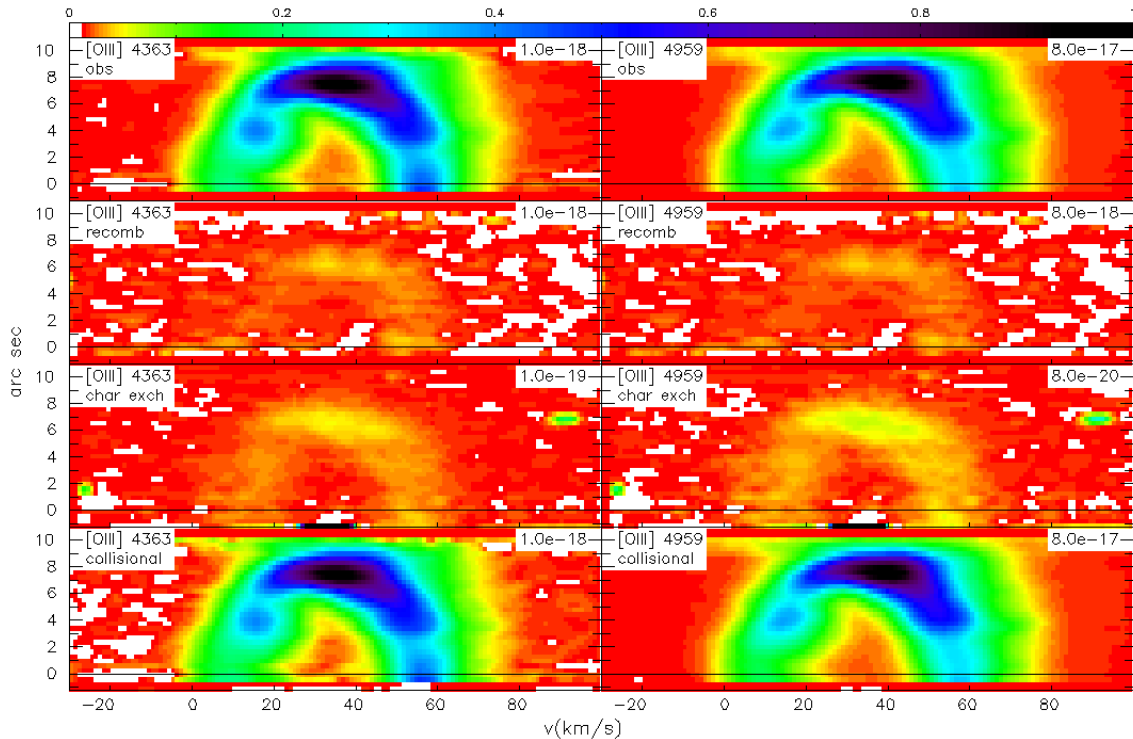


Figure 35. These panels present PV diagrams for [O III] λ 4363 (left) and [O III] λ 4959 (right) of the observed emission (top), the contamination due to recombination (second), the contamination due to charge exchange (third), and the emission due to collisional excitation (bottom). The PV diagrams in the bottom row are the result of subtracting those in the second and third rows from the PV diagrams in the top row. Since the emission due to recombination and charge exchange is so faint, the normalization value for the intensity/color scale varies by factors of 10 – 1,000 with respect to the top and bottom rows. While recombination makes a small contribution to the [O III] λ 4363,4959 PV diagrams, charge exchange is much less relevant.

may over-estimate the recombination contribution to the [O III] lines.

Figure 35 presents the results for [O III] λ 4363,4959. Clearly, the contamination due to recombination and charge exchange is minor. Only for [O III] λ 4363 is contamination noticeable, and only in the case of recombination. Although the effect of this contamination upon the total emission from [O III] λ 4363 is minor, it affects the “inside” of the line profile where the flux is lower.

Figure 36 presents the [O III] electron temperature before and after correcting for the contamination due to recombination and charge exchange. Figure 36 also presents the change in temperature and, as expected, it is largest on the “inside” of the line profile, near the systemic velocity and at spatial positions near the central star. Even so, the change is small, amounting to a decrease in the electron temperature of up to 200 K. The final panel in Figure 36 presents the change in temperature over the area covered by the contours at 10%, 20%, ..., 90% of the maximum intensity of the [O III] λ 4363 line. The biggest change occurs for the areas enclosed by the lower limiting fluxes. These areas also show the

widest range of change. This occurs because these areas of the PV diagram correspond to larger nebular volumes within which there is a greater range of electron temperature, including both the hotter interior of the main shell and the lower temperatures in the diffuse emission at the most redshifted velocities.

In NGC 6153, the effect of recombination and charge exchange upon the electron temperature deduced from the [O III] λ 4363,4959 lines is small to negligible. In particular, the central volume of the nebula (near the systemic velocity and near the central star) appears to be hotter than the rest. This is very likely due to the extra heating as a result of the presence of He^{2+} ions. Since the appearance of He^{2+} is accompanied by the disappearance of O^{2+} , the most important source of nebular cooling, there is good reason to accept that the electron temperature really does increase in the central volume of the nebula.

4. DISCUSSION: T_E AND CONSEQUENCES

Table 9. Summary of main results

Parameter	Details	Indicator	Result	
(1)	(2)	(3)	(4)	
$E(B - V)$	§2.3	H I and He I lines	0.535 ± 0.053 mag	
temperature	§3.2.1	kinematics	~ 8000 K	
	§3.3	[N II] $\lambda\lambda 5755/6583$	$\sim 9,000$ K; contaminated by recombination	
	§3.2.2	[O III] $\lambda\lambda 4363/4959$	$\sim 9,000$ K, higher in inner main shell	
	§3.2.2	[S III] $\lambda\lambda 6312/9069$	unusable due to telluric absorption	
	§3.2.2	[Ar III] $\lambda\lambda 5191/7751$	$\sim 9,000$ K, higher in inner main shell	
	§3.2.3	He I lines	$8,000 - 12,000$ K, rather uniform	
	§3.2.3	O II $\lambda\lambda 4089/4649$	$1,800 - 5,000$ K, little variation	
	§3.2.3	N II $\lambda\lambda 4041/5680$	$> 2,500$ K	
	density	§4.1	Peimbert (1967) t^2	$T_0 \sim 8000$ K and $t^2 \sim 0.03$ in large volume
		§3.3	[O II] $\lambda\lambda 3726/3729$	$\sim 5,000 - 10,000$ cm $^{-3}$; contaminated by recombination
§3.2.2		[S II] $\lambda\lambda 6716/6731$	$\sim 2,000$ cm 3 at edges, $5,000 - 6,000$ cm $^{-3}$ closest to centre	
§3.2.2		[Cl III] $\lambda\lambda 5517/5537$	$5,000 - 6,000$ cm $^{-3}$, rather uniform	
§3.2.2		[Ar IV] $\lambda\lambda 4711/4740$	$3,000 - 4,000$ cm $^{-3}$	
§3.2.3		high Balmer lines	$< 10,000$ cm $^{-3}$	
§3.2.3		He I lines	$< 10,000$ cm $^{-3}$	
§3.2.3		O II $\lambda\lambda 4662/4649$	$> 5,000$ cm $^{-3}$, rather uniform	
§3.2.3		N II $\lambda\lambda 5666/5680$	$> 10,000$ cm $^{-3}$, rather uniform	
ADF(O $^{2+}$)		§4.3	ORL/CEL	ADF(O $^{2+}$) up to 12 in main shell, ~ 1.2 in diffuse emission
N $^{++}$ mass fraction	§4.4	additional component	$23 - 53\%$ @ $10,000$ cm $^{-3}$; $3 - 10\%$ @ $100,000$ cm $^{-3}$	
O $^{++}$ mass fraction	§4.4	additional component	$30 - 62\%$ @ $10,000$ cm $^{-3}$; $4 - 13\%$ @ $100,000$ cm $^{-3}$	
H $^+$ mass fraction	§4.5	additional component	$3 - 5\%$	

mgro.astroph

Although it is not a direct result, our most notable finding is that the plasma in NGC 6153 is complex. Whether we consider the kinematics or the physical conditions in the nebular shell, we find complexity. Usually, there are complementary and congruent lines of evidence for this complexity. For instance, both the kinematics and the physical conditions imply the existence of two plasma components. In spite of the complexity, we also find very strong support for the conventional astrophysics of nebular plasmas. The physical conditions implied by the H I, He I, and forbidden lines are generally congruent, as are the kinematics found for the H I, He I, and [O III] $\lambda 4959$ lines. The kinematics of the great majority of the emission lines, both permitted and forbidden, conform to the canonical results of Wilson (1950).

Table 9 collects the physical conditions computed in the previous section for easier comparison. This table also includes results from the subsections that follow.

As will become clear, the theme of complexity becomes more and more apparent.

4.1. Variations in the electron temperatures

The two panels in Figure 37 quantify the variation of the [O III] and [Ar III] temperatures (Figures 14 and 15, respectively). The left panel presents the mean and median [O III] temperature computed based upon different limiting intensities of the [O III] $\lambda\lambda 4363, 4959$ lines. To compute these values, only the temperatures from the pixels whose intensities exceed the indicated intensity relative to the maximum intensity are used. For instance, for a relative intensity limit of 0.1, only the non-zero temperature values from the pixels whose line intensities exceed 10% of the maximum intensity for the indicated line are used ([O III] $\lambda\lambda 4363, 4959$ in the left panel). The mean and median values of the temperatures are similar, indicating that the temperature distributions are approximately symmetric. For a given line, either [O III] $\lambda 4363$ or [O III] $\lambda 4959$, the variation of the mean and median temperatures as a function of the limiting line intensity is modest. The right panel in

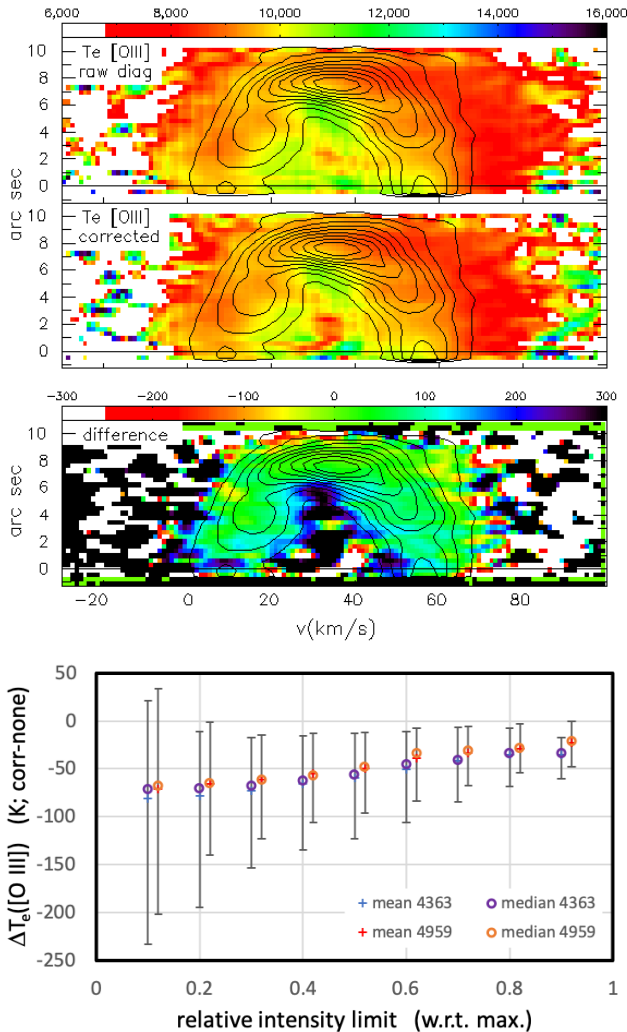


Figure 36. The top two panels present the [O III] electron temperature using the raw PV diagrams and those corrected for contamination due to recombination and charge exchange. The third panel presents the PV diagram of the difference map between the corrected and raw temperature maps. In all panels, the contours are of the [O III] $\lambda 4363$ intensity. At bottom, we plot the mean and median for the difference map as a function of the relative intensity in the [O III] $\lambda 4363$ line. The error bars span from the 5-th to 95-th percentiles.

Figure 37 presents the same information for the [Ar III] $\lambda\lambda 5191, 7135$ lines. (The analogous figure for the temperature based upon the [Ar III] $\lambda\lambda 5191, 7751$ lines is very similar.)

The mean or median temperatures at different limiting line intensities measure the temperature over very different volumes of the nebula. At the 10% limiting intensity, plasma throughout the entire volume that emits the [O III]/[Ar III] lines is included, but, at the 90% limiting intensity, only part of the plasma seen along the line of sight towards the edge of the nebula’s main shell

is included. Thus, the wider distribution of temperature values at lower limiting intensities is not due primarily to signal-to-noise, but to the wider range of physical conditions that occur in the larger volumes included by the lower limiting intensity limits.

In both panels of Figure 37, there is a systematic variation in the difference between the mean/median temperature weighted by the auroral and nebular lines, increasing as the limiting intensity increases. The mean/median values based upon the intensity of the auroral lines ([O III] $\lambda 4363$, [Ar III] $\lambda 5191$) are systematically higher than those based upon the intensity of the nebular lines ([O III] $\lambda 4959$, [Ar III] $\lambda 7135$). Since the excitation energy for the auroral lines is more than double that for the nebular lines, it makes sense that the temperatures weighted by the auroral lines are the larger ones since they are excited more easily where the temperature is higher and so will be biased to regions of higher temperature.

Comparing the two panels in Figure 37, there is a systematic difference between the [O III] and [Ar III] temperatures, with the latter being systematically lower. While the volumes occupied by the O^{2+} and Ar^{2+} ions largely coincide, the Ar^{2+} volume is biased towards the outer part of the O^{2+} volume, so it may be cooler. However, exciting the [Ar III] lines requires less energy, so they will also be more easily excited where the temperature is cooler. Figure 38 plots the mean [O III] and [Ar III] temperatures weighted using the [Ar III] $\lambda 7135$ line, i.e., *averaging over the same volume of the nebula*. Again, the [O III] temperature is systematically higher than the [Ar III] temperature. This would appear to be a clear example of the temperature sensitivity of the excitation of forbidden lines affecting the temperature derived from them (Peimbert 1967). An alternative explanation is that, for some reason, one or both of the [Ar III] or [O III] temperatures are systematically wrong.

Both of the [O III] and [Ar III] temperatures (Figures 14 and 15) are greater than the $\sim 8,000$ K temperature that matches the thermal line widths of the H I, He I, and [O III] $\lambda 4959$ lines (Table 9). The lower end of the range allowed by the He I lines also matches the kinematic temperature, though temperatures derived from recombination lines should actually under-estimate the true mean temperature (Peimbert 1967).

The difference between the temperatures found when weighting with the auroral and nebular lines in Figure 37 or the difference between the [O III] or [Ar III] temperatures in Figure 38 nicely illustrates the central concern discussed by Peimbert (1967): The temperature sensitivity of the emission mechanism influences the temperature obtained if temperature fluctuations are present.

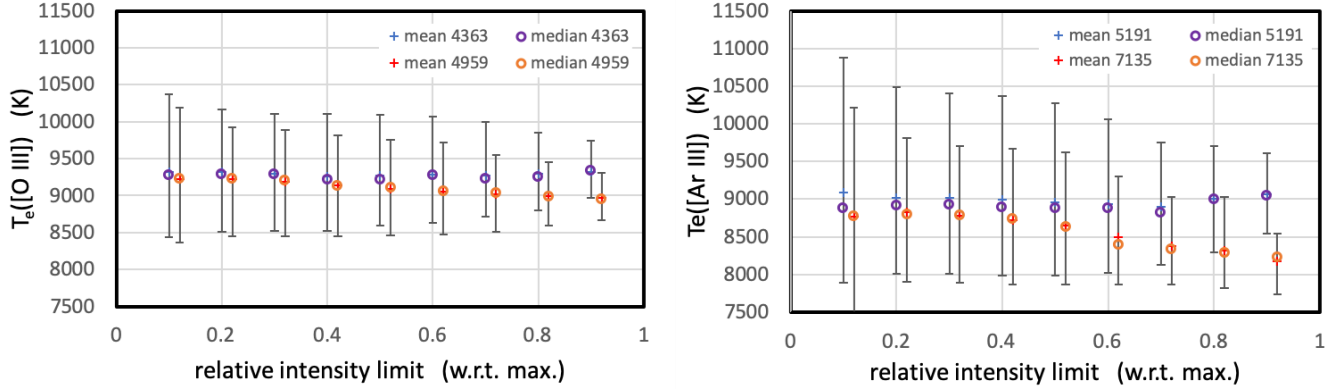


Figure 37. The left panel presents mean and median values of the [O III] temperature as a function of the limiting intensities of [O III] $\lambda 4363$ or [O III] $\lambda 4959$ with respect to the maximum value for each line. The error bars represent the extent of the distributions from the 5th to 95th percentiles. The right panels presents the same information for the [Ar III] temperatures as a function of the line intensity limit for the [Ar III] $\lambda\lambda 5191, 7135$ lines. In both cases, there is a systematic difference depending upon whether they are weighted by the intensity of the nebular or auroral line, with the values weighted using the auroral line being systematically higher.

In the temperature fluctuation formalism of Peimbert (1967), normally a pair of temperatures is used, one sensitive to cooler regions and the other sensitive to hotter ones, but, in principle, any pair with a different temperature sensitivity should work. So, we use the [O III] and [Ar III] temperatures. These temperatures are related to T_0 and t^2 , the mean square temperature fluctuations (atomic data: Table 1), by

$$T_e([\text{O III}]) \approx T_0 \left(1 + \left(\frac{91183}{T_0} - 3 \right) t^2 \right)$$

$$T_e([\text{Ar III}]) \approx T_0 \left(1 + \left(\frac{676981}{T_0} - 3 \right) t^2 \right).$$

Ideally, we would study the temperature fluctuations on a pixel-by-pixel basis in the PV diagram, but the PV diagram of the [Ar III] temperature has insufficient S/N for this, so instead we consider the same limiting intensities of the [Ar III] $\lambda 7135$ line as in Figures 37 and 38. We weight both temperatures using this line intensity so as to compare exactly the same volume of the nebula.

In Figure 38, we present the values of true mean temperature and the t^2 value at each flux limit of the [Ar III] $\lambda 7135$ line. Evidently, the true mean temperature is substantially lower than the [Ar III] or [O III] temperatures, by 1,000–2,000 K. For the low flux limits, whose volume is similar to that sensed by the kinematic temperature, T_0 is similar to the kinematic temperature. For the high flux limits, corresponding to the small volume towards the rim of the main shell, the temperature is lower. (The kinematic temperature is not sensitive to small volumes because of the thermal line width of the H I lines.) The large decrease in T_0 for the smallest volumes is mostly driven by the similar, but smaller, change in the [Ar III]

temperature. Given the difference in the true mean temperature for small and large volumes, we would not be surprised if deeper data found large scale variations in T_0 , as we find for the [Ar III] and [O III] temperatures.

In Figure 38, like T_0 , the t^2 value varies substantially, but in the opposite direction. Given the definition of t^2 (Peimbert 1967), the relative amplitude of the temperature fluctuations varies from 15% in the largest volumes to 22% in the smallest. These are large temperature fluctuations. The absolute value of these fluctuations mirrors the variation in t^2 , spanning 1250–1550 K. Hence, in NGC 6153, we find substantial temperature fluctuations using only forbidden line temperatures. Since the forbidden lines arise in the normal nebular plasma, these temperature fluctuations pertain to that plasma component alone.

Figure 38 illustrates the risk of using two forbidden lines to determine t^2 and T_0 . The value of t^2 is driven primarily by the difference between the [O III] and [Ar III] temperatures, increasing as the difference increases. Meanwhile, the value of T_0 is driven by the value of the lower of the two temperatures, also increasing as the lower temperature increases. Provided the [Ar III] temperature is lower than the [O III] temperature, a solution can always be found. T_0 can easily differ very substantially from the forbidden line temperatures, so it is important that they be well-constrained. In the usual scenario, a temperature based upon permitted emission is included, usually the ratio of an H I line to the Balmer jump, which is lower than the true mean temperature, T_0 , as shown in Figure 38.

The above supposes that the difference in the [Ar III] and [O III] temperatures is due to temperature fluctuations. An alternative explanation is that one or both of

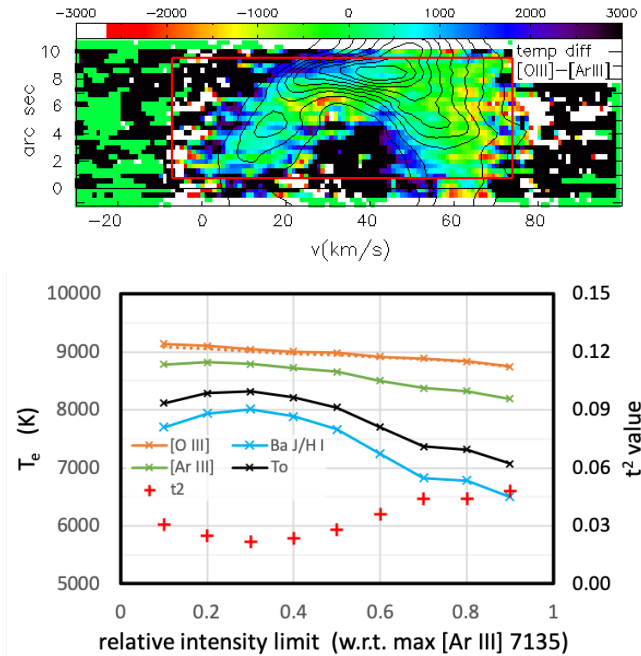


Figure 38. The top panel presents the PV diagram of the difference between the [O III] and [Ar III] temperatures. The contours are of the intensity of [Ar III] λ 7135. The rectangle indicates the columns and rows considered for the statistics. In the bottom panel, we plot the mean [O III] and [Ar III] temperatures as a function of the limiting relative intensity of the [Ar III] λ 7135 line, i.e., both temperatures are averaged over the same PV coordinates. (The dotted line shows the effect of correcting for the contamination in the [O III] λ 4363 line.) As in Figure 37, the [O III] temperature is systematically higher. We also plot the T_0 and t^2 parameters for the temperature fluctuation formalism of Peimbert (1967) for the same limiting relative intensities of the [Ar III] λ 7135 line, as well as the predicted temperature for the Balmer jump following Peimbert (2019). When large volumes are considered, T_0 is similar to the kinematic temperature (§3.2.1).

these temperatures could be systematically in error. Our [O III] temperatures are similar, though up to ~ 200 K higher than, those of Kingsburgh & Barlow (1994, ; 8940 K) and Liu et al. (2000, ; 9030 K and 9070 K, adopting the same atomic data; Table 1 in both cases), so our [O III] temperature appears reasonable and secure considering that our observations do not coincide spatially with theirs.

As for the [Ar III] temperature, based upon the atomic data we use (Table 1), we find values of 10,125 K and 9,900 K for the minor axis and whole nebula spectra from Liu et al. (2000), $\sim 1,000$ K higher than we find, so the agreement is not good, but perhaps not unreasonable. McNabb et al. (2016) report an [Ar III] temperature of 9,350 K, similar to our result, but we are unable to convert this to the same atomic data that we

use since we derive a much higher temperature based upon the line intensities in their Table 2. Objectively, we have no strong cross-check on the flux calibration for the blue end of the CD4b wavelength interval (§2.3), so it is possible that the flux calibration for the [Ar III] $\lambda\lambda$ 7135,7751 lines is incorrect. If these line intensities were lower by 20% or more, the [O III] and [Ar III] temperatures would be very similar and they could not be used to derive the amplitude of temperature fluctuations in Figure 38. However, even such an error would not eliminate the evidence for temperature fluctuations from the [O III] and [Ar III] temperature maps (Figure 37).

Considering the independent evidence for temperature fluctuations from the [O III] and [Ar III] temperature maps and the lower kinematic temperature (§3.2.1), we do not doubt the presence of temperature fluctuations in the normal nebular plasma in NGC 6153.

For the diffuse emission beyond the receding side of the main shell, the [O III] temperature falls to values near 8,000 K (Figure 14). This temperature agrees with the kinematic temperature, which appears to apply to the PV coordinates of this emission since Figures 9, 10, and 11 are all relatively uniform at the PV coordinates of this emission. As we show below (§4.3), the ADF for this volume of the normal nebular plasma is near 1.0. So, the temperature fluctuations in this part of the normal nebular plasma are apparently small. Unfortunately, we cannot check this directly since we do not detect the [Ar III] λ 5191 line in this part of the PV diagram. Therefore, the amplitude of the temperature fluctuations in the normal nebular plasma appears to vary, from very small in the diffuse emission beyond the receding side of the main shell to very substantial within the main shell itself.

In summary, not only does the normal nebular plasma in NGC 6153 contain large scale temperature gradients (Figures 14 and 15), but it also contains small scale temperature fluctuations, all based only upon forbidden lines (Figures 37 and 38). The amplitudes of both the large- and the small-scale effects are similar. Hence, even after decomposing the permitted O II emission as in §3.3, were we to use the O II emission from the normal nebular plasma to compute the O^{2+} abundance, it would not coincide with that computed from the [O III] lines and the [O III] temperature because of temperature fluctuations. Our use of the kinematic temperature for the normal nebular plasma in previous sections anticipates this result.

4.2. The Balmer jump temperature

Liu et al. (2000) find a Balmer jump temperature that is spatially uniform across NGC 6153's minor axis with values scattering about a mean value of 6,080 K. From a spatially-integrated spectrum, Zhang et al. (2004) report a value of $6,000 \pm 400$ K. McNabb et al. (2016) find a Balmer jump temperature of 6250^{+150}_{-100} K. Nominally, these temperatures do not agree with those we find here by other means based upon the kinematics or the He I and forbidden lines.

However, all of these Balmer jump temperatures were computed supposing a single plasma component. If we assume, as we illustrate below (§4.5), that approximately 5% of the mass of H^+ is at a temperature of 2,000 K and the rest at 8,000 K, using the definition of Liu et al. (2000), we find a ratio of Balmer jump to H11 of 0.161 \AA^{-1} using the atomic data of Storey & Hummer (1995) and Ercolano & Storey (2006), which implies an electron temperature of 6,000 K when we assume a single plasma component. Therefore, interpreted in the framework of two plasma components, the existing measurements of the Balmer jump temperatures are indeed compatible with the temperatures found here for both plasma components.

The complication in the foregoing is that the spatial extent of the two plasma components in NGC 6153 is not the same. The additional plasma component is more centrally concentrated (Liu et al. 2000; Tsamis et al. 2008, here, e.g., Figure 12). In principle, given the difference in the spatial distributions of the plasma components, Liu et al. (2000) should have found a lower Balmer jump temperature in the central part of NGC 1653, where the additional plasma component is found and where it contributes to increase the Balmer jump (w.r.t. the normal nebular plasma). Their Figure 14 shows no clear difference between the interior and exterior of the nebula, but it could be a S/N issue.

García-Rojas et al. (2022) find similar results for the Paschen jump temperature in NGC 6881, Hf 2-2, and M 1-42.

4.3. The PV variation of the ADF

We may use the decomposition of the O II $\lambda 4649$ line (§3.3) to construct the PV diagram of the ADF for O^{2+} . We compute the O^{2+} ionic abundance using the O II $\lambda 4649/H\beta$ and the [O III] $\lambda 4959/H\beta$ ratios using the emissivities from Figure 27. We adopt our usual choices for the physical conditions in the two plasma components, $T_e = 8,000$ K and $N_e = 5,000 \text{ cm}^{-3}$ for the normal nebular plasma and $T_e = 2,000$ K and $N_e = 10,000 \text{ cm}^{-3}$ for the additional plasma component. Before computing either line ratio, we must broaden the PV diagrams of the oxygen lines to the width of the

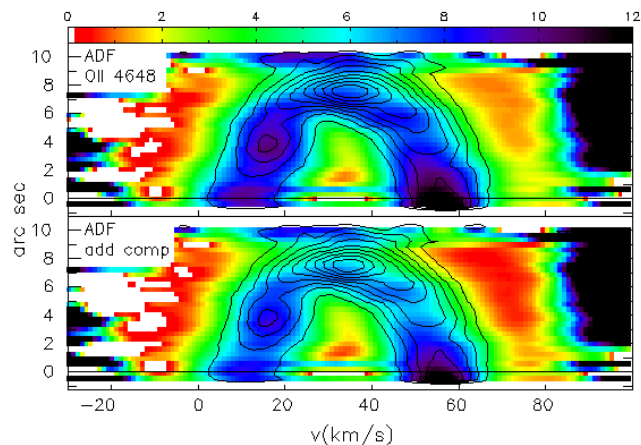


Figure 39. These PV diagrams present the variation of the ADF for O^{2+} as a function of position and velocity within our slit. The top panel presents the ADF computed using all of the permitted O II $\lambda 4649$ emission while the bottom panel uses only the emission due to the additional plasma component. The scale is common to the two panels, but the contours are not. At top, the contours are of the intensity of the observed O II $\lambda 4649$ intensity. At bottom, they are of the intensity of this line due to the additional plasma component only. In the top panel, the ADF for the diffuse emission beyond the receding side of the nebula is near 1.0, implying that this emission is due to the normal nebular plasma, i.e., there is no abundance discrepancy when considering this volume of the normal nebular plasma. In both panels, the apparently high values at the largest velocities are due to the C III $\lambda 4650$ line in the PV diagram of O II $\lambda 4649$.

hydrogen lines at the adopted temperatures, which is different for the O II $\lambda 4649$ and [O III] $\lambda 4959$ lines. Otherwise, we would introduce spurious structure in the PV diagram of the ADF.

Figure 39 presents the resulting PV diagram of the ADF. We compute the ADF in two ways. First, following common practice, we compute the O II $\lambda 4649/H\beta$ ratio using the observed PV diagram for O II $\lambda 4649$, broadened to match the thermal width expected for the $H\beta$ line. This is shown in the top panel of Figure 39. The ADF for O^{2+} is highest where the O II $\lambda 4649$ emission is most intense. Given the kinematics of the O II $\lambda 4649$ line, we expect the ADF to be highest at velocities closest to the systemic velocities and positions close to the central star, as observed.

The other important result from Figure 39 is that the ADF in the diffuse emission beyond the receding side of the main shell has a value near 1 (the actual value is $\sim 1.1 - 1.2$). An ADF near unity is congruent with the results that the temperatures determined using the [O III] lines, the kinematics, and the t^2 formalism are similar there (§3.2.1, §3.2.2, §4.1), so we expect that the diffuse emission beyond the main shell is due to the

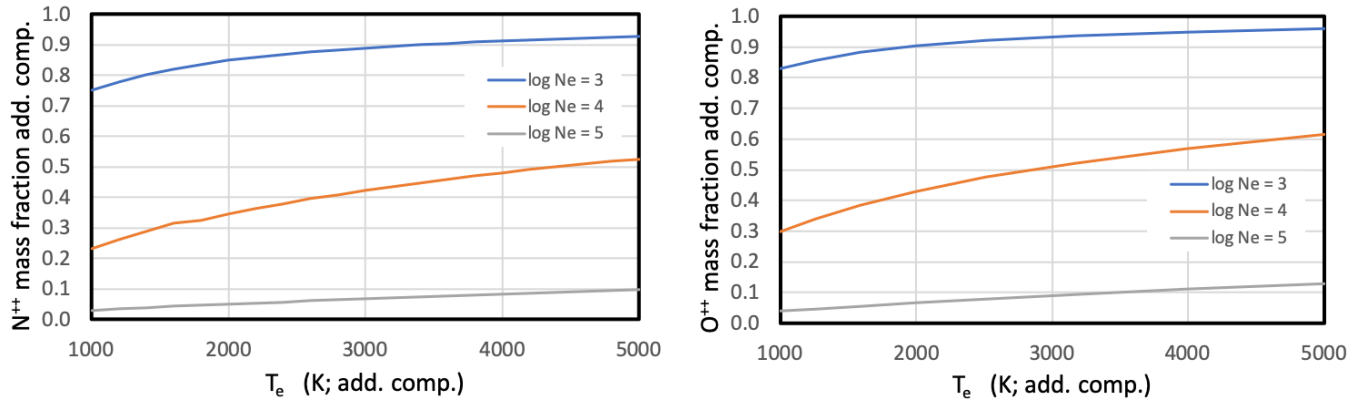


Figure 40. These panels present the mass fraction of N^{2+} (left) and O^{2+} (right) contributed by the additional plasma component for different densities and temperatures. The temperature range is that indicated by the N II $\lambda\lambda 4041/5680$ and O II $\lambda\lambda 4089/4649$ line ratios (§3.2.3). The N II $\lambda\lambda 5666/5680$ and O II $\lambda\lambda 4662/4649$ line ratios imply electron densities $> 5,000 - 100,000 \text{ cm}^{-3}$. If so, the additional plasma component accounts for up to about half of the N^{2+} and O^{2+} mass fractions.

normal nebular plasma alone and that temperature fluctuations are small in that volume of plasma.

Second, we compute the O II $\lambda 4649/H\beta$ ratio using only the O II $\lambda 4649$ emission from the additional plasma component. The bottom panel of Figure 39 presents this result. When two plasma components are present, this method is the more reasonable, since it discounts the permitted emission due to the normal nebular plasma. Given that the additional plasma component emits most of the O II $\lambda 4649$ emission (§4.4), the general pattern is similar to the top panel. The main difference is that the ADF for the diffuse emission beyond the receding side of the main shell is now near zero since the additional plasma component does not emit at those velocities. Regardless of the details, the basic result is that the ADF for O^{2+} is highest in the inner part of the main shell, where the additional plasma component has most of its mass in O^{2+} (§4.4).

4.4. The relative masses of N^{2+} and O^{2+} in the two plasma components

We may use the decompositions of the N II $\lambda 5680$ and O II $\lambda 4649$ lines into components due to the normal nebular plasma and the additional plasma component to estimate the relative masses of these two plasma components. We adopt our usual physical conditions (§3.3): $T_e = 8,000 \text{ K}$ and $N_e = 5,000 \text{ cm}^{-3}$ for the normal nebular plasma and $T_e = 2,000 \text{ K}$ and $N_e = 10,000 \text{ cm}^{-3}$ for the additional plasma component (emissivities: Figure 27). The mass of ion X in the additional plasma component with respect to that in the normal nebular plasma is

$$\frac{M(X)_a}{M(X)_n} = \frac{I(\lambda)_a N(X)_n \epsilon(\lambda)_n}{I(\lambda)_n N(X)_a \epsilon(\lambda)_a}$$

where $I(\lambda)$ indicates the intensity, $N(X)$ the density, and $\epsilon(\lambda)_x$ the emissivities at the appropriate temperatures for the two plasma components. So the mass fraction in the additional component is

$$\text{mass fraction} = 1 - \left(1 + \frac{M(X)_a}{M(X)_n}\right)^{-1}.$$

For the N II $\lambda 5680$ line, we integrate the emission from the middle and bottom panels from Figure 29 to obtain the total emission (within our slit) due to the two plasma components. We find that the additional plasma component emits 76% of the total emission in the N II $\lambda 5680$ line. However, given the adopted temperatures and densities for the two plasma components, the additional plasma component accounts for 35% of the mass of N^{2+} for the volume of the nebula intercepted by our spectrograph slit. If the density is as high as 10^5 cm^{-3} (§3.2.3), the mass fraction drops to 5%. The left panel of Figure 40 presents the variation of the mass fraction of the additional plasma component for densities spanning $10^3 \text{ cm}^{-3} - 10^5 \text{ cm}^{-3}$ and temperatures of $1,000 - 5,000 \text{ K}$. Unless the density is lower than indicated by the N II and O II lines, the additional plasma component accounts for at most half of the mass of N^{2+} in NGC 6153.

For O II $\lambda 4649$, we proceed in a similar manner. We find that the additional plasma component emits 84% of the O II $\lambda 4649$ emission for the volume of the nebula seen by the spectrograph slit, but accounts for only 43% of the O^{2+} mass at the adopted electron densities and temperatures for the two plasma components. This mass fraction falls to 7% if the density is as high as 10^5 cm^{-3} . The right panel in Figure 40 presents the fraction of the mass accounted for by the additional plasma component for a range of relevant temperatures and densities. Again, we find that, unless the density

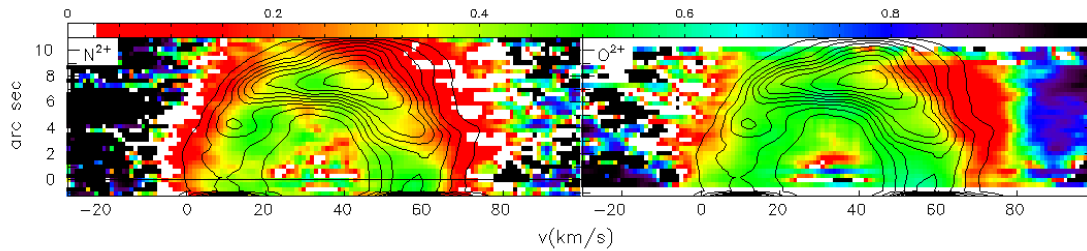


Figure 41. These PV diagrams present the fraction of the mass in the additional plasma component for N^{2+} (left) and O^{2+} (right) computed assuming $(T_e, N_e) = (2,000 \text{ K}, 10,000 \text{ cm}^{-3})$ for the additional plasma component and $(T_e, N_e) = (8,000 \text{ K}, 5,000 \text{ cm}^{-3})$ for the normal nebular plasma. The contours are of the intensity of the $[O \text{ III}] \lambda 4959$ line. Locally, the additional plasma component represents up to 50-60% of the total mass of N^{2+} and O^{2+} and is concentrated in the inner part of the main shell. The region of apparently high fractional mass at the right side of the PV diagram for O^{2+} is due to contamination from the $C \text{ III} \lambda 4650$ line adjacent to the $O \text{ II} \lambda 4649$ line.

for this plasma component has been significantly underestimated, the additional plasma component accounts for about half of the mass of O^{2+} in NGC 6153 seen by the spectrograph slit. This agrees with the results of (Gómez-Llanos & Morisset 2020, theoretical models) and García-Rojas et al. (2022, observations of planetary nebulae with high ADFs).

Figure 41 presents the fractional mass of the additional plasma component in the PV diagram based upon the decomposition of the $N \text{ II} \lambda 5680$ and $O \text{ II} \lambda 4649$ lines using the nominal physical conditions above. Locally, the additional plasma component accounts for up to 50-60% of the total mass of N^{2+} or O^{2+} ions. As expected from the kinematics of the $C \text{ II}$, $N \text{ II}$, $O \text{ II}$, and $Ne \text{ II}$ lines, the maximum of the mass in the additional plasma component is concentrated to the inner part of the main shell, both in velocity and spatial coordinates, in agreement with the spatial distribution of these emission lines (Liu et al. 2000; Tsamis et al. 2008).

4.5. The H mass in the additional plasma component

Having determined the fraction of the mass of O^{2+} contained in the additional plasma component, it is of interest to investigate the fraction of the mass of hydrogen it may contain. As Gómez-Llanos & Morisset (2020) illustrate convincingly, it may be a small minority, making it difficult to determine. We can think of no direct way of probing the H mass fraction, but here present three estimates. The two of the three estimates indicate that the additional plasma component contributes of order 10 – 15% of the emission in $H\beta$, and so of order 3 – 5% of the mass of hydrogen within the area intercepted by our slit in NGC 6153.

The simplest means to estimate the mass of hydrogen in the additional plasma component is to consider its effect upon the kinematic temperature (§3.2.1). Clearly, the additional plasma component must contribute a minority of the $H\beta$ emission; otherwise it would distort the

comparison between the $H\beta$, $H\gamma$ and $[O \text{ III}] \lambda 4959$ lines (Figure 9), since we assume that $[O \text{ III}] \lambda 4959$ arises only in the normal nebular plasma.

To estimate the $H\beta$ emission from the additional plasma component, we assume that its emission will follow that from the $O \text{ II}$ lines and that its temperature is 2,000 K, as found from the $N \text{ II}$ and $O \text{ II}$ lines (§3.2.3). We construct a model of $H\beta$ line based upon the $O \text{ II} \lambda 4649$ line and broadened assuming a temperature of 2,000 K (as described in §3.2.1, subscript *th* below). We then scale this model to different fractions of the total $H\beta$ emission, f , subtract the model from the observed PV diagram for $H\beta$, $I(H\beta)_o$, and compare the remaining $H\beta$ emission with that from the $[O \text{ III}] \lambda 4959$ line (the same as used in §3.2.1). Arithmetically,

$$I(H\beta/4959)_n = \frac{I(H\beta)_o - f \times I(4649)_{o,th}}{I(4959)_{o,th}}.$$

Above some scale factor, subtracting the contribution of the $H\beta$ emission due to the additional plasma component will cause a deficit of $H\beta$ emission compared to $[O \text{ III}] \lambda 4959$, similar to that observed in the top left panel of Figure 9. Once that occurs, we assume that the contribution from the additional plasma component is too great.

Figure 42 presents the results. We consider contributions from the additional plasma component equivalent to 1% – 40% of the total $H\beta$ emission. Contributions below 5% do not cause noticeable changes compared to the observed PV diagram of $H\beta$ (top panel). A 5% contribution (second panel) begins to be noticeable, but in a positive way, making the ratio map even flatter than before. At a 10% contribution (third panel), the ratio is flattest. Beginning at contributions of 15% (fourth panel), there is a deficit of $H\beta$ emission that becomes very notable at 40% (bottom panel). Assuming that the flattest ratio map indicates the most likely estimate of the contribution of the additional plasma component

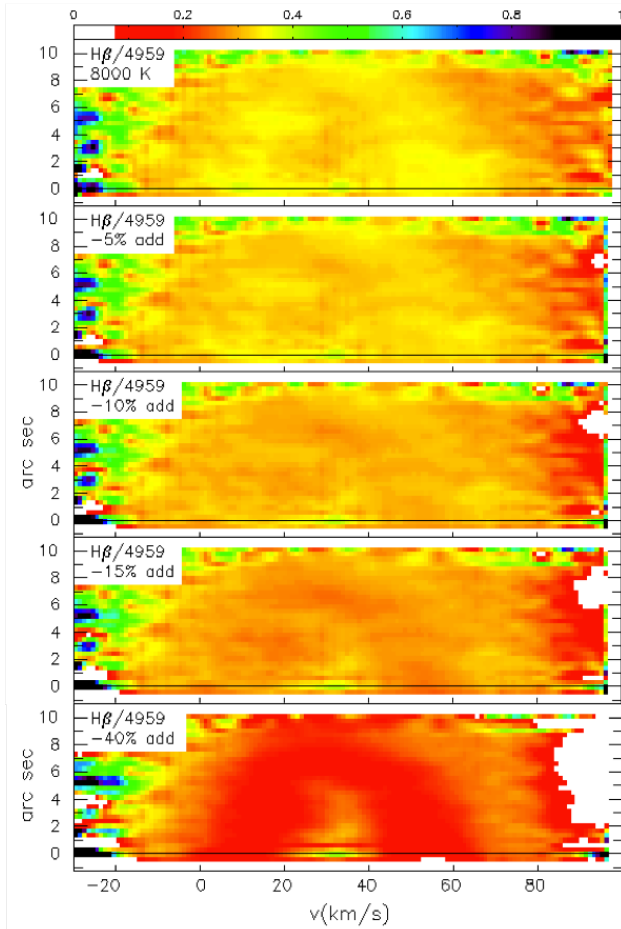


Figure 42. We present the ratio of the PV diagram of the $H\beta$ line and the model of this line based upon the $[O III] \lambda 4959$ line broadened for a temperature of 8,000 K. The top panel considers the observed PV diagram of $H\beta$ (Figure 9). The next four panels consider the observed PV diagram of $H\beta$ after subtracting a contribution due to the additional plasma component, which we model using the $O II \lambda 4649$ line broadened for a temperature of 2,000 K, equivalent to 5%, 10%, 15%, and 40% of the total $H\beta$ emission. Contributions below 5% are not noticeable. For contributions of 5% and 10% (second and third panels), the result is a flatter ratio, presumably indicating that removing the emission due to the additional plasma component improves the agreement for the normal nebular plasma. For contributions of 15% or more (fourth and fifth panels), there is a deficit of $H\beta$ emission at the positions and velocities expected for the additional plasma component.

to the $H\beta$ emission, we attribute 10% of the total $H\beta$ emission to this plasma component, though we probably cannot exclude the range from 5% to 15%. Given the change in emissivity for $H\beta$ between the temperatures of 8,000 K and 2,000 K (Storey & Hummer 1995), a 10% contribution for the emission from the additional plasma component represents 3-4% of the total mass of H.

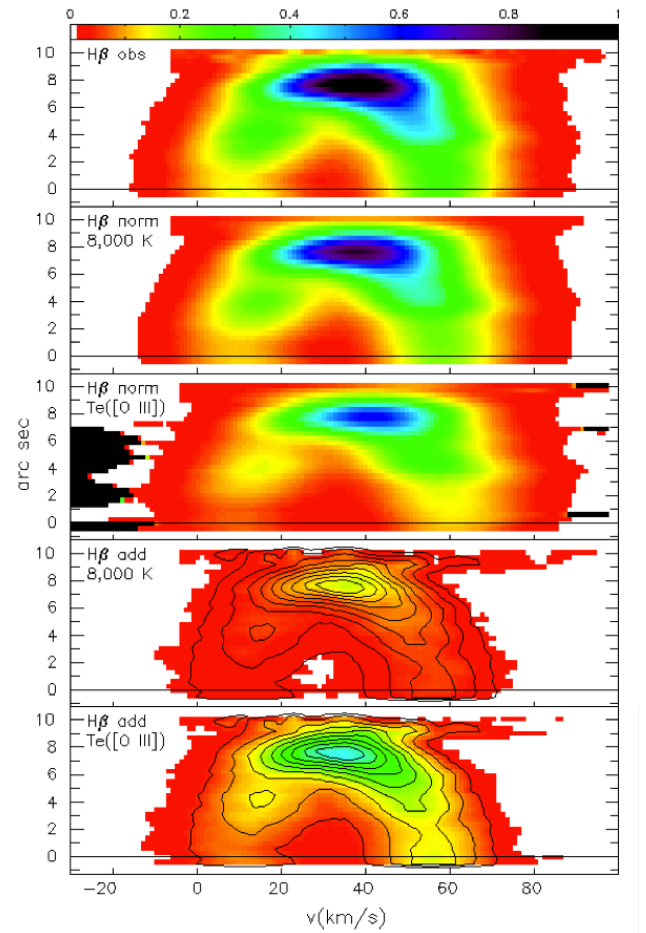


Figure 43. We present the PV diagrams of the observed $H\beta$ line (top panel), predictions of the $H\beta$ emission from the normal nebular plasma based upon the $[O III] \lambda 4959$ line assuming (a) the kinematic temperature of 8,000 K (second panel) and (b) the $[O III]$ temperature map (third panel), and the residual $H\beta$ emission attributable to the additional plasma component assuming a temperature of 8,000 K (fourth panel) and the $[O III]$ temperature map (bottom panel). The contours in the bottom two panels are of the model of the $H\beta$ emission based upon the $O II \lambda 4649$ line broadened for a temperature of 2,000 K (used in Figure 42). All panels share a common color scale. The residual emission amounts to 15.3% (fourth panel) and 41.7% (bottom panel) of the total $H\beta$ emission, i.e., the bottom two panels correspond closely to the contributions supposed in the bottom two panels of Figure 42.

Instead of estimating the $H\beta$ emission of the additional plasma component, we can also estimate the $H\beta$ emission from the normal nebular plasma. We assume that the emission in the $[O III] \lambda 4959$ line is entirely due to the normal nebular plasma. By adopting an electron temperature, we may predict the $H\beta/[O III] \lambda 4959$ ratio via Figure 27. The product of the PV diagram of the $[O III] \lambda 4959$ line (broadened for a temperature of

8,000 K) and the $H\beta/[O\ III]\ \lambda 4959$ ratio gives the predicted $H\beta$ emission per O^{2+} ion. We then scale the result by the H^+/O^{2+} ionic ratio and subtract the result from the observed PV diagram of $H\beta$ to obtain the residual $H\beta$ emission that we attribute to the additional plasma component, $I(H\beta)_a$. When scaling, we fit the predicted $H\beta$ emission to that observed in the diffuse plasma beyond the main shell where the ADF is near unity (§4.3, Figure 39). This second estimate of the $H\beta$ emission from the additional plasma component is

$$I(H\beta)_a = I(H\beta)_o - I(4959)_{o,th} \times \frac{\epsilon(H\beta, T_e)}{\epsilon(4959, T_e)} \times \frac{N(H^+)}{N(O^{2+})}.$$

As regards the electron temperature, we proceed in two ways. First, we assume that the electron temperature is the kinematic temperature of $T_e = 8,000$ K (§3.2.1). The H^+/O^{2+} ionic ratio required in this case is 1200 ± 100 . Second, we assume that the temperature varies as shown in the PV diagram of the [O III] temperature, $T_e = T_e([O\ III])$ computed after broadening the [O III] $\lambda\lambda 4363, 4959$ lines to the width of the $H\beta$ line for a temperature of 8,000 K. The H^+/O^{2+} ratio required in this case is 1400 ± 100 . The H^+/O^{2+} ionic abundances for the two temperatures are similar since the [O III] temperature in the diffuse emission beyond the main shell is near 8,300 K.

Figure 43 illustrates both versions of this second method. The top panel presents the observed $H\beta$ emission. The second panel presents the predicted $H\beta$ emission for the normal nebular plasma supposing an electron temperature of 8,000 K. The third panel presents the predicted $H\beta$ emission supposing the electron temperature given by the [O III] temperature map. The predicted $H\beta$ emission from the normal nebular plasma is less in this second case because the adopted electron temperature is higher in the main shell, 9,000 – 10,000 K. The fourth panel presents difference between the observed $H\beta$ emission (top panel) and that predicted for the normal nebular plasma for an electron temperature of 8,000 K (second panel). The PV diagram of the residual $H\beta$ emission has a morphology similar to that of the PV diagrams of the C II, N II, O II, and Ne II lines (Figure 6). This PV diagram is strictly positive, as it must be if the predicted $H\beta$ emission in the normal nebular plasma is reasonable. The residual emission in the fourth panel amounts to 15.3% of the total $H\beta$ emission. Hence, this estimate implies that the additional plasma component contains about 5% of the total H mass. The bottom panel presents difference between the observed $H\beta$ emission (top panel) and that predicted for the normal nebular plasma for an electron temperature according to the [O III] temperature map (third panel). The

residual emission is greater in this case, 41.7% of the total $H\beta$ emission (approximately 14% of the H mass), but still has a morphology similar to that expected for the additional plasma component.

The estimate of the H mass in the additional plasma component found by subtracting a hypothetical contribution from the observed PV diagram of $H\beta$ agrees with the estimate found by adopting the kinematic temperature as the true electron temperature in the normal nebular plasma. These estimates imply that the H mass of the additional plasma component is 3–5% of the total H mass. The estimate of the H mass in the additional plasma component found when adopting the temperature given by the PV diagram of the [O III] temperature is very different. Indeed, Figure 42 indicates that it is not feasible that the additional plasma component contain so much H if we insist that the $H\beta$ emission from the normal nebular plasma follows that from [O III] $\lambda 4959$. We interpret this discrepancy as the result of adopting an incorrect estimate of the electron temperature.

Finally, if the two plasma components contain similar masses of O^{2+} (§4.4), but the additional plasma component contains only 3–5% of the mass of H, then the O^{2+}/H^+ ionic abundance ratios differ by a factor of 20–30 between the two plasma components. This result confirms the finding from Gómez-Llanos & Morisset (2020) that the ADF is not a particularly good estimate of the difference in chemical composition between the two plasma components. If the O^{2+}/H^+ ionic ratio is 1/1200 or 1/1400 in the normal nebular plasma, $12 + \log(O^{2+}/H^+) = 8.85 - 8.92$ dex, including the additional plasma component implies an overall abundance ratio of approximately 1/600 or 1/700, $12 + \log(O^{2+}/H^+) = 9.15 - 9.22$ dex. (This neglects a -0.013 dex correction for the H in the additional plasma component.)

4.6. On the abundance discrepancy in NGC 6153

The classical understanding of the abundance discrepancy is that permitted and forbidden lines emitted by a given ion indicate different chemical abundances. The temperatures used to compute these abundances are critical, as Peimbert (1967) first pointed out. With few exceptions, the analyses prior to that of Liu et al. (2000) typically supposed a single plasma component and often a single electron temperature for the permitted and forbidden lines.

Our study of NGC 6153 finds conditions that differ markedly from that framework. The kinematics, physical conditions, and relative masses of N^{2+} and O^{2+} yield congruent results regarding the two plasma components that apparently coexist in the nebular shell of

NGC 6153 (§3.1, §3.2, §4.4). Considering two plasma components with very different physical conditions and chemical compositions allows explaining the anomalous electron temperature and density derived from the [N II] $\lambda\lambda 5755, 6583$ and [O II] $\lambda\lambda 3726, 3729$ lines, respectively, as well as the Balmer jump temperature determined by others (§3.3 and §4.2). Even considering the normal nebular plasma alone, there are large-scale temperature gradients and small-scale temperature fluctuations (§3.2 and §4.1), both of which are substantial, but the temperature fluctuations also apparently differ in different volumes of the plasma. All of these are confounding factors that, if not taken into account, will inevitably lead to the conclusion that there is an abundance discrepancy in NGC 6153.

However, if we consider the diffuse emission beyond the main shell in the normal nebular plasma, there is no abundance discrepancy in NGC 6153. There, the ADF is near unity and the [O III] and kinematic temperatures are similar, near 8,000 K. In this volume of the normal nebular plasma, it is particularly simple to determine the O^{2+} ionic abundance (§4.5). Assuming that this ionic abundance holds throughout the normal nebular plasma and that there are similar masses of N^{2+} and O^{2+} ions in the two plasma components, we can estimate the total abundance of O^{2+} ions in the plasma within our spectrograph slit (§4.5). That we obtain similar estimates of the H^+ mass in the additional plasma component assuming (1) an emission pattern like the O II emission from the additional plasma component and its nominal physical conditions and (2) an emission pattern like the [O III] emission from the normal nebular plasma and the kinematic temperature (equivalently, T_0 ; §4.5), indeed implies that it is reasonable to suppose a constant chemical composition within the normal nebular plasma.

To determine the O^{2+} ionic abundance in other volumes of the normal nebular plasma is more difficult, because choices are required. In the main shell, the [O III] and [Ar III] temperatures are substantially higher than the kinematic temperature, the Balmer jump temperature, or T_0 , forcing a choice as to which to use. Using the kinematic temperature or T_0 and the forbidden line intensity would yield the same O^{2+} abundance. However, the ADF is substantial in the main shell, so, to compute the abundance from the permitted lines requires subtracting the majority of the emission that arises in the additional plasma component. Both of these options are possible only because of the quantity of information we have for NGC 6153. This illustrates very clearly the central issue concerning the abundance discrepancy in NGC 6153: It is an information and analysis issue.

Normally, tradition favors using the forbidden line temperatures, because they are much more commonly available and have higher S/N. Also, separating the emission from the two plasma components is usually impossible. So, it is not difficult to imagine an apparent abundance discrepancy arising if the conditions in NGC 6153 are typical. Even if only one plasma component is present, the fundamental lesson from Peimbert (1967) is that all temperature indicators are biased to some extent (Figure 38), so their interpretation is key.

4.7. Beyond NGC 6153

Our findings in NGC 6153 emphasize the complexity that may exist in nebular plasmas. These findings pertain to only the small part of NGC 6153 observed by our spectrograph slit, so there is probably even more complexity lurking within. Although none of the sources of this complexity are new, the combination of multiple plasma components (Liu et al. 2000) and variable temperature fluctuations (Peimbert 1967) implies a degree of complexity not considered previously. The plasma in other objects may be less, or more, complex. When possible, this complexity should be taken into account when computing the elemental/ionic abundances in planetary nebulae, at least.

The plasma's complexity manifests itself directly in the line intensities and so the interpretation of the line intensities requires care. In particular, it is necessary to correct the intensities of the auroral lines of [N II] and [O II] for contributions due to recombination if the volume of O^{2+} observed is large. Otherwise, the derived electron temperatures will be too large, biasing the abundance calculations, even if only one plasma component is present. The density determined from the [O II] nebular lines may be significantly affected if the volume observed includes multiple plasma components, as this density will reflect the density of different plasma components in different parts of the nebula. There is considerable documentation of the contamination of the [N II] $\lambda 5755$ and [O II] lines in the literature (e.g., Liu et al. 2000; Tsamis et al. 2003; Wesson et al. 2005; Liu et al. 2006; Corradi et al. 2015; Ruiz-Escobedo & Peña 2022), and we advocate that the contamination of these lines be taken into account in those cases where it is reasonable to expect it to be important.

If the volume of He^{2+} included in the observations is large, the intensity of the [O III] $\lambda 4363$ line may also need correction. As Gómez-Llanos et al. (2020) point out, the excitation of the [O III] $\lambda 4363$ due to recombination is less sensitive to temperature than many lines, varying much less than the usual $\sim T^{-1}$ assumption, so the recombination contribution may be more important

from the normal nebular plasma than from the colder additional plasma component. In this case, we caution against using the O III lines involved in the Bowen fluorescence cascade to deduce the corrections necessary since they will not reflect the true abundance of O^{3+} (e.g., Liu & Danziger 1993; Kastner & Bhatia 1996; Selvelli et al. 2007).

The [O III] temperature is sensitive to the presence of the He^{2+} zone, since this zone may include a considerable O^{2+} content as a result of the efficiency of charge exchange with O^{3+} . Normally, the temperature is higher in the He^{2+} zone due to the extra heating that occurs there (e.g., Gómez-Llanos & Morisset 2020), which will affect the intensity of [O III] $\lambda 4363$ preferentially. Hence, the often-adopted tactic of correcting for the recombination contribution to the [O III] $\lambda 4363$ line assuming a flat spatial distribution of the [O III] temperature through the central zone of the nebula (where the He^{2+} is found) is likely to over-correct for the contribution of recombination to the excitation of this line, i.e., one problem substitutes for another.

If the physical conditions indicated by the N II and O II lines are representative (§3.2.3), the additional plasma component is colder by a factor of ~ 3 and denser by a factor of $\gtrsim 2$ compared to the normal nebular plasma in NGC 6153. If so, the two plasma components appear to be close to being in pressure equilibrium. Using similar means, Richer et al. (2019) found that the two plasma components may be in pressure equilibrium in NGC 7009. Peimbert et al. (2014) found a similar result for their sample of planetary nebulae, with the pressures computed using forbidden and permitted lines being within a factor of a few of being in equilibrium.

Although there is no commonly-accepted explanation of how they are maintained, temperature fluctuations appear to be important in the normal nebular plasma in NGC 6153, so they should be taken into account. While it is tempting to argue that any abundance calculation that does not consider temperature fluctuations should be considered as only a lower limit to the true value, both this study and that of Richer et al. (2019) of NGC 7009 demonstrate that there may be regions within any given object where temperature fluctuations are negligible. So, while it is not simple to decide how to proceed, having multiple reliable temperature indicators is the best guide as to which temperature to adopt when calculating chemical abundances.

NGC 6153 joins a growing list of objects whose permitted lines of C II, N II, O II, and Ne II have kinematics that are anomalous with respect to the ionization structure defined by other lines (Sharpee et al. 2004; Barlow et al. 2006; Otsuka et al. 2010; Richer et al. 2013,

2017; Peña et al. 2017; Ruiz-Escobedo & Peña 2022). Unfortunately, multiple plasma components can only be recognized via high resolution spectroscopy or if the spatial profile of the emission lines is available (e.g., Liu et al. 2000; Garnett & Dinerstein 2001; Tsamis et al. 2008; Monreal-Ibero & Walsh 2020; García-Rojas et al. 2022).

In most previous studies of this issue, the additional plasma component is represented only through the emission of the C II, N II, O II, and Ne II lines. However, Corradi et al. (2015) and García-Rojas et al. (2022) find that the O I $\lambda\lambda 7771, 7774, 7775$ lines imply an O^+ abundance discrepancy in Ou 5, NGC 6778, M 1-42, and Hf 2-2. Here, we also find that the emission from the permitted quintuplet lines of O I, which cannot be excited by fluorescence from the ground state, have kinematics that are compatible with belonging to the additional plasma component. Thus, O I represents a second ionization stage of oxygen identified in the additional plasma component. This is perhaps the most significant evidence that the additional plasma component is a distinct plasma from the normal nebular plasma, since the presence of O I emission indicates that there are two ionization structures.

Here, we also find similar kinematics for the additional plasma component using lines of O II that span a wide range of energy levels (Table 8), e.g., the upper level of O II $\lambda 6501.4$ is $2p^2 6g$ within 1.5 eV of the ionization limit while the lower level of the V1 multiplet, $2p^2 3s$, is the first excited state above the ground level (for the $2p^2 (^3P)$ core configuration). This demonstrates that fluorescence, including indirect fluorescence, is not a viable explanation of the kinematics of the additional plasma component in NGC 6153, or of the abundance discrepancy problem more generally.

Both Liu et al. (2000) and Tsamis et al. (2008) found that the O^{2+}/H ratio from permitted lines was more centrally concentrated in NGC 6153 than the same ratio computed from forbidden lines. Figures 39 and 41 indicate the same result here. This agrees with essentially all studies that can address the issue, the spatial distribution of the emission from the permitted lines of C II, N II, O II, and Ne II is more compact than that of the forbidden lines from the same ions (e.g., Barker 1982, 1991; Garnett & Dinerstein 2001; Luo & Liu 2003; García-Rojas et al. 2022). Thus, while the kinematics of the C II, N II, O II, and Ne II lines can address the spatial location of the plasma only indirectly, via the hypothesis that the multiple plasmas follow a typical relation between velocity and ionization energy (Wilson 1950), the spatial distribution confirms that both are found in the inner part of the nebula, close to the central

star, supporting a common [Wilson \(1950\)](#)-like relation for all plasma components. So far, though, no study is able to spatially isolate a “clump” of the additional plasma component ([García-Rojas et al. 2022](#)), so its topology within the nebular shell remains a mystery.

As [Gómez-Llanos & Morisset \(2020\)](#) point out, the abundance discrepancy factor is a poor descriptor to relate the chemical compositions of the two plasmas because of the difficulty of apportioning the emission from hydrogen between the two plasma components. Fortunately, they find that the normal nebular plasma emits the great majority of the hydrogen emission. While it would be useful to have a more general study of this effect, it seems likely that the basic result will remain, as we find for NGC 6153. Under these circumstances, it is probably more instructive, as [Liu et al. \(2006\)](#) first pointed out, to compare the masses of O^{2+} (or CNO elements) in the two plasma components. That way, the “usual” techniques to determine the chemical composition of the normal nebular plasma may be leveraged to estimate the overall chemical composition considering both plasma components. Here, it appears that the overall abundance of N^{2+} and O^{2+} is no more than double the abundance of these ions in the normal nebular plasma in NGC 6153. Similar results have been found for NGC 7009, NGC 6778, M 1-42, and Hf 2-2 ([Liu et al. 2006](#); [Richer et al. 2019](#); [García-Rojas et al. 2022](#)).

An important observation is that abundance ratios, such as C/O, are similar in both plasma components, as was first noted by [Liu et al. \(2000\)](#). When two plasma components are present with arbitrary absolute abundances of C, N, and O, it is not evident why the relative abundances in the two components need be maintained. Hence, it is unlikely that the additional plasma component has an origin in an event such as a very late thermal pulse, since that would dramatically change the relative abundances (e.g., as observed in A 38, A 58, and A 78; [Jacoby & Ford 1983](#); [Lau et al. 2011](#)). However, as [García-Rojas et al. \(2022\)](#) point out, common relative abundances could arise naturally if the additional plasma component is ejected later from a more internal layer of the progenitor star. The question would then be why that would happen or be evident only in some objects, such as NGC 6153, and not in all.

The work of [Bautista & Ahmed \(2018\)](#), who model a nebula whose central star is periodically eclipsed, may offer an alternative to the two plasma components we advocate here. The particular nebula they model is not a good approximation to NGC 6153, but, if the amplitude of their resonant temperature fluctuations varies sufficiently rapidly with depth, it might mimic the behavior of two plasma components within a single plasma

and binary stars appear to be very common among planetary nebulae with large abundance discrepancies (e.g., [Wesson et al. 2018](#)). While the return to a single plasma is a major simplification, the model’s time-variable ionizing flux and the plasma’s departure from a steady state equilibrium are very significant complications. We encourage further work on this front as it is congruent with our argument that it is necessary to better consider the complexity of the nebular plasma.

5. CONCLUSIONS

We present a detailed study of the kinematics of the emission lines in NGC 6153 based upon echelle spectra obtained with the UVES spectrograph at the ESO VLT. Our first conclusion is that the plasma in NGC 6153’s nebular shell is complex. We find that there are two plasma components. What we call the normal nebular plasma emits in all lines and behaves generally as described in textbooks. What we call the additional plasma component emits in the lines of O I, C II, N II, O II, and Ne II. The additional plasma component contributes a small fraction of the H I emission. Within both plasma components, the usual physics of nebular plasmas appears to hold and we find consistent results for the physical conditions from multiple lines of evidence.

The kinematics of the two plasma components are distinct. Except for the permitted lines of O I (quintuplet states), C II, N II, O II, and Ne II, all lines follow a single relation between velocity splitting and ionization energy ([Wilson 1950](#)), and is the means by which we define the normal nebular plasma. These permitted and forbidden lines arise from a variety of physical processes (recombination, collisional excitation, Bowen fluorescence, and charge exchange). The permitted lines of O I (quintuplets), C II, N II, O II, and Ne II all have the same velocity splitting even though the energies needed to create the parent ions differ widely, defining the additional plasma component. Thus, we confirm a second ionization state, O^+ , for the additional plasma component (see also [Corradi et al. 2015](#); [García-Rojas et al. 2022](#)). In the case of the O II lines, lines arising from energy levels spanning from just below the ionization threshold to the first excited state above ground all present similar kinematics. Multiple ionization stages of oxygen and the similar kinematics from a wide variety of lines of O II argue that two plasma components coexist in the nebular shell of NGC 6153. As has been found in studies of the spatial distribution of C II, N II, O II, and Ne II lines, we also find that these lines are concentrated towards the inner part of NGC 6153’s main shell (e.g., [Barker](#)

1982, 1991; Liu et al. 2000; Garnett & Dinerstein 2001; Tsamis et al. 2008; García-Rojas et al. 2016, 2022).

We determine the physical conditions in both plasma components. For the normal nebular plasma, the kinematics, the He I lines and the forbidden lines of [N II] (once corrected), [O III], and [Ar III] all imply temperatures of 8,000–10,000 K while the H I lines and the forbidden lines of [S II], [Cl III], and [Ar IV] imply electron densities in the neighborhood of 5,000 cm⁻³. For the additional plasma component, we determine the electron temperature and density from the N II and O II lines, finding $T_e \sim 2,000$ K and $N_e > 5,000$ cm⁻³ (and possibly as high as 10⁵ cm⁻³). The [O II] $\lambda\lambda 3726, 3729$ lines imply a density of $\sim 10,000$ cm⁻³ where their emission may be dominated by recombination excitation in the additional plasma component. Given these physical conditions, the additional plasma component contains a mass of N²⁺ and O²⁺ similar to that found in the normal nebular plasma (for $N_e = 10,000$ cm⁻³; a smaller fraction if the density is higher). When we compute the ADF for O²⁺ resolved in velocity and position, we find that it peaks in the inner part of NGC 6153's main shell, but that the ADF falls to unity in the diffuse emission beyond the receding side of the main shell, i.e., there is no abundance discrepancy in that volume of the plasma.

Supposing the existence of two plasma components, we find that recombination excitation from the additional plasma component dominates the emission in the [N II] $\lambda 5755$ and [O II] $\lambda 7320, 7330$ auroral lines in some volumes of the nebular shell (e.g., Liu et al. 2000; Tsamis et al. 2003; Corradi et al. 2015; Ruiz-Escobedo & Peña 2022). However, there are also volumes of the plasma where the collisional excitation dominates the emission and the usual interpretation of these lines applies. We recommend caution in using the auroral transitions of the [N II] and [O II] lines in any circumstance when the observation includes a large volume of the O²⁺ zone. A similar exercise shows that the emission in the [O III] $\lambda 4363$ line is dominated by the normal nebular plasma and its use as a temperature indicator is unaffected in NGC 6153. However, as for the auroral lines of [N II] and [O II], the [O III] $\lambda 4363$ line may be suspect when the He²⁺ zone dominates the volume included in the observation.

There are clear temperature variations within the normal nebular plasma. There are large-scale variations, for instance a higher temperature where helium is doubly ionized, though even the He²⁺ zone is not near isothermal. Although the [Ar III] and [O III] temperatures are very similar, differing by only $\sim 300 - 600$ K, they both exceed the temperature found from the kinematics of the H β , H γ , He I $\lambda\lambda 4471, 4922$, and [O III] $\lambda 4959$ lines, which should be sensitive to the motions of the ions involved. The average Balmer jump temperature in NGC 6153 found by others is consistent with the temperatures we find for the two plasma components (Liu et al. 2000; Zhang et al. 2004; McNabb et al. 2016). However, we cannot explain why it is constant over the minor axis (Liu et al. 2000) since the concentration of the additional plasma component to the central part of the nebula should lower it there, as found by García-Rojas et al. (2022).

When two plasma components are present, with distinct physical conditions, the relevance of an abundance discrepancy becomes less obvious. Furthermore, the ADF may be a poor description of the abundances in the additional plasma component (Gómez-Llanos & Morisset 2020; García-Rojas et al. 2022), so instead we advocate following Liu et al. (2006) in computing the fraction of O²⁺ (or CNO ions) contributed by the additional plasma component as a clearer indicator of the relevance of the additional plasma component. The observation that the relative abundances of the CNO elements appear to be similar in both plasma components indicates that the two plasmas are not completely independent (Liu et al. 2000).

We gratefully acknowledge financial support from UNAM DGAPA grant PAPIIT IN103519, CONACyT grant A1-S-15140, and the Departamento de Investigación of the Universidad Iberoamericana. We thank the anonymous referee for helping to improve this work very substantially.

Software: IDL, IRAF (Tody 1986, 1993), Microsoft Office (Microsoft Corporation 2016), Python (Van Rossum & Drake 2009), PyNeb (Luridiana et al. 2015), SAOImageDS9 (Joye & Mandel 2003)

REFERENCES

- Aller, L. H. 1984, *Physics of Thermal Gaseous Nebulae* (Dordrecht, the Netherlands: Springer)
- Axner, O. et al. 2004, *Spectrochimica Acta*, Part B, 59, 1
- Barker, T. 1982, *ApJ*, 253, 167
- Barker, T. 1991, *ApJ*, 371, 217
- Barlow, M. J. et al. 2006, in *Proc. IAU Symp.* 234, *Planetary Nebulae in our Galaxy and Beyond*, ed. M. J. Barlow & R. H. Méndez (Cambridge: Cambridge Univ. Press), 367
- Bautista, M. A., & Ahmed, E. E. 2018, *ApJ*, 866, 43

- Bowen, I. S. 1960, *ApJ*, 132, 1
- Butler, K., & Zeppen, C. J. 1989, *A&A*, 208, 337
- Cardelli, J. A., Clayton, G. C., & Mathis, J. S. 1989, *ApJ*, 345, 245
- Clegg, R. E. S. et al. 1999, *A&AS*, 135, 359
- Courtès, G. et al. 1968, *Annales d'Astrophysique*, 31, 493
- Corradi, R. L. M. et al. 2015, *ApJ*, 803, 99
- Dalgarno, A., & Sternberg, A. 1989, *ApJL*, 257, 87
- Dalgarno, A. et al. 1981, *ApJ*, 245, 793
- Dekker, H. et al. 2000, *Proc. SPIE*, 4008, 534
- Dyson, J. E., & Meaburn, J. 1971, *A&A*, 22, 33
- Ercolano, B. et al. 2003, *MNRAS*, 344, 1145
- Ercolano, B., & Storey, P. J. 2006, *MNRAS*, 372, 1875
- Escalante, V. 2002, *RMxAA Conf. Ser.*, 12, 22
- Fang, X. et al. 2011, *A&A*, 530, A18
- Fang, X. et al. 2013, *A&A*, 550, C2
- Fitzpatrick, E. L. 1999, *PASP*, 111, 63
- Frew, D. 2008, PhD thesis, Macquarie University
- Froese-Fischer, C., & Tachiev, G. 2004, *Atomic Data and Nuclear Data Tables*, 87, 1
- García-Díaz et al. 2008, *RMxAA*, 44, 181
- García-Rojas, J. et al. 2016, *ApJL*, 824, 27
- García-Rojas, J. et al. 2022, *MNRAS*, 510, 5444
- Garnett, D. R., & Dinerstein, H. L. 2001, *ApJ*, 558, 145
- Gómez-Llanos, V., & Morisset, C. 2020, *MNRAS*, 497, 3363
- Gómez Llanos, V. et al. 2020, *MNRAS*, 498, L82
- Grandi, S. A. 1976, *ApJ*, 206, 658
- Hamuy, M. et al. 1992, *PASP*, 104, 533
- Hamuy, M. et al. 1994, *PASP*, 106, 566
- Jacoby, G. H., & Ford, H. C. 1983, *ApJ*, 266, 298
- Joye, W. A., & Mandel, E. 2003, in *Astronomical Data Analysis Software and Systems XII*, ASP Conference Series, Vol. 295 (San Francisco: PASP), eds. H. E. Payne, R. I. Jedrzejewski, and R. N. Hook, 489
- Kastner, S. O., & Bhatia, A. K. 1996, *MNRAS*, 279, 1137
- Kingsburgh, R. L., & Barlow, M. J. 1994, *MNRAS*, 271, 257
- Kisielius, R. et al. 2009, *MNRAS*, 397, 903
- Kramida, A., Ralchenko, Yu., Reader, J., and NIST ASD Team (2021). NIST Atomic Spectra Database (ver. 5.9), [Online]. Available: <https://physics.nist.gov/asd>. National Institute of Standards and Technology, Gaithersburg, MD.
- Lau, H. H. B., De Marco, O., & Liu, X.-W. 2011, *MNRAS*, 410, 1870
- Liu, X.-W., & Danziger, J. 1993, *MNRAS*, 261, 465
- Liu, X.-W. et al. 1995, *MNRAS*, 272, 369
- Liu, X.-W. et al. 2000, *MNRAS*, 312, 585
- Liu, X.-W. et al. 2006, *MNRAS*, 368, 1959
- Luo, S.-G., & Liu, X.-W. 2003, in *IAU Symp.* 209, *Planetary Nebulae: Their evolution and role in the universe*, ed. S. Kwok, M. A. Dopita, R. Sutherland (San Francisco: ASP), 393
- Luridiana, V. et al. 2015, *A&A*, 573, A42
- McCall, M. L., & Armour, M.-H. 2000, in *ASP Conf. Ser.* 218, *Mapping the Hidden Universe: The Universe behind the Milky Way: The Universe in H I*, ed. R. C. Kraan-Korteweg, P. A. Henning, & H. Andernach (San Francisco: ASP), 1
- McNabb, I. A. et al. 2016, *MNRAS*, 461, 2818
- Mesa-Delgado, A. et al. 2009, *MNRAS*, 395, 855
- Microsoft Corporation, 2016, *Microsoft Excel*, Available at: <https://office.microsoft.com/excel>
- Monreal-Ibero, A., & Walsh, J. R. 2020, *MNRAS*, 634, A47
- Morton, D. C. 2003, *ApJS*, 149, 205
- Muñoz Burgos, J. M. et al. 2009, *A&A*, 500, 1253
- Nussbaumer, H., & Storey, P. J. 1984, *A&AS*, 56, 293
- Osterbrock, D. E. et al. 1996, *PASP*, 108, 277
- Osterbrock, D. E. et al. 1997, *PASP*, 109, 614
- Osterbrock, D. E., & Ferland, G. J. 2006, *Astrophysics of Gaseous Nebulae and Active Galactic Nuclei* (Melville, USA: University Science Books)
- Otsuka, M. et al. 2010, *ApJ*, 723, 658
- Peimbert, M. 1967, *ApJ*, 150, 825
- Peimbert, M. 2019, eprint arXiv:1905.01244
- Peimbert, A. et al. 2014, *RMxAA*, 50, 329
- Peña, M. et al. 2017, *MNRAS*, 472, 1182
- Péquignot, D. et al. 1991, *A&A*, 251, 680
- Péquignot, D. et al. 2002, *Revista Mexicana de Astronomía y Astrofísica, Serie de Conferencias*, 12, 142
- Porter, R. L. et al. 2013, *MNRAS*, 433, L89
- Pottasch, S. R. et al. 2003, *A&A*, 409, 599
- Ramsbottom, C. A., & Bell, K. L. 1997, *Atomic Data and Nuclear Data Tables*, 66, 65
- Richer, M. G. et al. 2013, *ApJ*, 773, 133
- Richer, M. G. et al. 2017, *AJ*, 153, 140
- Richer, M. G. et al. 2019, *ApJ*, 870, 42
- Roueff, E., & Dalgarno, A. 1988, *Physical Review A*, 38, 93
- Rubin, R. H. 1986, *ApJ*, 309, 334
- Ruiz-Escobedo, F., & Peña, M. 2022, *MNRAS*, 510, 5984
- Rynkun, P. et al. 2019, *A&A*, 623, A155
- Selvelli, P. et al. 2007, *A&A*, 464, 715
- Sharpee, B. et al. 2004, *ApJ*, 615, 323
- Stevenson, C. C. 1994, *MNRAS*, 267, 904
- Storey, P. J., & Hummer, D. G. 1995, *MNRAS*, 272, 41
- Storey, P. J., & Zeppen, C. 2000, *MNRAS*, 312, 813
- Storey, P. J. et al. 2014, *MNRAS*, 441, 3028
- Storey, P. J. et al. 2017, *MNRAS*, 470, 379

- Tachiev, G., & Fischer, C. F. 2001, *Canadian Journal of Physics*, 79, 955
- Tayal, S. S. 2007, *ApJS*, 171, 331
- Tayal, S. S. 2011, *ApJS*, 195, 12
- Tayal, S. S., & Zatsarinny, O. 2010, *ApJS*, 188, 32
- Tody, D. 1986, in *Proc. SPIE Instrumentation in Astronomy VI*, ed. D.L. Crawford, 627, 733
- Tody, D. 1993, in *Astronomical Data Analysis Software and Systems II*, A.S.P. Conference Ser., Vol 52, eds. R.J. Hanisch, R.J.V. Brissenden, & J. Barnes, 173
- Torres-Peimbert, S. et al. 1990, *A&A*, 233, 540
- Tsamis, Y. G. et al. 2003, *MNRAS*, 345, 186
- Tsamis, Y. G., & Péquignot, D. 2005, *MNRAS*, 364, 687
- Tsamis, Y. G. et al. 2008, *MNRAS*, 386, 22
- Tylenda, R. 2003, in *Proc. IAU Symp. 209, "Planetary Nebulae: Their Evolution and Role in the Universe"* (ed. S. Kwok, M. Dopita, & R. Sutherland, *Astronomical Society of the Pacific: San Francisco*), 389
- Van Hoof, P. A. M. 2018, *Galaxies*, 6, 63
- Van Rossum, G., & Drake, F. L. 2009, *Python 3 Reference Manual* (Scotts Valley, CA: CreateSpace)
- Wenåker, I. 1990, *Physica Scripta*, 42, 667
- Walsh, J. R. et al. 2018, *A&A*, 620, A169
- Wesson, R., Liu, X.-W., & Barlow, M. J. 2005, *MNRAS*, 362, 424
- Wesson, R., Jones, D., García-Rojas, J. et al. 2018, *MNRAS*, 480, 4589
- Wiese, W. L. et al. 1996, *Journal of Physical and Chemical Reference Data*, Monograph 7, 403
- Wilson, O. C. 1950, *ApJ*, 111, 279
- Wyse, A. B. 1942, *ApJ*, 95, 356
- Yuan, H. B. et al. 2011, *MNRAS*, 411, 1035
- Zeippen, C. 1982, *MNRAS*, 198, 111
- Zhang, Y. et al. 2004, *MNRAS*, 351, 935

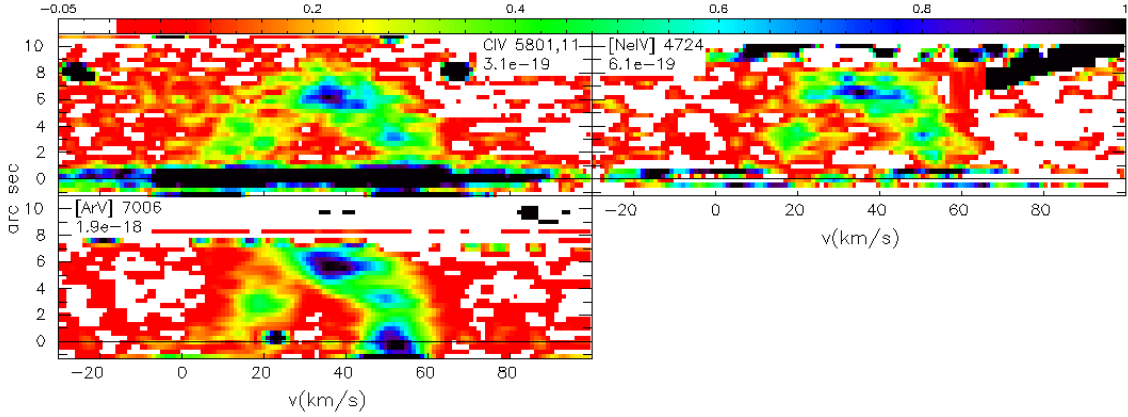


Figure 44. These panels present the PV diagrams of the lines of highest ionization: C IV $\lambda\lambda 5801,5811$, [Ne IV] $\lambda 4724$, and [Ar V] $\lambda 7006$. Note that there is also C IV emission from the central star. In general, the receding side of the main shell and its outer edge (at top) are the brightest features. The approaching side of the main shell is fainter, but a feature half-way to the outer edge is visible in all three PV diagrams. Although it is discontinuous, the velocity ellipse has a semicircular shape in these PV diagrams.

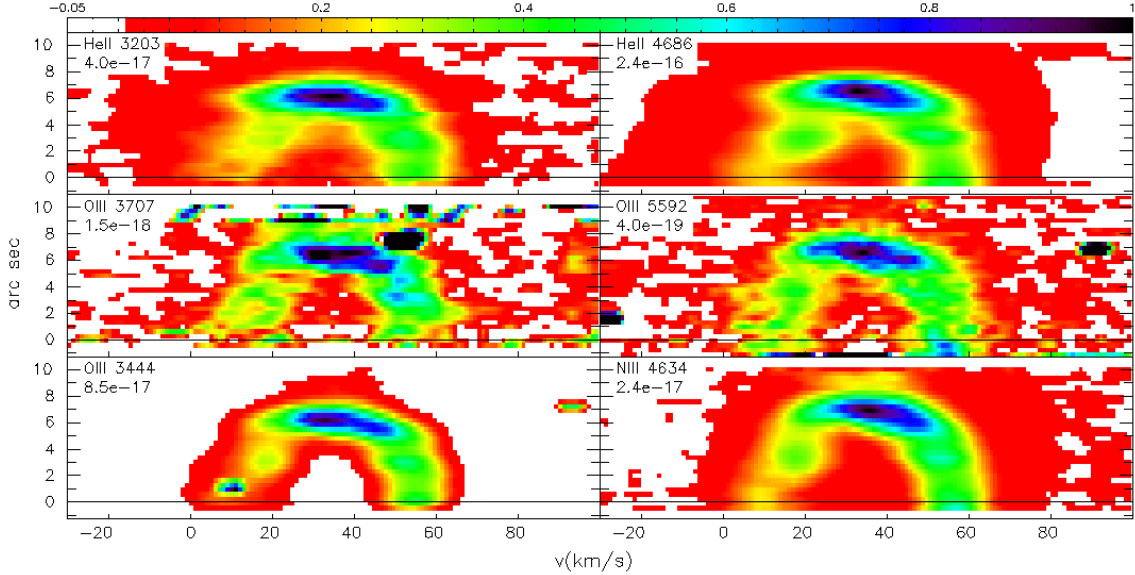


Figure 45. These panels present lines of high ionization: He II $\lambda 3203$, He II $\lambda 4686$, O III $\lambda 3707$ (recombination), O III $\lambda 5592$ (charge exchange), O III $\lambda 3444$ (Bowen fluorescence), and N III $\lambda 4634$ (Bowen fluorescence). In terms of shape, these PV diagrams are more square than those in Figure 44 and extend to a larger distance from the central star.

APPENDIX

A. MORPHOLOGY OF THE PV DIAGRAM

Here, we compare the morphology observed in the PV diagrams for emission lines emitted by many ions. Our primary intention is to demonstrate the robustness of the results presented in §3.1, since PV diagrams provide more information than may be represented in the Wilson diagram (Figure 5).

Figures 44-50 present a selection of the many PV diagrams from which we derive the Wilson diagram (Figure 5). The order of these figures is from the lines arising from the ions with the highest degree of ionization (e.g., C⁴⁺; Figure

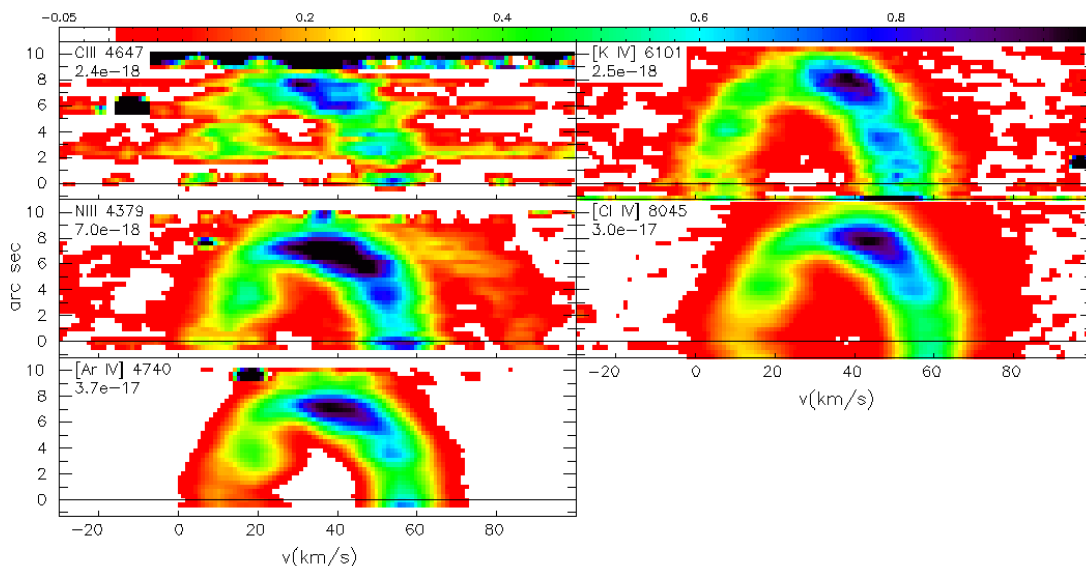


Figure 46. These panels present the PV diagrams for the lines of C III $\lambda 4647$, [K IV] $\lambda 6101$, N III $\lambda 4379$ (O III $\lambda 4379.6$ is the second/redder line), [Cl IV] $\lambda 8045$, and [Ar IV] $\lambda 4740$. The velocity ellipse in these PV diagrams has returned to a rounder shape than in Figure 45, largely because of the greater velocity splitting.

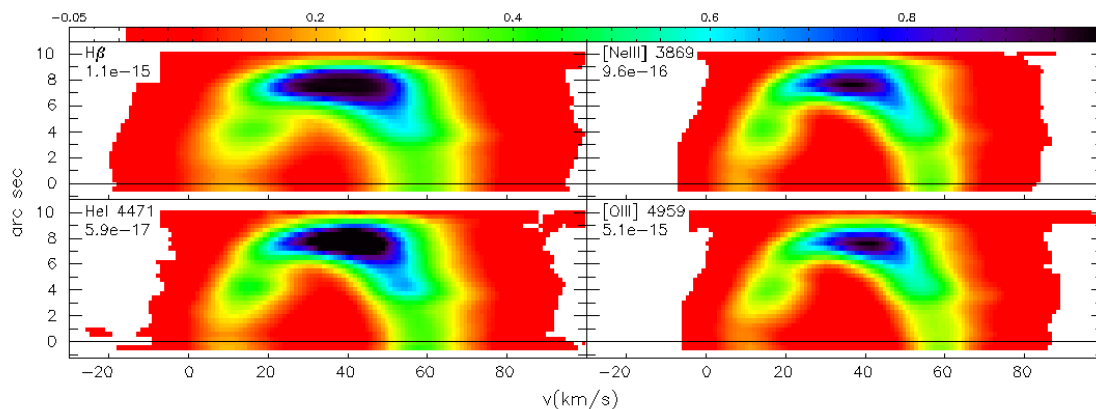


Figure 47. These panels present the PV diagrams in the lines of H I β , [Ne III] $\lambda 3869$, He I $\lambda 4471$, and [O III] $\lambda 4959$, lines that sample the majority of the mass of the nebula (all of it for H I), all from the CD2 wavelength interval. Compared to the lines in Figure 46, there is clearly less emission from the receding side of the main shell for lines of sight close to the central star.

44) through the lines arising from the ion with the lowest degree of ionization (e.g., O⁰; Figure 50). The morphologies of these PV diagrams present coherent trends and so define a kinematic structure that varies continuously as a function of ionization. We recall that the slit length is shorter for wavelengths below 5000Å than for longer wavelengths.

Considering Figures 44-49 individually, the component PV diagrams in each figure present similar morphologies. That is, in Figure 44, for example, although the S/N varies (and is never high), the PV diagrams for C IV $\lambda\lambda 5801, 5811$, [Ne IV] $\lambda 4724$, and [Ar V] $\lambda 7006$ show similar structures. In all lines, the emission from the main shell is broken into 3-4 components that define a velocity ellipse. The fourth component, due to the receding side of the main shell along the line of sight to the central star, is only visible in the [Ar V] $\lambda 7006$ line due to residuals in the subtraction of the emission from the central star. (In the case of C IV $\lambda\lambda 5801, 5811$, the central star has emission lines that are not removed by the continuum subtraction.) In all lines, the top of the main shell is the brightest feature while the approaching and receding sides of the main shell are fainter. Also, the spatial extent of the main shell in all of these highly ionized ions is similar, i.e., the top of the ellipse defined by the main shell is at the same distance from the

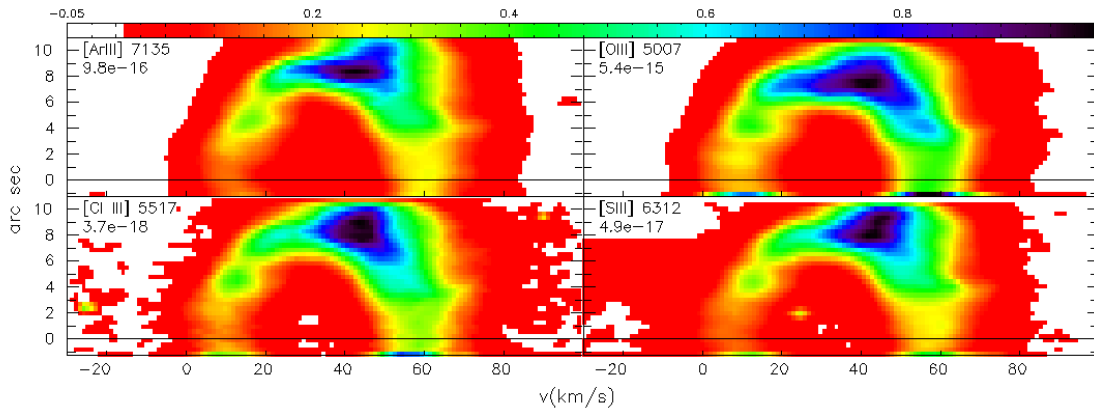


Figure 48. These panels present the PV diagrams for [Ar III] $\lambda 7135$, [O III] $\lambda 5007$, [Cl III] $\lambda 5517$, and [S III] $\lambda 6312$. Compared to [O III] $\lambda 5007$, the other three lines have even less emission from the receding side of the main shell along lines of sight near the central star, but more emission from the filament beyond the receding side of the main shell (Figure 4). The difference between [O III] $\lambda 5007$ and [O III] $\lambda 4959$ (Figure 47) is due to the longer slit for lines to the red of 5000 \AA and a slight shift in the position of the slit perpendicular to its length.

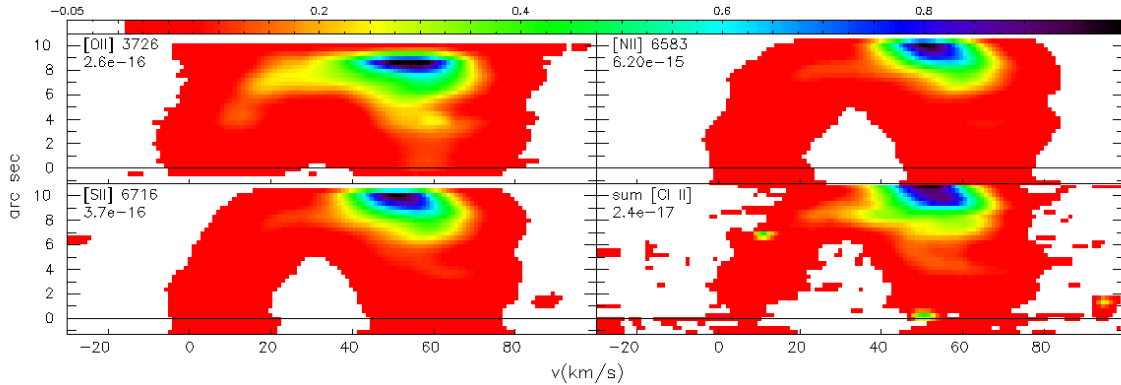


Figure 49. These panels present the PV diagrams for the lines of [O II] $\lambda 3726$, [N II] $\lambda 6583$, [S II] $\lambda 6716$, and the sum of [Cl II] $\lambda \lambda 8578, 9123$. In all of these lines, the emission from the main shell is much weaker than in the previous figures while the only bright emission comes from the filament outside the main shell. Even so, the main shell is brighter in the [O II] $\lambda 3726$ line than in the other lines, the result of collisional excitation (§3.3).

central star in all of the PV diagrams. Although the details vary, in each of Figures 44-49, the morphologies of the component PV diagrams are similar, indicating that the lines presented in each of these figures arise from volumes of plasma of with similar kinematics and similar spatial distributions, i.e., they are largely the same volume of plasma in each figure.

There are also systematic changes when proceeding from figure to figure in the sequence from Figure 44 to Figure 50. For instance, the velocity ellipse in the three PV diagrams in Figure 44 has a shape that is approximately a semicircle while it is somewhat more square in Figure 45. Also, the edge of the main shell is farther from the position of the central star in Figure 45 than in Figure 44. The similar morphologies of the PV diagrams in Figure 45 indicates that they arise in similar volumes of the nebular plasma, in spite of the variety of physical processes involved. Comparing Figure 45 (He⁺⁺/O³⁺ zone and O³⁺ \rightarrow O⁺⁺ transition zone) and Figure 46 (the zone containing C³⁺, N³⁺, Cl³⁺, Ar³⁺, and K³⁺), the emission from the receding side of the main shell becomes more spatially continuous, i.e., a full arc is now visible from the receding side of the main shell. These changes reflect a change in the volume of the plasma that emits in the lines presented in the two figures. Proceeding from Figure 46 to Figure 47, the main change is a decrease in the brightness of the receding side of the main shell along lines of sight near the central star in Figure 47, which presents the PV diagrams for the lines that sample most (or all) of the nebular mass. This effect continues in

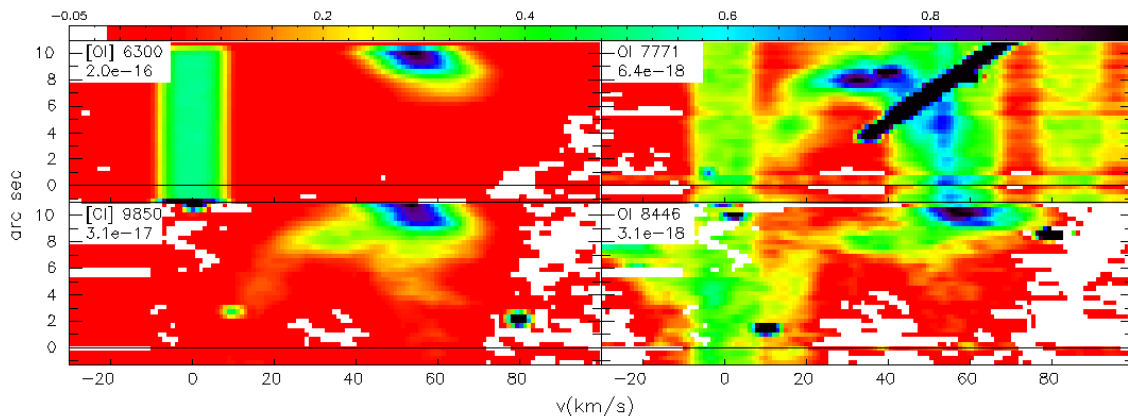


Figure 50. The panels in the left column present the PV diagrams in the lines of lowest ionization potential, [O I] λ 6300 and [C I] λ 9850. In [O I] λ 6300, emission from the main shell is now nearly absent. In the right column, the panels contrast the PV diagrams of the O I λ 7771 and O I λ 8446 lines. The different morphologies likely arise due to different physical processes contributing to the two lines. The black streak is a cosmic ray.

Figure 48, where the emission is quite faint from the receding side of the nebular shell along lines of sight near the central star (except for [O III] λ 5007, which repeats from the previous figure). However, in Figure 48, the emission from the filament on the approaching side of the nebula is now fainter and the emission from the filament, beyond the main shell on the receding side of the nebula (Figure 2), is now clearly present. From Figure 48 to Figure 49, the emission from the entire main shell decreases significantly while the brightness of the filament increases substantially. Finally, considering the PV diagram for [O I] λ 6300 in Figure 50, the emission from the main shell is nearly absent while that from the filament is now very bright.

Hence, the sequence from Figure 44 to Figure 49 (and [O I] λ 6300 in Figure 50) shows that lines with similar ionization potentials, expected to be found together in the nebular plasma, present PV diagrams with similar morphologies. Since the morphology of the PV diagram is a result of the kinematics and spatial distribution of the volume of plasma that emits a given line, similar morphologies mean that the lines with similar ionization potentials are emitted together. Also, progressing from along the sequence, the changes are gradual, and continuous. Based upon the PV diagrams in Figure 44 to Figure 49, it is clear that the approaching and receding sides of the main shell are more highly ionized than the end of the main shell or the material outside the main shell on the receding side of the nebula. This structure results naturally if the sides of the main shell are closer to the central star than is the end of the main shell or if the end of the main shell has a higher density or a greater depth.

We now consider the puzzles presented by several lines, starting with the O I $\lambda\lambda$ 7771,8846 lines in Figure 50. The first is a quintuplet line that cannot be excited by fluorescence from the atom's ground state (triplet), but the O I λ 8446 triplet line is part of a decay cascade that can be excited by the H I Ly β line. The emission from the O I λ 7771 line traces only the main shell, but the O I λ 8446 line also has emission from the filament outside the main shell. The velocity splitting of the O I λ 7771 line and the morphology of its PV diagram are very similar to those for the C II, N II, O II, and Ne II lines. (Two sky lines perturb the shape of the PV diagram of O I λ 7771 and the S/N is only modest.) As for O I λ 8446, its velocity splitting may be compatible with that of the C II, N II, O II, and Ne II lines, but the details of its PV diagram are even less clear since it is fainter and the blue side of the line profile is blended with a cluster of 3 sky lines. It is conceivable that the emission from the main shell in the O I λ 8446 line is due to the plasma that emits in the C II, N II, O II, and Ne II lines, in which case the emission from the main shell would be due to recombination (the O^+ ion). It is likely that the emission in O I λ 8446 from the filament is due to fluorescence (and so the O^0 ion).

The [C I] λ 9850 line in Figure 50 may, like O I λ 8446, also represent a mixture of C ions and physical processes. The velocity splitting we measure is intermediate between those of the additional plasma component and of [O I] $\lambda\lambda$ 6300,6364 (Table 8). Emission from the main shell is clearly present. However, the brightest feature in the PV diagram is the filament on the receding side of the main shell. In this case, the emission from the main shell may be a combination of recombination (the C^+ ion) and collisional excitation (the C^0 ion), but the latter would dominate in

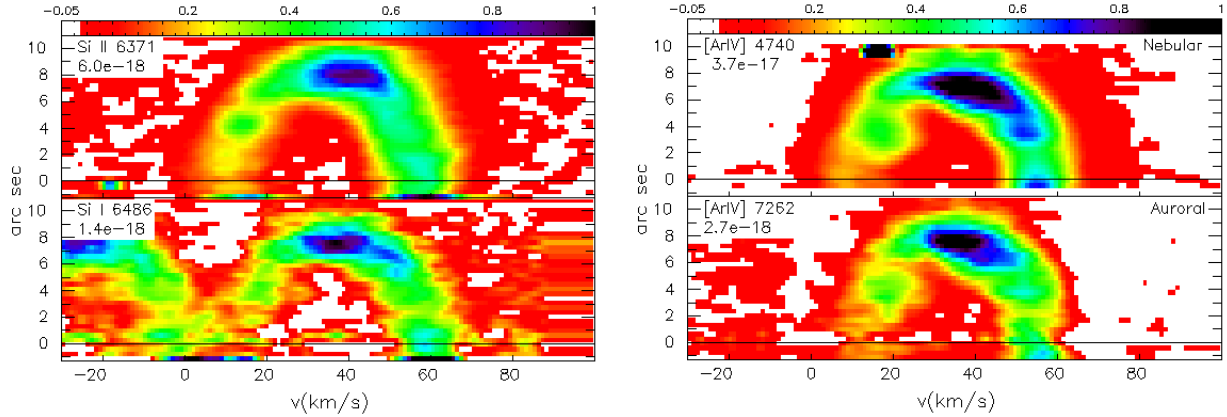


Figure 51. Left column: These panels present the PV diagrams in the lines of Si II $\lambda 6371$ and Si I $\lambda 6486$. Right column: These panels present the PV diagrams in the lines of [Ar IV] $\lambda 4740$ (nebular line) and [Ar IV] $\lambda 7262$ (auroral line). The vertical stripes of low counts (white) to the blue and red of the [Ar IV] $\lambda 7262$ line profile are due to atmospheric absorption, which affects the measurement of the velocity splitting (Table 8; Figure 5).

the filament (the C^0 ion). If so, the [C I] $\lambda 9850$ line may represent a second ionization stage of C from the additional plasma component.

The morphology of the PV diagram of the Si I $\lambda 6486$ line (Figure 51; left column) is similar to that of the C II, N II, O II, and Ne II lines (Figure 6). However, its velocity splitting is “normal” for its ionization energy (Table 8, Figure 2), though it is uncertain since the blue side of the line profile has low S/N and is blended with the adjacent lines to the blue.

In the PV diagram of the Si II $\lambda 6371$ line (Figure 51; left column), like those of the Si II $\lambda\lambda 5041, 6347$ lines, the shape of the receding side of the main shell is reminiscent of that in Figures 46 and 47, which represent more highly ionized plasma. The velocity splitting of 46.7 ± 0.6 km/s is lower than expected (~ 50 km/s) for Si^+ 's ionization energy, assuming the lines arise from recombination in the normal nebular plasma. Si II $\lambda 5041$ is from multiplet V5 while Si II $\lambda\lambda 6347, 6371$ are from multiplet V2. The lower level of V5 is the upper level of V2. The upper level of V5 can be radiatively excited from the Si^+ ground state (989.87\AA Morton 2003). Given the line splitting and the morphology of the PV diagram, there may be a fluorescence contribution in these lines in addition to recombination. A potential fluorescence source is emission in the Ne III $\lambda\lambda 989.90, 989.91$ lines from the He^{2+} zone (Van Hoof 2018, Fe V $\lambda\lambda 989.93, 989.96$ lines is a less likely possibility). The population of Si^+ ions in the He^{2+} zone will be minuscule, so the fluorescing ions will be from zones of lower ionization, though preferentially near the He^{2+} zone since the efficiency of fluorescence drops with distance due to dilution. If so, the kinematics inferred from these Si II lines in NGC 6153 may mimic the kinematics of zones of higher ionization, and not necessarily the zone where S^+ is the dominant ionization stage.

Finally, in Figure 51 (right column), the [Ar IV] $\lambda 7262$ auroral line profile has a smaller velocity splitting than its nebular counterpart (Table 8). In this case, the difference appears to be due to telluric absorption affecting both the bluest emission from the approaching side of main shell and the reddest emission from the receding side, both of which bias the velocity splitting to lower values. Unfortunately, we cannot easily check this conjecture since the other auroral lines of [Ar IV] are all contaminated by stronger lines ([Fe IV] $\lambda 7171$, C II $\lambda 7236$, [O II] $\lambda\lambda 7330, 7331$).